Microscale Airflow Simulations over Complex Alpine Terrain

THÈSE N^{O} 4071 (2008)

PRÉSENTÉE LE 5 SEPTEMBRE 2008

À LA FACULTÉ DE L'ENVIRONNEMENT NATUREL, ARCHITECTURAL ET CONSTRUIT
LABORATOIRE DE MÉCANIQUE DES FLUIDES DE L'ENVIRONNEMENT
PROGRAMME DOCTORAL EN ENVIRONNEMENT

ÉCOLE POLYTECHNIQUE FÉDÉRALE DE LAUSANNE

POUR L'OBTENTION DU GRADE DE DOCTEUR ÈS SCIENCES

PAR

Françoise FAURE

ingénieur diplômé de l'école centrale de Nantes, France
et de nationalité française

acceptée sur proposition du jury:

Prof. J.-L. Scartezzini, président du jury
Prof. M. Parlange, Dr M. Lehning, directeurs de thèse
Prof. A. Rinaldo, rapporteur
Prof. F. Stagnitti, rapporteur
Prof. V. P. Walden, rapporteur

ÉCOLE POLYTECHNIQUE
FÉDÉRALE DE LAUSANNE
Suisse
2008

Composition of the examining committee presented to the dean of the Faculty of Architecture, Civil and Environmental Engineering at the Ecole Polytechnique Fédérale de Lausanne as required for the submission of the dissertation under (ref. nb.):

Committee for oral examination:

1. Prof. Jean-Louis Scartezzini,
   Director of the doctoral program Environment, EPFL

2. Prof. Marc Parlange,
   Thesis director, EPFL/ENAC/ISTE/EFLUM

3. Dr. Michael Lehning,
   Thesis director, Swiss Federal Institute for Snow and Avalanche Research (SLF)

4. Prof. Andrea Rinaldo,
   Examiner, EPFL/ENAC/ISTE/HYDRAM

5. Prof. Von p. Walden,
   Examiner, University of Idaho - USA

6. Prof. Francesco Stagnitti,
   Examiner, Deakin University - Australia

Date: May 8, 2008

"La théorie n'est qu'un piège tendu dans l'espoir que la réalité sera assez naïve pour s'y laisser prendre."

(Jean Baudrillard)

Abstract

Accurate microscale windfields computations over complex topography is crucial to many particle transport models but remains a challenging task. The objective of this work focuses on the numerical simulations of micro-scale windfields over the steep Gaudergrat ridge, located in the Swiss Alps. These windfields are computed with the objective of driving a snowdrift model, consequently the work concentrates on meteorological situations close to snow storms. As snow transport occurs in the first meters above the surface, this implies a very fine resolution of order tens of meters.

Airflow simulations are performed using the meteorological model ARPS (Advanced Regional Prediction System), which is based on a Large Eddy Simulation (LES) formulation of the compressible Navier-Stokes equations.

The turbulent airflow features play an important role in the transport of particles. Therefore ARPS turbulence models, the Smagorinsky-Lilly and the 1.5 order Turbulent Kinetic Energy (TKE) closures, have been examined in neutral atmosphere conditions over flat terrain. ARPS mechanical turbulence schemes has hence been tested and the parameters of the Subgrid-Scales (SGS) models have been tuned.

ARPS has already been proven suitable for reproducing qualitative features of airflow and over complex alpine terrain with a careful choice of the artificial initialisation and periodic boundary conditions. When lateral periodic boundary conditions are applied for airflow computations over real complex topography, instabilities arise quickly. For a quantitative and stable description of airflow presented in this work, the initialisation and boundary conditions have consequently been improved. In this study, the simulations over the Gaudergrat ridge presented are performed a one-way nesting approach. ARPS is first driven by the outputs of the MeteoSwiss model aLMo which produce initial and time dependent lateral boundary conditions. Then the application of the nesting technique permit to bridge spatial resolutions

from 7km (aLMo grid resolution) to 25 m (horizontal resolution in the finer ARPS grid). Such a fine resolution is also required for Large-Eddy Simulations (LES) configuration and it is expected that a large part of the energy is resolved explicitly. The nesting technique has been applied to reproduce two selected days during the Gaudergrat Experiment (Gaudex) with stronger wind, to have conditions as close as possible to winter conditions and when thermal winds are weak. The field measurement campaign, Gaudergrat Experiment (Gaudex), in collaboration with the University of Leeds, was held from June to October 2003 at the Gaudergrat ridge, near Davos, Switzerland. The collected data are used to develop a better understanding of the airflow characteristics and turbulence features as well as to check the model results. The comparison with field data show satisfactory results for the mean flow quantities, whereas the lateral boundary condition forcing suppresses the small scales turbulent motion. A simple method is proposed to spin up turbulent motions in the finer resolution domain. This method is based on the introduction of turbulent perturbations from a precursor simulation onto the mean wind profile at the lateral boundaries. This new configuration facilitate the development of turbulence and resolves explicitly smaller scale motions without altering the mean flow.

The spectral analysis of the Gaudex data highlights the fact that the turbulence on the lee side of the Gaudergrat ridge is influenced by local features, whereas at the crest, the effect of the surrounding mountains is recognisable. The statistical analysis of wind speed fluctuations shows that the turbulence in complex terrain is highly intermittent, but can be interpreted as a combination of subsets of isotropic turbulence. In complex terrain, the production of turbulence is not continuous, it is hence difficult to apply the traditional scaling and averaging laws developed for homogeneous horizontal surfaces. The heterogeneous surface conditions are likely to create additional length and time scale to generalise the statistical properties.

Keywords: Windfield, complex terrain, microscale, Turbulent Kinetic Energy (TKE), turbulence.

Résumé

Le calcul numérique à micro-échelle de champs de vent en terrain complexe est crucial pour beaucoup de models de transport de particules, mais demeurre cependant une tâche difficile. L'objectif de ce travail est les simulations numériques de champ de vent à micro-échelle au dessus du Gaudergrat, montagne située près de Davos dans les Alpes suisses.

Ces champs de vents sont calculés dans l'objectif d'initialiser un model de transport de neige. Comme le transport de la neige se produit dans les premiers mètres au-dessus de la surface, ceci implique une résolution très fine de l'odre de quelques décamètres.

Les simulations sont réalisées avec le model météorologique ARPS (Advanced Regional Prediction System), basé sur la résolution des équations de Navier-Stokes pour un fluide compressible, à l'aide de simulations à grandes échelles.

Les charactéristiques de l'écoulement turbulent jouent un role important dans le transport des particules. C'est pourquoi les différents models de turbulence de ARPS, le model de Smagorinsky-Lilly et le model d'énergie turbulente cinétique d'ordre 1.5, ont été testés afin d'en ajuster les paramètres.

ARPS a déjà été utilisé pour reproduire qualitativement un écoulement d'air en terrain complexe montagneux avec une initialisation basée sur un sondage artificiel et des conditions aux limites périodiques. Cependant avec de telles conditions aux limites en terrain complexe, le calcul devient rapidement instable. Par conséquent, pour obtenir un écoulement stable, l'initialisation et les conditions aux limites ont été améliorées en utilisant la technique de "nesting" (imbrication des domaines numériques) uni-directionnel. ARPS est initialisé par les resultats de du model de MeteoSuisse aLMo qui fournissent des conditions initiales et aux limites qui dépendent du temps. Les informations sont ainsi transmises d'une résolution de 7km (résolution de aLMo) à la plus fine résolution utilisée pour ARPS: 25m Une ré-

solution aussi fine est nécessaire pour les simulations aux grandes échelles puisqu'une grande partie de l'énergie doit être résolue explicitement.

La méthode de nesting a été utilisée pour reproduire deux jours pendant la campagne de mesures Gaudergrat Experiment (Gaudex) qui a eu lieu au Gaudergrat pendant l'été 2003, en collaboration avec l'Université de Leeds. Ces deux jours sont charactérisés des vents relativement forts afin d'avoir des conditions à l'hiver et ainsi minimiser les effets des vents thermiques.

La comparaison des résultats issus des simulations avec les mesures sont satisfaisantes pour l'écoulement moyen. En revenche les conditions aux limites latérales pourvues par le " nesting" supriment les structures turbulentes de petite taille.

Une méthode simple est proposée pour faciliter le développement de la turbulence dans le domaine de plus fine résolution. Cette méthode est basée sur l'introduction de perturbations de faible amplitude, provenant d'une simulation séparée antérieure, sur le profile moyen. Ceci permet de résoudre explicitement de plus petites structures turbulentes sans altérer l'écoulement moyen.

L'analyse spectrale des mesures de la campagne Gaudex montrent que la turbulence sur la pente sous le vent est plus influencée par des structures turbulentes produites localement, alors qu'à la crête et sur la pente au vent, l'écoulement est influencé par de plus grosses structures provenant du sillage des montagnes environnantes. L'analyse statistique des fluctuations de vitesse du vent montre que la turbulence en terrain complexe est fortement intermittente mais peut être interprétée comme une superposition de sous-ensemble de turbulence isotropique. En terrain complexe, il est difficile d'appliquer les mêmes théories et dimensionnement que pour un terrain plat et homogène. Des longueurs et échelles de temps supplémentaires sont probablement nÃl'cessaire pour généraliser les lois de dimensionnement en terrain plat et homogène.

Mots clef: Champs de vent, terrain complexe, micro-échelle, énergie cinétique turbulente, turbulence.

Acknowledgements

This PhD research would not have been possible without the help and contribution from many people. I want to express my gratitude to them with these lines.

I thank Michael Lehning, my supervisor at SLF, for giving me the possibility to carry out this research work and then opening the doors of atmospheric sciences.

I thank Marc Parlange for accepting to be the director of my thesis and I appreciated that he could find some time to receive us at EPFL despite his overburdened schedule.

I thank the other members of my committee, Andrea Rinaldo, Francesco Stagnitti and Von P. Walden for accepting to be part of the examination panel and their review of the thesis. I thank Jean-Louis Scartezzini for serving as the chair of my oral examination.

Airflow simulations were made using the ARPS model developed at the Center for Analysis and Prediction of Storms at the University of Oklahoma.I appreciated the online support and clarity and consistancy of their code.

I thank Elie Bouzeid for his help and valuable suggestions concerning the turbulence modelling.

Christophe Hug provided a valuable assistance with the installation of linux at the begining of my PhD and all kind of computing issues.

Windfields studies at SLF are a long story: Rolland Meister and Paul Foehn started the wind fields investigations at the Gaudergrat, then Peter Gauer took over with the installation of permanent weather stations at the Gaudergrat and started the numerical experiments with CFX fluid dynamic code. Norbert Raderschall did the first windfields simulations with ARPS Submeso version. They are here all acknowledged.

The Gaudex field campaign has been planned by Stephen Mobbs. Quality control of the "Leeds part" of the Gaudex data set was proceeded by Huw Lewis.

Thanks also to all participants of the Gaudex from University of Leeds, SLF or University of Innsbruck.

I thank Michele Guala for his interest to the project and valuable ideas and suggestions.

Fotini Katopodes Chow, Oliver Fuehrer and Andreas Weigel answered my questions during my first steps with ARPS. Thanks to Mathias Rotach for his "Boundary Layer Meteorology" course.

Topography files, landcover data and orthophotos have been prepared by Andreas Stoffel and Micheal Schirmer.

MeteoSwiss aLMo data as well as documentation concerning the aLMo model have been provided by Francis Schubiger and Emanuele Zala.

Concerning the use of windfields for snow drift simulations, I appreciated the discussions with Henning Loewe, and the feedback from Rebecca Mott.

I thank my colleagues, Charles Fierz, Nora Helbig, Constantino Manes and Jean-Daniel Rüedi for their valuable comments.

The interesting discussion with Joachim Peinke and David Kleinhans leaded to the statistical analysis of the turbulence in 2.

I thank Iljia and Martin for their friendship and accommodation during my classes at EPFL.

I thank Marie-Jo Pellaud, Sylvette Renfer and Barbara Tinguely for their assistance with infrastructure and administrative work at EPFL.

Part of the computations were run at the Swiss Supercomputing Centre (CSCS), on the Cray XT3 platform. Optimisation and scaling of ARPS on the Cray XT3 was made by Mark Cheeseman. (Computational support was provided in part by the CSCS).

I am grateful to Jan-Moritz for his constant encouragements and his patience during these years.

Finally, many thanks to my family for their unconditional support and encouragements.

The Swiss National Science Foundation, project 107654, provided the funding for this project.

Notations

List of symbols

$\overline{()}$	Mean component (Reynolds decomposition)
$\widetilde{()}$	Filtered motion or resolved motion (LES)
$()'$	Fluctuation from the mean
C_k	Smagorinsky coefficient
C_ε	Diffusion coefficient in the TKE prognostic equation
dt	Time step (s)
dt_{big}	Large time step in ARPS (s)
dt_{sml}	Small time step in ARPS (s)
$d\tau$	Small time step (s)
dx	Grid spacing or horinzontal resolution in the x-direction (m)
e	Turbulent kinetic energy per unit mass of the subgrid scales ($m^2.s^{-2}$)
f	Frequency ($s^{-1} or Hz$)
f_c	Coriolis parameter (s^{-1})
g	Acceleration of the gravity ($m.s^2$)
K_m	Mixing coefficient for momentum (or eddy viscosity) ($m^2.s$ in the ARPS 1.5 order TKE closure)
K_h	Mixing coefficient for heat (or eddy diffusivity) ($m^2.s$ in the ARPS 1.5 order TKE closure)
K_{mh}, K_{mh}	Mixing coefficient for momentum for the horizontal direction, vertical direction ($m^2.s$ in the ARPS 1.5 order TKE closure)
$(K_m)_{ij}$	Mixing coefficient (or eddy viscosity) for momentum at grid point (i,j) ($m^2.s$ in the ARPS 1.5 order TKE closure)
k	Wave number (m^{-1})
Lx, Ly	Horizontal length of the domain in the x, y directions (m)

Lz	Vertical length of the domain (m)
ℓ	Mixing length (Prandtl) (m)
ℓ_s	Mixing length for stable conditions (m)
N	Brunt-Väisälä frequency (s^{-1})
Nx	Number of grid points in the x-direction
Ny	Number of grid points in the y-direction
Nz	Number of grid points in the z-direction
nx	Number of grid points in the x-direction
ny	Number of grid points in the y-direction
nz	Number of grid points in the z-direction
Pr_t	Turbulent Prandtl number
p	Pressure ($kg.m^{-1}.s^{-2}$ or Pa)
R	Correlation function
R_α	Correlation function for variable α
S_{ij}	Velocity strain tensor (s^{-1})
U	Total velocity magnitude ($m.s^{-1}$)
$\mathbf{U}$ or $\vec{U}$	Total velocity vector
u	Eastward or x-direction wind velocity component ($m.s^{-1}$)
$\mathbf{u}$ or $\vec{u}$	u-velocity vector ($u(x, y, z, t)$)
u_*	Friction velocity ($m.s^{-1}$)
v	Northward or y-direction wind velocity component ($m.s^{-1}$)
$\mathbf{v}$ or $\vec{v}$	v-velocity vector ($v(x, y, z, t)$)
w	Vertical or z-direction wind velocity component ($m.s^{-1}$)
$\mathbf{w}$ or $\vec{w}$	w-velocity vector ($w(x, y, z, t)$)
$\vec{x}$	Position vector ($\vec{x} = (x, y, z)$)
z_o	Dynamic roughness length (m)
z_i	Boundary Layer Depth (m)

Δ	Grid size (m)
Δ_f	Filter size for Large-Eddy simulation (m)
Δh	Grid size in the horizontal direction (m)
Δt	Time step (s)
Δv	Grid size in the vertical direction (m)
$\Delta x, \Delta y, \Delta z$	Grid size in the x, y, z-directions (m)
$\Delta_x, \Delta_y, \Delta_z$	Filter size in the x, y, z-directions (m)

Δz_{av}	Average grid size in the z-direction (m)
Δz_{min}	Minimum grid size in the z-direction (m)
δ_{3i}	Kronecker delta tensor or identity tensor
ϵ	Dissipation rate of the turbulent kinetic energy
ε	Dissipation rate of turbulent energy ($m^2.s^{-3}$)
κ	Von Kármán constant
λ	Wavelength (m)
ν	Kinematic viscosity ($m^2.s^{-1}$)
μ	Dynamic viscosity ($kg.m^{-1}.s^{-1}$)
(ξ, η, ζ)	Curvilinear coordinates, terrain following coordinates
ρ	Density ($kg.m^{-3}$)
Θ	Taylor scale (m)
θ	Potential temperature (K)
θ_v	Virtual potential temperature (K)
τ_{ij}	Reynolds stress tensor ($m.s^{-1}$, in dynamic units)

List of acronyms

ABL	Atmospheric Boundary Layer
aLMo	Alpine Model
ARPS	Advanced Regional Prediction System
AWS	Automatic Weather Station
BADC	British Atmospheric Data Centre
CAPS	Center for Analysis and Prediction of Storms
CBL	Convective Boundary Layer
CPU	Central Processor Unit
CSCS	Swiss Super Computing Center
DNS	Direct Numerical Simulations
DWD	Deutscher Wetterdienst
ECMWF	European Center for Medium-range Weather Forcast
Gaudex	Gaudergrat Experiment
LES	Large-Eddy Simulations
LM	Lokal-Modell
MAP	Mesoscale Alpine Programme
MO	Monin-Obukhov
MOST	Monin-Obukhov Similarity Theory
NWP	Numerical Wather Prediction
PBL	Planetary Bounbary Layer
PDF	Probability Density Function
RANS	Reynolds-Averaged Navier-Stokes
SFS	Subfilter Scale
SGS	Subgrid Scale
TKE	Turbulent Kinetic Energy

Contents

Chapter 1

Introduction

Wind is one of the most influencing factors for avalanche danger. Indeed large amounts of snow can be transported by the wind and redistrubuted unevenly creating an extra load on mountains slopes. Accurate three-dimensional and time-dependent windfields are required to model snow erosion and deposition zones, for avalanche danger estimation or for hydrological purposes Raderschall et al. (2008, submitted). The transport of snow occurs in the first tens of meters of the boundary layer, consequently to capture this phenomenon, a resolution of the order of a few meters is necessary. The turbulent structures in the surface layer region play an important role in the particle transport. The performance of numerical simulations remains however limited, and parameterisation are required. Large-Eddy Simulations (LES) over steep terrain have been recently made possible by the development of computing power. Experimental observations are also required for a better understanding of the flow characteristics as well as to check the numerical experiments.

In this dissertation, LES are applied in order to compute the airflow over a steep Alpine ridge using ARPS (Advanced Regional Prediction System) meteorological model Xue et al. (1995, 2000, 2001). This chapter reviews current practice in modeling the Atmopheric Boundary Layer (ABL) and highlight issues in modelling windfields above complex terrain. Finally the motivation for this work and an overview of the content of this work is presented.

1.1 Airflow over complex mountainous terrain

Accurate prediction of windfields over mountainous terrain is of crucial importance for weather prediction as mountain ranges can significantly influence weather and climate up to hundreds of kilometers away. The Atmospheric Boundary Layer depth is about 1 to 3 km (Stull, 1988), though it depends on the underlying terrain and weather conditions. Whereas the momentum, heat and water vapor exchanges influence the whole ABL, the region of focus is the first tens of meters above the surface, i.e. the surface layer, where drifting snow occurs. In mountainous terrain, vertical accelerations can be important, i.e. the motions are no longer hydrostatic, so the range of interest is the meso-γ scale, and the Coriolis effects are small (Pielke, 1984). The scales of motions in the ABL are also dependent on the stratification. In a stable boundary layer, the turbulent structures become finer and vertical motions are inhibited. This is the hardest case to simulate. In a convective boundary layer, the heating of the surface drives large, resolvable motions which mix the boundary layer. However the stratification on which this work is based is the neutral boundary layer, where the potential temperature decreases with the height, following the adiabatic lapse rate. Indeed during a snow storm, the strong winds lead to a well mixed ABL.

Flows over hills can generate flow separation in the leeward side, lee waves and rotors depending on the hill's height and steepness. Whereas for an isolated hill the turbulence in the wake region decreases further downwind, in the case of a real mountain massif, the wake flows interfere and lead to a complicated turbulent flow. In mountainous terrain the flow must be modelled as fully three-dimensional.

An internal boundary layer forms within the existing boundary layer when the flow passes from one roughness scale to another. Moreover in mountainous terrain, each slope has a different heating capacity due to the variety of surface covers, slopes angles and orientations, which creates a inhomogeneous temperature field. This more complex distribution creates local circulations and thermal turbulence that interact with the synoptic circulation making the prediction of the ABL evolution even more complicated. A detailed description of the circulation in mountainous regions is presented in Whiteman (2000) and (Stull, 1988, chapter 14).

The first mathematical descriptions could be tested in the field with the support of observational campaigns. It started with the study of the moderately sloped hill Brent Knoll (Mason and Sykes, 1979). Many similar campaigns followed with various shaped hills to study different aspects of the flow. Observations were made

of the flow over the three-dimensional low to moderate sloped hills: Black Mountain (Bradley, 1980), Blashaval (Mason, 1985), Askervein (Taylor and Teunissen, 1987) and Kettles Hill (Wood, 1988). All these field campaigns agreed with the predicted theory even in case when the theory is not strictly applicable, at least for sites upstream and at the crest. However traditional scaling laws and averaging procedures developped for horizontally homogeneous ABLs are not applicable to these datasets. Complex terrain are likely to require additional time and length scales to generalise the statistics.

When the slopes are steeper, the flow becomes more non-linear and the analytical analysis has to be replaced by numerical modeling. Further understanding of the turbulence structure came with the numerical modeling conducted in the eighties. Nevertheless observational and analytical analyses were still carried on, with for example wind tunnel experiments (Ross et al., 2004) and asymptotic developpement for the analytical analysis (Sykes, 1980). The turbulent flow and inviscid flow were traditionally quite separate ways of describing an airflow. However Zhou et al. (1995) discussed the interaction between the lee waves response in the free atmosphere and the flow response in the underlying boundary layer.

Energy balance, i.e. temperature, moisture and radiation budgets, is a crucial aspect in turbulent flow. Raupach and Finnigan (1997) present a detailed review of temperature and moisture budget in complex terrain. Huntingford et al. (1998) have used a fully non-linear model to investigate the response of the moisture fluxes in the presence of steep hills.

The complete description of turbulence, not only over mountainous terrain, still remains one of the unsolved problems in physics and a challenging task for both measurements and modeling techniques.

1.2 Large-eddy simulations of the airflow over complex terrain

ABL flows are highly turbulent with Reynolds numbers of order 10^8. Consequently the three-dimensional compressible Navier-Stokes equations cannot be solved analytically and numerical modeling is necessary. However it is today still not possible to solve explicitly the large range of motion scales. In addition the Earth's surface is rough and directly adjacent to it exists a viscous sublayer which is only a few millimeters thick and where the shear stress is caused predominantly by viscosity. Consequently the turbulence parameterisation has a particular importance,

especially near the surface. Numerical simulations of the ABL flows are also highly sensitive to the bottom approximate boundary conditions.

Large eddy simulations (LES) of atmospheric flows relies on the usual set of equations for balance of momentum, mass and energy. With this method, only the scales up to the filter size Δ are solved and all scales that are smaller than the filter size are Subgrid-Scales (SGS) which are parameterized. The equations to be solved for the large-eddies, or resolved motions, are obtained by filtering in space the compressible Navier-Stokes equations up the filter size. This set of equations has been completed by initial and boundary conditions and a sub-grid scale (SGS) model. The sub-grid scale model formulation depends on the problem. The motions that are not resolved by the LES are assumed to be universal. Thus a SGS model should be sufficient to resolved them.

The atmopheric boundary layer (ABL) contains a large range of scales. The LES technique was first applied to the ABL by Deardorff (Deardorff, 1972). From his experiments, he deduced the scaling parameters for a convective boundary layer. LES are nowadays known as a powerful method to solve atmospheric turbulent flows. Several models are presented in the literature with different type of closures. In the first order models, the turbulent fluxes are proportional to the strain tensor and the exchange coefficient K. The simplest models do not take into account the transport equations for turbulent quantities, but express K as a function of the mean strain tensor and the mixing length. Higher order models include a transport equation for turbulent kinetic energy (TKE) and make use of one or more length scales to calculate turbulent quantities, like Reynolds stresses or TKE (Yamada and Mellor, 1975). The most commonly used turbulence models in LES of ABL flows are the first order Smagorinsky model and the 1.5 order Turbulent Kinetic Energy (TKE) model. For the classical Smagorinsky model (Smagorinsky, 1963), a non-linear eddy-viscosity is derived from the hypothetized balance between shear production and dissipation. These eddy-viscosity models are known to be highly dissipative, do not allow the backscatter of energy from small scales to large scales. However they are widespread due to their simplicity and have already successfully been used for airflow simulations over complex mountainous terrain (Chow et al., 2006; Weigel et al., 2006). A model that does not include transport equations is essentially local in nature and hence it can only reproduce the balance between local TKE production and dissipation rates. In case of complex terrain, a more

sophisticated closure taking into account the TKE transport and diffusion should be applied (Zeman and Jensen, 1987). A simple model where the eddy coefficient does not take into account horizontal variations is not appropriate to compute flow over complex terrain. However introducing a transport equation allows to account for such inhomogeneities. In the subgrid model used by Deardorff (Deardorff, 1980), a prognostic equation for the subgrid turbulent kinetic energy transport is solved and the SGS fluxes are related to the resolved scale motions.

In LES, the spatial resolution is an integral part of the SGS model through the filter size. Hence it is essential to provide a resolution that can resolve the most energetic scales. Many numerical weather models use a grid spacing that fall within the spectral gap to resolve explicitly the large scales of the production range. Moeng (1984) suggests that the filter size should be in the inertial sub-range. Indeed previous LES studies show that most of the statistics are insensitive to the grid resolution, provided the grid size lies in the inertial subrange over the bulk ABL. The size of the smallest resolved eddies in a large-eddy numerical simulation depends on the numerical scheme used to discretise the equations (Senocak et al., 2007). In the case of finite differences methods, the filter size is also implicit.

If the energy containing scales are resolved, the interior of the flow, i.e. away from boundaries, and for a mixed layer is relatively insensitive to the Subgrid Scale (SGS) model (Khanna and Brasseur, 1998). In regions of strong shear, SGS parameterizations become however increasingly important (Sullivan et al., 1994, 1996). Hence, any imperfection in the SGS parameterizations could account for an underestimation of the momentum flux.

Near the bottom boundary, however, the energy containing turbulent motions become more anisotropic and smaller than in the middle ABL, hence the filter scale (associated to the grid spacing) is larger than the turbulent motions at the wall and a larger amount of scales are parameterized. In this region the flow is as a consequence underresolved or implies high computational costs. It is argued that the errors from the near surface affect the entire boundary layer (Juneja and Brasseur, 1999). To overcome the coarse resolution in the surface layer, an additional stress may be needed to represent the small scale motions. A near-wall stress model, which distributes stress generated at the rough wall over the near-wall region, can be used in addition to the SGS model. This idea has been first applied to represent the increased drag of the vegetation canopies on the flow, which gives them the

name of canopy models (Patton et al., 2001; Shaw and Schumann, 1992). Brown et al. (2001) extended the idea to flow over a rough surface. Their near-wall model uses the classical Smagorinsky model with addition of turbulent stresses to the SGS stresses in order to improve the wind profile within the surface layer. Another method to improve the numerical results near the surface is the use of LES away from the surface combined with Reynolds-Averaged Navier-Stokes (RANS) models near the surface. For example in the eddy-viscosty proposed by Sullivan et al. (1994), a so-called isotropy factor that accounts for anisotropic effects and determines the transition from LES to RANS. Mason and Callen (Mason and Callen, 1986) proposed a length scale base on the LES filter size and the distance to the surface for the classical Smagorinsky SGS model. This last model can also be improved by the addition of a stochastic energy backscatter model (Mason and Thomson, 1992): random stresses are produced to improve the matching between different length scales, hence improve the prediction of the logarithmic profile in the surface layer. In addition, the roughness of the bottom boundary condition is not applied directly but needs to be parameterized to avoid too large stresses when the vertical resolution becomes coarse. The bottom boundary is represented using similarity laws and aerodynamic drag coefficients calculated from the roughness height. In atmospheric boundary layer flows, a method to apply the no-slip condition consists of fixing a logarithmic profile in the surface layer and imposing the surface fluxes as boundary conditions, (Moeng, 1984). However over complex mountainous terrain, where flow separation often occurs, the similarity profiles are not always appropriate. Wood (2000) recommends that the lowest internal grid point should be close enough to the surface for the surface no-slip boundary condition to be imposed by the law of the wall. The vertical stretching of the vertical levels permit a finer resolution near the ground surface. The vertical grid spacing is hence much smaller than the horizontal one, leading to well resolved eddies in the vertical but not in the horizontal.

Another improvement can be achieved by the use of a Reconstruction Subfilter Scale (RSFS) closure model combined with eddy-viscosity models, as the mixed-model of Bardina et al. (1983), to reduce numerical errors in finite-volume or finite-difference formulations of LES models. Chow (2004) implemented a Subfilter Scale (SFS) reconstruction model based on the Taylor series expansions in order to create a robust SFS model for flow computations over a rough wall. This model gives encouraging results. Porté-Agel et al. (2000) explained the inconsistency of the

assumption of scale invariance of the dynamic Smagorinsky model when the filter length is outside the inertial subrange and developped a scale-dependent SGS model for the neutral ABL. Based on a second test filtering, the model determines how the coefficients varies with scale, near the surface the length scale becomes comparable to the local integral scale, i.e. of the order of the distance to the wall. Promising results have been computed with dynamic SGS model (Bou-Zeid et al., 2005; Germano et al., 1991; Porté-Agel et al., 2000), where the SGS parameters of the original Smagorinsky are computed from the resolved flow, are much more accurate but still difficult to apply to real topographies such as steep mountains, due to spectral methods and sharp Fourier cut-offs in filters. In addition, Fourier spectral methods require periodic lateral boundary conditions, which are more complicated to apply to airflow computations over terrain that is inhomogenous in x- and y-directions, although improvment have been made recently.

Beside the problem of the near surface underresolved flow, ABL airflow models tend to suppress turbulence to gain stability. A method to keep the turbulence of the flow was proposed by Spalart (1988) in the context of engineering flow computations and applied by Mayor et al. (2002) in order to compute the development of an internal boundary layer associated with a cold air outbreak. The method is based on the recycling of turbulence from a vertical plane located downstream of the flow. The simulated turbulent perturbations are reintroduced at the inflow boundary on the mean profile. The mean profile, obtained from a precursor run, is maintained constant over the whole simulation. This method works well, provided that the wind direction remains constant. This is more difficult to apply when computing one full day over an Alpine ridge.

Grid nesting is now a common method used in Numerical Weather Prediction (NWP) simulations for initial and boundary conditions. Boundary conditions are time dependent and obtained from the results of coarser surrounding grid. It permits to increase the resolution while keeping a large computational domain. Consequently more scales are resolved by using the LES technique (Sullivan et al., 1996). This method is of particular interest for mountainous terrain where a fine resolution is necessary to resolve the topography correctly while keeping the influence of the synoptic weather conditions. This grid nesting approach is more appropriate for computations of a realistic atmospheric boundary layer over complex terrain. Clark and Hall (1991) introduced the nomenclature: one-way nesting when the fine grid

is driven solely by coarse mesh, as opposed to two-way nesting when the fine mesh is incorporated in the coarse mesh. The second method is preferred to the first one as it allows the transmission of small scale turbulence information toward larger scales, however the compuational cost is higher. Chow et al. (2006) and Weigel et al. (2006) used the one-way netsting technique to perform LES of the ABL in an Alpine steep valley with the meteorological model ARPS. The outer mesoscale domain was initialised using the ECWMF outputs, before running four other ARPS numerical domains with decreasing horizontal resolution. Two-way nesting was applied to LES by Sullivan et al. (1996). The nesting was applied to the vertical direction and both domains had the same horizontal size to keep lateral periodic boundary conditions. Moeng et al. (2007) looked at the horizontal nesting configured, as they called it, "LES-within-LES". The outer domain used periodic boundary conditions whereas the nested domain used boundary conditions based on the outer simulated flow. The classical Smagorinsky closure is modified in order to avoid a bias in the near surface wind: it is completed with a new part introducing an additional near wall eddy diffusivity that is grid independent. The issue of the law of the wall deficiency in the surface layer remains. The method works well in the case of two LES domains, however it may be more complicated to apply with traditional PBL parameterisations.

In the case of NWP, the authors suggest to gradually scale down from mesoscale to turbulence domain using multiple nests. Moreover the construction of nested boundaries from the mesoscale model are laminar by construction, which does not allow the development of the turbulent flow. This problem has been also investigated in this thesis.

1.3 Goals and outline of the thesis

The computations of accurate mean and turbulent parts of the airflow very high resolution and over complex mountainous terrain still remains a challenging task. The goal of the thesis is to improve the understanding of airflow over the steep Gaudergrat ridge and to provide very high resolution accurate and stable windfields (mean flow and turbulence), for snowdrift computations. For this purpose, the meteorological model ARPS is used in combination with the data from a measurement campaign, Gaudex 2003, which was held during the summer 2003 at the Gaudergrat ridge, located in the Swiss Alps. The extended dataset is used to check the numer-

ical predictions as well as to investigate the airflow characteristics over the steep Gaudergrat ridge.

In chapter 2, the turbulence characteristics at the Gaudergrat ridge are investigated using spectral and statistic analysis of the windspeed measurements from the Gaudex. The results show tat the windward side of the ridge is influenced by surrounding mountain wakes, whereas the leeward side is influenced by smaller structures produced locally. The turbulence at the Gaudergrat ridge can be decomposed as a subset of isotropic turbulence.

In chapter 3, the meteorological model ARPS is tested in a neutral atmospheric boundary layer, over a flat rough terrain in order to check the turbulence models available in ARPS: the Smagorinsky-Lilly model and the 1.5 order Turbulent Kinetic Energy (TKE) model. The lateral boundary conditions are periodic to allow the flow to be fully developed and for comparisons with results of similar computations found in the literature. This study highlight the limits of the model in representing the small turbulence scales near the surface. In addition this study permits to tune the turbulence model parameters in the ARPS code for the computations over the steep Gaudergrat ridge.

The airflow simulations over real topography are presented in chapter 4. As shown by previous studies the initial and boundary condition description need to be improved to ensure stability of the flow without filtering to much turbulent motions. To achieve stable computations over a complete day, the grid nesting technique is applied to provide time dependent boundary conditions and for the first time ARPS is initialised with the MeteoSwiss Alpine Model aLMo. This model has the advantage to be already set for Alpine regions and has a horizontal resolution of 7km. These numerical experiments permit to determine :

- how well the Large Eddy Simulations as configured in ARPS perform in complex terrain

- how the nesting technique affects the mean flow and turbulent motions, in the case of a very fine resolution such as 25m.

While the application of nested boundaries provides satisfying results for mean flow features, it suppresses a large part of the small scales motions. A simple method has been implemented to facilitate the development of small scales turbulent motions.

Chapter 5 summarises the work achieved in the thesis and proposes recommendations for the next LES of the very fine scale windfields over the Gaudergrat ridge using ARPS. Windfields have been computed in order to drive the snowdrift module of the Alpine3D code. A test has been run for a 2-day snow storm that took place in October 2003. This test pointed out further improvements.

Chapter 2

Characteristics of the turbulence at the Gaudergrat

2.1 Introduction

Atmospheric air flows are highly turbulent, with Reynolds number of order 10^8. Thus analytical solution or direct numerical simulations (DNS) are not capable to resolve such a flow and a statistical or spectral analysis can provide a better description. The spectral analysis can quantify the distribution of energy among the different scales of the turbulence. In the literature, little is reported about turbulence study over complex mountainous terrain. The aim of this study is to investigate the influence of the steep Gaudergrat ridge on the turbulence using the Gaudergrat Experiment 2003 (Gaudex 2003) data set and compare with the Kolmogorov statistical theory or experimental results obtained over flat terrain (e.g. Kansas experiment, Kaimal et al. (1972)).

Atmospheric boundary layer turbulence has also the property to be highly intermittent. Intermittency can be generally defined as the capacity of a nonlinear system to alternate between apparently periodic and chaotic states, in the case of a flow, when a laminar flow is interrupted by turbulence. It can also be defined as the occurrence of a gust, even during a storm. In this chapter this second definition is considered. Results from Böttcher et al. (2003, 2006) show that intermittent distributions can be explained by a superposition of different subsets of isotropic homogeneous stationary turbulence. The turbulence observed in the nature is a

superposition of different motion scales that individually respect the spectral characteristics of the isotropic homogeneous stationary turbulence, in particular the Kolmogorov energy cascade law in the inertial subrange. The spectra for all superposed scales do not however respect this theoretical law. The turbulence observed over real topography is similar to the one observed in the laboratory (i.e. isotropic and homogeneous), provided the mean velocity component (Reynolds decomposition) stays at the same order of magnitude and the averaging period is about 10 minutes. Also Böttcher et al. (2006) show that the probability distribution functions (noted PDFs hereafter) of atmospheric turbulence change their shape only for the smallest scales of motion and then stay constantly intermittent for a broad range of scales. In their study, the atmospheric datasets were recorded over flat land, offshore and over a more complex terrain with gentle mountains. In this study, the statistics of wind gusts are investigated for a more complex topography : over a steep Alpine ridge, the Gaudergrat. The aim is to check if the assumption of Böttcher et al. (2003) is also valid at the Gaudergrat.

In this chapter, after presenting the Gaudergrat experiment (Gaudex 2003), the theoretical background is described. Then the influence of the averaging period on the rotatation of the data in the mean streamline coordinate and on the Reynolds decomposition is investigated. A statistical analysis of the wind is presented to check if the hypothesis of Böttcher et al. applies to the Gaudergrat. The rotated data are finally used for a spectral analysis of windspeed at the Gaudergrat.

2.2 Presentation of the Gaudergrat Experiment 2003

The Gaudergrat Experiment (Gaudex) is an airflow experiment over an Alpine ridge, the Gaudergrat. The measurement campaign took place from June to October 2003, as a joint project between the Leeds University, the Swiss Federal Institute for Snow and Avalanche Research (SLF), and additional support from the University of Innsbruck. The goal of this measurement campaign was to study the flow characteristics over a steep ridge and provide an extended dataset for model comparisons. More than thirty measurement stations were installed around the ridge of interest, located near Davos in Switzerland (latitude 46.46 N and longitude 9.80 E). Figure 2.1 shows a map of the Gaudergrat region : the ridge is in the middle of an Alpine massif and the airflow is influenced by the surrounding higher mountains, located a few kilometer further and the Gaudergrat ridge is quite isolated over a plateau. It can

be notice that there is a broad valley at the north end of this plateau, which makes the ridge strongly exposed to the north, north-west winds.

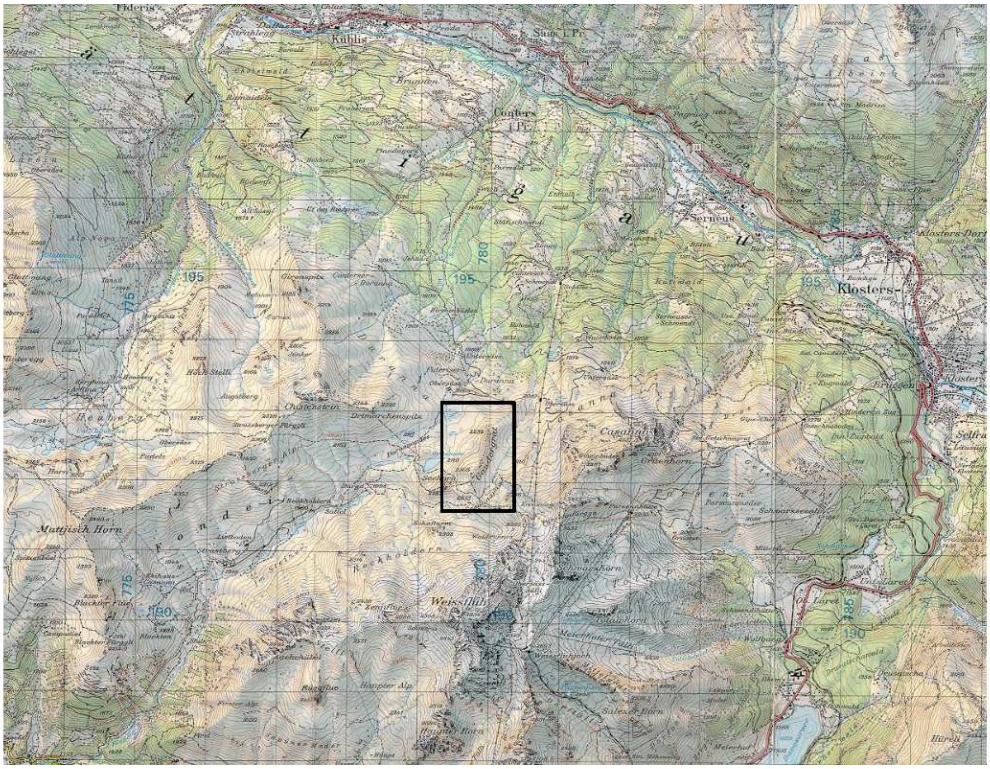

Figure 2.1: Map showing the Gaudergrat ridge (small frame), surrounded by the valley of Davos on the east side, and the Prättigau valley on the north side. Map scale : 1 : 50000

Figure B.1 presents a view from the south of the ridge : the hill is fairly uniformly rough with a covering of grass and small shrubs. The ridge is located at about 2200 meters above sea level and is about 250m higher than the sourrounding topography. Its cross section is roughly symmetric with very steep slopes : up to 55 degrees, which produces flow separation with eddies in the lee-slope.

Twenty-eight Automatic Weather Stations (hereafter called AWS) were installed around the ridge with a higher density of sites on the lee-slopes as the flow separation is expected to be found on this side. AWS 1 to 21 were provided by the University of Leeds, each measuring the atmospheric pressure, the horizontal wind speed and direction with a 1 second resolution and temperature and humidity with a 4 seconds resolution. Site 28 was provided by the Institute for Meteorology and

Geophysic Innsbruck (IMGI) and measured the same parameters as the Leeds AWS with a 1 minute resolution. At he same location, radiosondes (identified as 34 on the map) were launched once a day. Sites 22 to 27 were SLF stations measuring wind, temperature, humidity and radiation measurements at 2, 3 and 5 meters above the ground. Site 23, 24 and 25 were equipped with UVW anemometers and measured the three wind components with a 1 second resolution (1Hz). Sites 22, 26 and 27 measured horizontal wind speed and direction, air temperature and humidity at a 10 seconds and/or 30 minutes resolution. Moreover sites 26 and 23 acquired incoming and reflected short wave radiation, and snow height with a 30 minutes resolution. Two SODARS were installed on both sides of the ridge at sites 29 and 30. Sites 31 to 33 are sonics mounted at 7.5 and 15 meters above the ground and recorded the three wind speed components as well as the virtual temperature with a resolution of 0.2 seconds (5 Hz). An overview of the sites locations around the ridge can be seen in Figure 2.3. A more detailed description of the Gaudex is presented in (Lewis, 2006, chap. 3 and annexes). All the data have been quality controlled and organised following the British Atmospheric Data Centre (BADC) guidelines.

Figure 2.2: The Gaudergrat ridge, view from south during the Gaudex

The 3-axis ultrasonic anemometers used during Gaudex were are able to measure wind in the range of 0° to 360°, according to the manufacturer. The accuracy of velocity measurements is 0.02m/s. The turbulence towers were measuring data from 13th of July to 25th of August, with a frequency of 5Hz, at 15 and 7.5m above

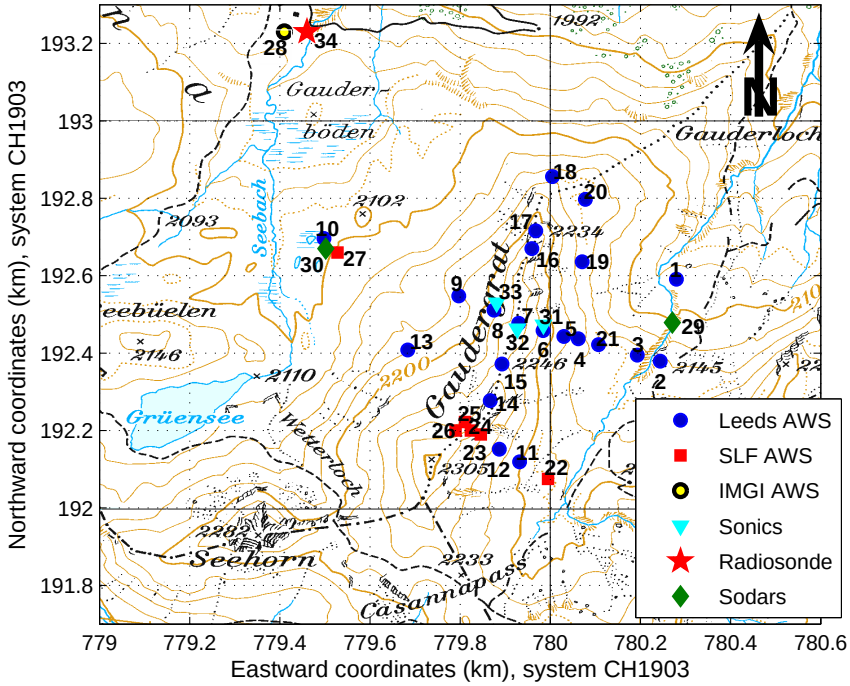

Figure 2.3: Gaudex sites map

the ground. The ultrasonic system was fixed on a metal boom at 1 meter from the mast, in order to avoid the flow distortion from the mast. An automatic weather station (AWS) was located near each turbulence tower as shown in figures 2.4(b) and 2.3.

Little is known about the optimal installation for ultrasonics measurements over slopping terrain. In the post-processing of turbulence measurements, the data will be rotated in the mean streamline coordinates to remove the influence of instrument's alignment. However the mount of the sensor remains important to avoid flow distorsions. Consequently the ultrasonics measurement volume should be oriented in the direction of the prevailing winds and as far as possible from other mast and instruments (Wilczak et al., 2001). During the Gaudex, the sonics have been mounted according to previous Gaudergrat wind studies (Gauer, 2001), that indicate prevailing wind from the directions west to north. As explained in (Lewis, 2006, chapter 3.4.4), on the west slope (site 33), the boom was rotated 45° toward

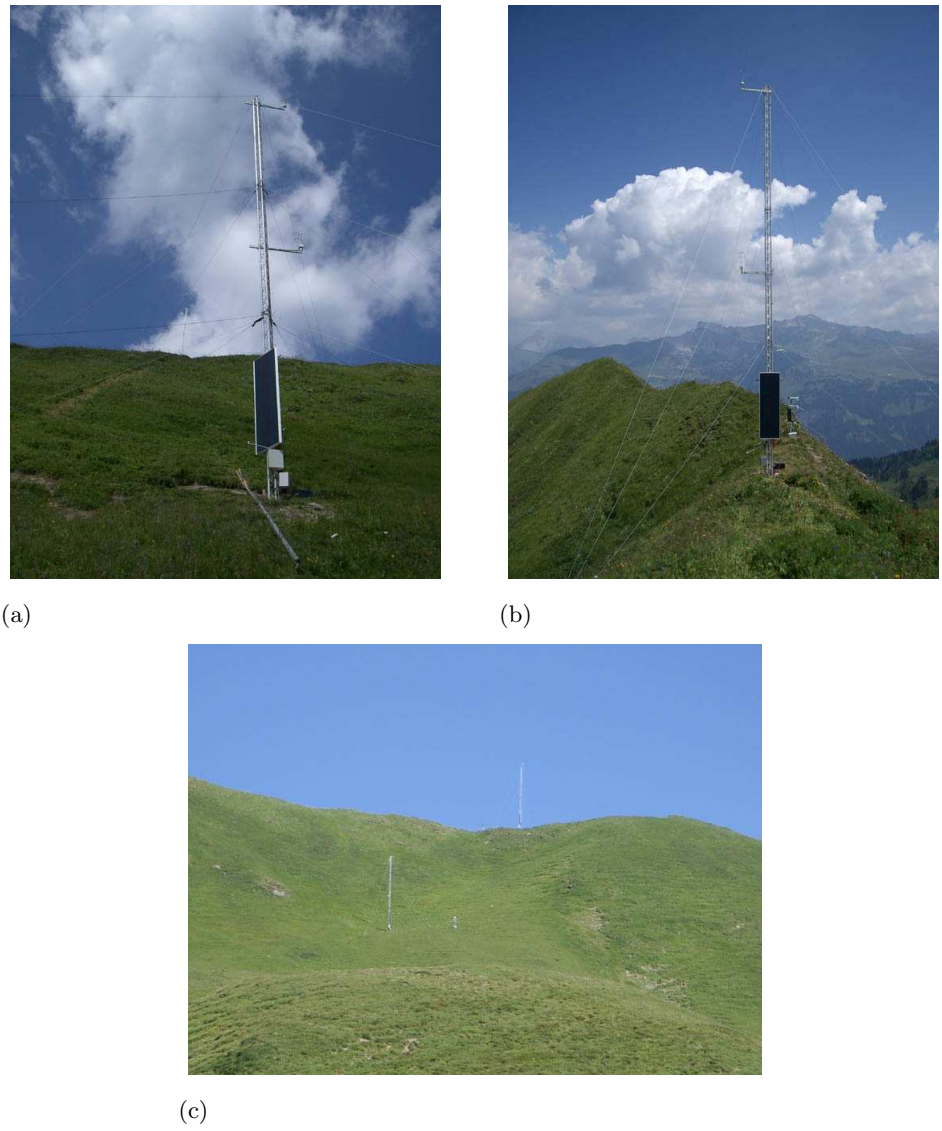

(a) (b)

(c)

Figure 2.4: Turbulence towers during the Gaudex, (a) east slope (site 31), (b) Ridge (site 32), (c) west slope (sites 33 and 32)

the ground so that the sonics were aligned with the underlying ground. A scheme representing the sonic's orientation is given in Figure 2.5. At the ridge (site 32), no tilting was applied in order to measure upslope wind from both the west and the east slope. According to previous wind studies at the Gaudergrat, the east slope is most

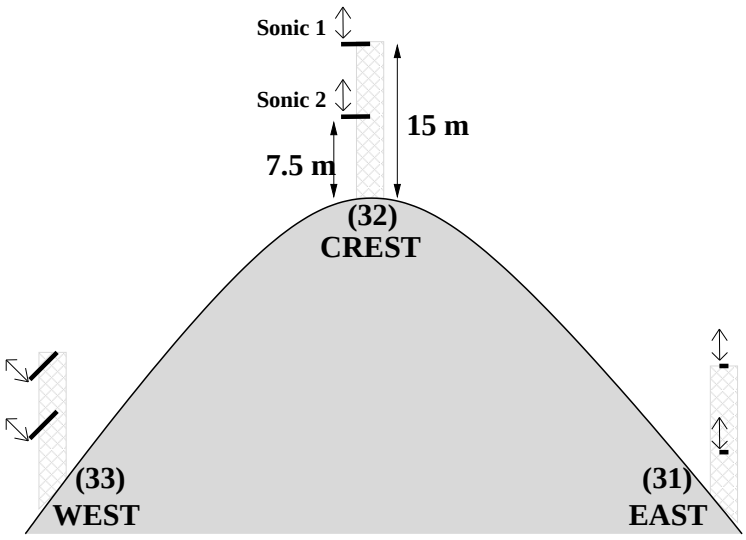

Figure 2.5: Schematic view of the sonics orientation during the Gaudex (courtesy of Huw Lewis)

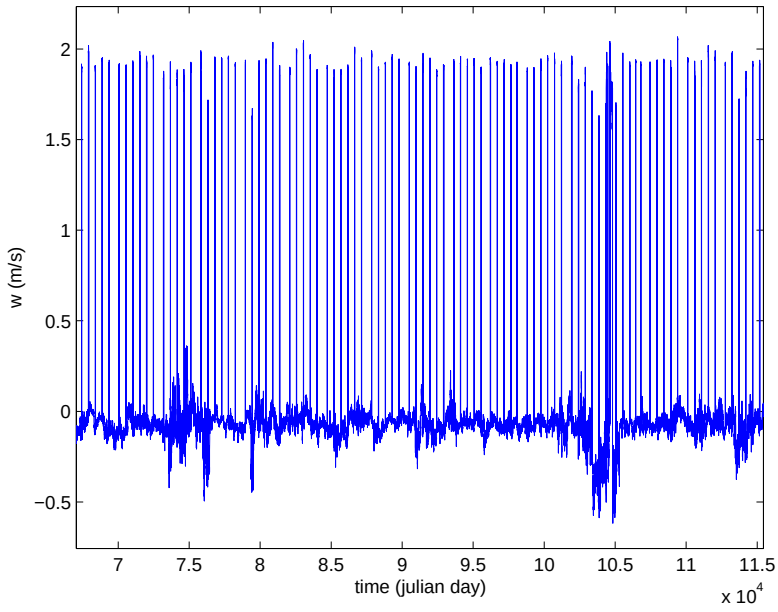

Figure 2.6: Example of spikes in the sonic times series for w-velocity

favourable to recirculation, and at the time of the installation, it was still unclear whether upslope or downslope flow is dominant at this location. Consequently the ultrasonics at site 31, were positioned vertically with the boom parallel to the ridge. Flow distortions can be anticipated for easterly wind.

The vertical velocity time series show a spike that comes with regular frequency, as shown in Figure 2.6, which is due to voltage discharge of the instrument. These spikes are easily recognisable and removed.

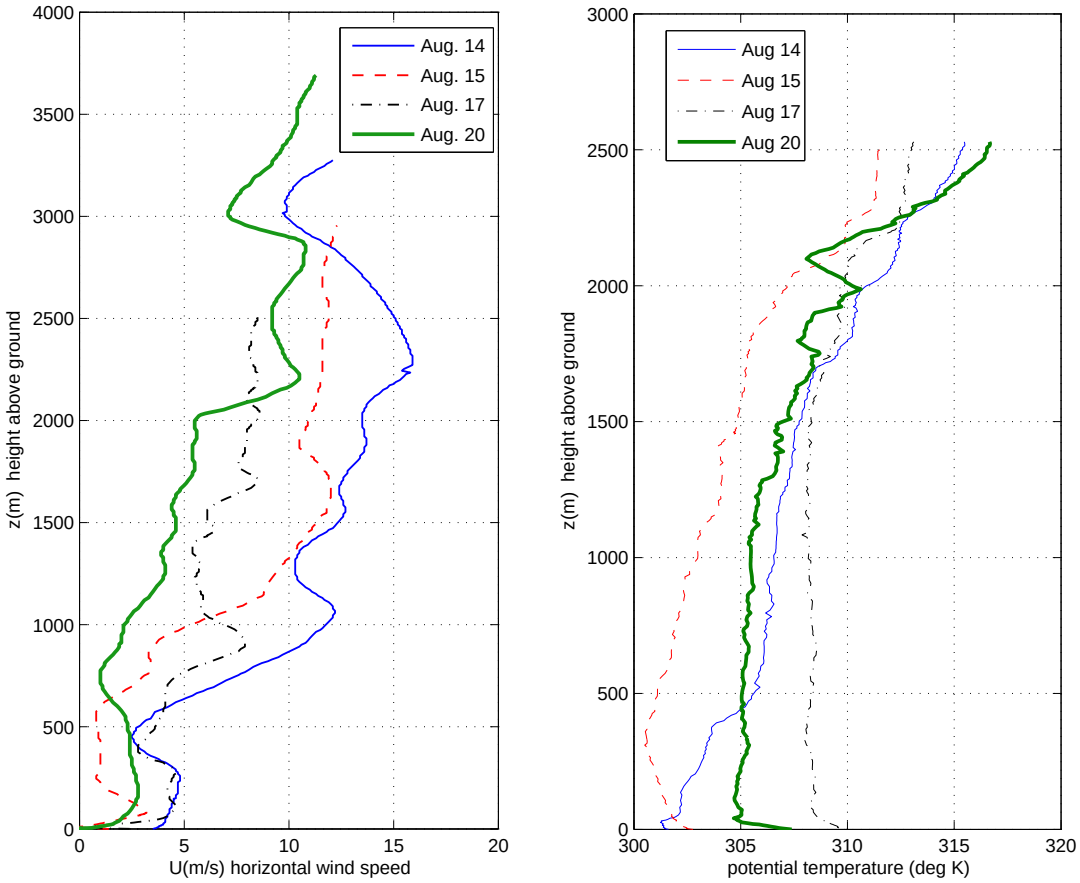

Figure 2.7: Some soundings during the period 11 to 18 August 2003 launched from site 34

The study uses data covering the period 11 to 25 August 2003, which includes the two selected days for the ARPS simulations described in Chapter 4. These two

days have been selected as they are characterised by strong winds, relatively for the summer 2003. The influence of thermal turbulence is hence diminished and to have wind conditions as close as possible as those during a snow storm. More details over the meteorological situation during those days are presented in Chapter 4. According to the local sounding launched every day at 12 UTC from location 34 (See figure 2.3), the atmosphere is stable or near neutral (17 to 20 August 2003), for the considered period : some representative soundings are shown in Figure 2.7.

2.3 Theoretical background

2.3.1 The Reynolds decomposition and averaging rules

The large-scale motion can be separated from the turbulent motions by averaging the wind speeds over a period that lies in the spectral gap of the turbulence spectrum. The velocity is then decomposed into a mean component $\bar{u}$ and a fluctuation u' around this mean, also called the turbulent part, as described in the equation 2.1. This approach was first introduced by O. Reynolds in 1889, and is referred to as the Reynolds decomposition.

$$u(x,y,z,t) = \overline{u(x,y,z,t)} + u'(x,y,z,t) \tag{2.1}$$

The mean $\bar{u}$ represents the part that varies with a period on the order of the averaging time. Turbulence is a three-dimensional phenomenon and the decomposition can be applied to all variables, including v- and w-velocity components.

$$v(x,y,z,t) = \overline{v(x,y,z,t)} + v'(x,y,z,t) \tag{2.2a}$$

$$w(x,y,z,t) = \overline{w(x,y,z,t)} + w'(x,y,z,t) \tag{2.2b}$$

In the atmospheric boundary layer, and over flat terrain, it is admitted that $\bar{w} = 0$. Over steep terrain, it is also valid in the mean streamline coordinates. The decomposition presented in equation 2.1 uses the following property:

$$\bar{u'} = 0$$

This decomposition uses an ensemble average. The ensemble average (formula 2.3) for a discrete variable a is defined as:

$$\overline{(a)}^{e} = \frac{1}{N}\sum_{i=1}^{N} a_i(\vec{x}) \tag{2.3}$$

Where N is the number of realisations of the air flow. However in the atmosphere, N is infinite and a true average cannot be obtained from experimental measurements. We thus have to fix limits to this average, although it raises the question: are such limits equal to ensemble average ? For turbulence that is homogeneous (i.e. invariant in space) and stationary (i.e. invariant statistics in time), the averages in time or space or the ensemble average are assumed to be equal. This is called the ergodic hypothesis as presented in the expression 2.4 (See (Panofsky and Dutton, 1984, chapter 3) for more details).

$$\overline{()}^{e} = \overline{()}^{time} = \overline{()}^{space} \equiv \overline{()} \tag{2.4}$$

The overbar symbol $\overline{()}$ describes a generic average in the following. During field campaigns, data are often recorded at a fixed location, like a tower or a mast, producing a times series of the local atmospheric variables. As a result time averaging is often used in atmospheric turbulence analysis, then the ergodic hypothesis is applied. In order to perform the Reynolds decomposition, this implicitly raises the question of the averaging period. The energy distribution through the scales gives an answer: the energy spectrum of atmospheric turbulence presents a minimum of energy between two maxima at high and low frequencies (See (Stull, 1988, p. 7)). This minimum is called the spectral gap and allows us to separate mean flow and turbulence, by choosing a time average corresponding to this gap. This issue is discussed in the case of the Gaudergrat site in section 2.4.

2.3.2 The Taylor hypothesis

One is often interested in knowing the spatial structure of the atmospheric turbulence, but usually have time series measurements. A way to solve this paradox was proposed by G. I. Taylor in 1838, a hypothesis that is now called after his name: the Taylor hypothesis. The Taylor hypothesis assumes that the turbulence is frozen during the time it travels across the point of observation. The temporal information can easily be transformed into spatial informations, using the mean wind speed:

$$\vec{x} = \vec{U} \cdot t$$

The Taylor hypothesis is of considerable importance in practice as it permits to infer the spatial structure of turbulence from single point measurements. It is valid when the flow is stationary in time and homogeneous in space. Moreover if the

assumption is valid for isotropic or locally isotropic turbulence (i.e. motions statistics are the invariant in all directions), the temporal spectrum represents also the spatial spectrum. These conditions can be approximately satisfied in the atmosphere if the measurement location and period are carefully chosen. As mentioned in Stull (1988), eddies can be considered to have a negligeable change as they are advected past the sensor if the turbulence intensity is small compared to the wind speed. Willis and Deardorff (1976) formulate it more precisely:

$$\sigma_{\mathrm{U}} < 0.5 \cdot U$$

For spectral analysis, the Taylor hypothesis fails for frequencies smaller than $\frac{\partial \bar{u}}{\partial z}$.

2.3.3 Measurement over sloping terrain and mean streamline coordinate

The x-direction is chosen as the eastward axes and the y-direction is the northwards direction. This is the usual choice in meteorology. However this system is not suitable for all terrains. When vector quantities, such as velocities or fluxes, are measured in a coordinate system that does not coincide with the one used for the analysis, problems arise. Over complex terrain, and in particular over Alpine terrain, the flow streamlines are not parallel to the underlying topography. Consequently, for a better understanding and interpretation of the fluctuating velocities or fluxes quantities, the data are transformed in the so-called mean streamline coordinates (Kaimal and Finnigan, 1994, chapter 6).

Close to the ground the wind vector must be parallel to the underlying surface for reasons of continuity. So surface-following coordinates have been used on several occasions. In this referential system, the z-coordinate is locally perpendicular to the surface and x and y coordinates lie parallel to the ground. Terrain following coordinates offer only a partial solution to the problem, as the wind is parallel to the ground only near $z = 0$, at high levels it is almost horizontal and there remains a mismatch between coordinate axes and the wind aloft.

One method to overcome this problem is to work in physical streamline coordinates. In this coordinate system, the x-direction is always along a streamline, i.e. aligned with the local mean wind vector $\bar{u}$, whereas the y and z coordinates are perpendicular to the x-direction. In this framework, the coordinate system is fixed by the flow. This system is a local rectangular Cartesian frame aligned with the local mean streamline and therefore with the physical quantities. The y and z directions are trajectories to the streamline. Consequently the three sets of coordinate

axes forming an orthogonal, curvilinear referential system. In these coordinates, $\bar{v} = \bar{w} = 0$ by definition, so the total velocity vector has the following components : $(\bar{u} + u', v', w')$.

The method used in the following is the triple rotation method and a detailed description of this transformation can be found in (Lewis, 2006, Appendix C). The first step is to compute a mean wind component for u, v, and w time series in a cartesian coordinate system. This step makes immediately clear that the mean component depends on the spatial resolution of the instrument as well as the averaging period. The choice of the averaging period is presented in section 2.4.

In flow over steep terrain with recirculation zones, the use of the mean steamline coordinate may not be the most appropriate system as the streamlines can intercept each other or present sudden direction changes in the lee when flow separation occurs. However no better tool exists nowadays and this framework is still applied. Nevertheless, it can be improved with information concerning the spatial evolution of the flow in order to fix the coordinate directions, the curvature of the streamlines, and the length of acceleration (Kaimal and Finnigan, 1994, chapter 6).

2.3.4 The velocity increment and wind gusts

A measure of turbulence can be given by the ratio of the variance (i.e. the spread of the velocity around its mean) to the mean (Stull, 1988, chap. 2). In the surface layer the turbulence intensity increases as the mean wind speed increases. The turbulence intensity is defined as:

$$I = \frac{\sigma_u}{\bar{u}} \tag{2.5}$$

Where σ_u is the standard deviation, defined as:

$$\sigma_u = (\overline{u'^2})^{\frac{1}{2}} \tag{2.6}$$

As specified in (Stull, 1988), the turbulence intensity I has to be small compared to the mean wind speed (i.e. $I < 0.5$) in order to apply the Taylor hypothesis. However this parameter does not give us any information about the velocity fluctuations dynamically. As introduced by (Böttcher et al., 2003; Lueck et al., 1999), to investigate the wind gust's turbulence, fluctuation differences are computed by the mean of the velocity increment (2.7).

$$\delta u_\tau(\tau) = u'(t+\tau) - u'(t) \tag{2.7}$$

Wind gust are represented by a large value of this increment (Equation 2.7), as long as τ, the time step, is small. Indeed gusts are phenomena with a short life time. Atmospheric winds also show fluctuations on any time scales ranging from less than a second up to several days or more as demonstrated by the wind speed energy spectrum (e.g. show in (Stull, 1988, chapter 2)). Hereafter the velocity increments statistics are presented for several time lags of up to 1800 seconds. Local isotropic and stationary turbulence (e.g. laboratory experiments) presents intermittent probability distribution functions (i.e. with a peak around the mean value and heavy tails) for small value of the time lag τ, whereas for large values of τ the probability distribution functions are rather Gaussian shaped distributions.

The integral time scale T is defined in the equation:

$$T = \int_0^\infty R_u(\tau) d\tau$$

Where $R_u(\tau)$ is the correlation function for the variable u, defined as:

$$R_u(\tau) = \frac{\overline{u'(t)u'(t+\tau)}}{\sigma_u^2}$$

σ_u is the standard deviation of u defined in equation 2.6.

In the atmosphere, the flow is non-stationnary and this leads to too long correlations ranges. Consequently, the integral time scale cannot be estimated properly.

2.4 Results for the Gaudergrat Experimental site

2.4.1 Averaging period specific to the Gaudergrat site for the data rotation in the mean streamline coordinates

In the analysis atmospheric measurements analysis, the Reynolds decomposition is often performed with an averaging period between 10 minutes to one hour. This averaging period is more or less chosen arbitrarily, even if this time should belong to the so-called spectral gap, as introduced by van der Hoven in 1957. The existence of such a gap between large synoptic scales and small scale or turbulence is still discussed (Eggleston and Clark, 2000). Over complex mountainous terrain, it is not certain where this minimum of energy is located.

In this study, the spectra of quality controlled but non-rotated data is constructed in order to check where the minimum of energy lies for such a topography, hence provides an averaging period for the following analysis.

The power spectra are computed using two weeks of data from the ultrasonics (sites 31, 32 and 33, as shown in Figure 2.3) between the 11 and 25 August 2003. The spectra obtained from the non-rotated data are presented figure 2.8. It is quite difficult at some sites to define a precise spectral gap. The extension of the spectra to the lower frequencies did not provide better results (the spectra become more difficult to read as the number of spectra averages diminishes). However one can see a tendency to a minimum around 10^{-3}Hz, which corresponds to about 15 minutes. This averaging times is consitent with the spectral gap predicted by the theory for flat and homogeneous terrain.

For site 32, at the ridge top, the spectra of the v-component show really little energy at all scales. This can be explained by the fact that the wind is channelled perpendicularly to the ridge at this location as explained in Lewis (2006).

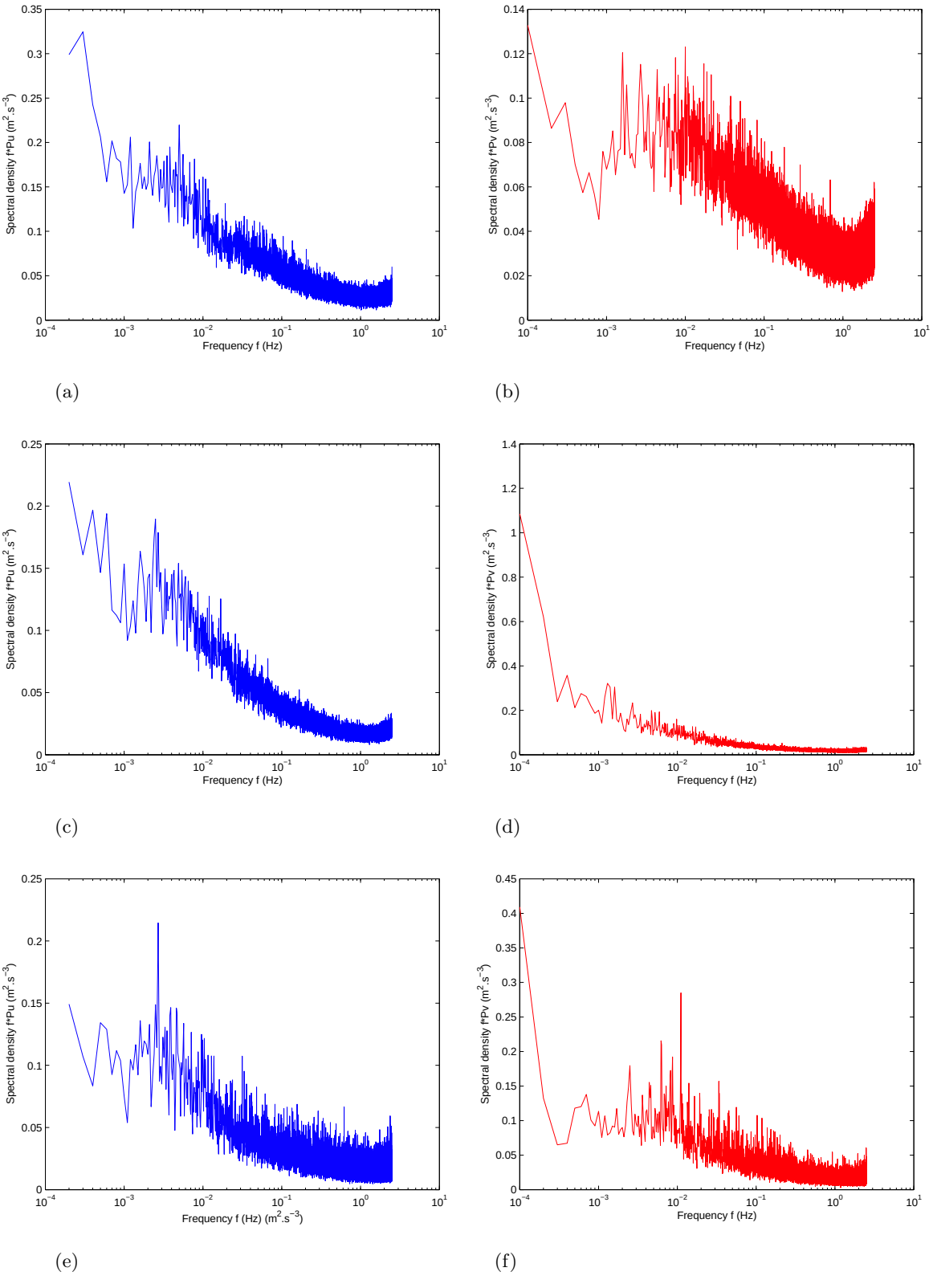

Figure 2.8: Power spectra of sonic raw data (non rotated) of the u- (left column) and v- (rigth column) velocity components, at site 31 (a,b), site 32 (c,d) and site 33 (e,f)

For the rotation into the mean streamline coordinates, two averaging times are then tested: 10 and 30 minutes. The choice of this averaging time is important although not strongly influencing the rotated values. Indeed the rotated data obtained from both averaging time may differ up to 10m/s, however more than 95% of the data does not differ more than 1m/s (Not shown).

Consequently in the following the averaging time is set to 10 minutes for the rotation into the mean streamline coordinates.

2.4.2 Atmospheric wind speeds statistics

Many meteorological applications of wind assume a Gaussian process, but it is not the case for atmospheric wind fields as it has been shown by Böttcher et al. (2003). The study of the probability distribution functions (noted PDFs hereafter) gives information on the transition from Gaussian distributions to intermittent distributions which present the so-called "heavy-tailed distributions".

As reported by Böttcher et al. (2003), calculating the PDFs of velocity increments for fixed mean velocity classes allows the atmospheric PDFs to compare well with the laboratory experiment PDFs. The datasets used in Böttcher et al. (2003, 2006) contain one dataset acquired in a wind tunnel, two datasets obtained over flat and rather homogeneous terrain, one dataset recorded offshore, and one dataset for more complex terrain (Oberzeiring, Austria). The last four datasets were measured in the atmospheric surface layer at height between 6 and 20 meters. The Gaudergrat dataset gives the possibility to extend their study to complex mountainous terrain.

Velocity increments, as defined in section 2.3, are used for the wind gust statistic analysis during Gaudex.

In this study, turbulence data recorded at sonics sites during the Gaudex 2003 field campaign are used (as described in section 2.2). The analysis is focused on the period Aug. 11 to 25, 2003, which covers the two days chosen for the ARPS simulations (chapter 4). The data are decomposed into two datasets of one week and for each site. A description is given in table 2.1. All data are recorded with a sampling frequency of 5 Hz and at a heigth of 7.5 meters above the surface.

It has been shown previously that the influence of the averaging time for the rotation has no influence on the results. This point has been also checked and all PDFs of velocity increments are similar, for a given location, independently of the averaging time. An example is given in Figure 2.9. Hereafter the figures are

Parameter	11-17 August 2003			18-25 August 2003		
	site 31	site 32	site33	site 31	site 32	site33
Nb of data points	3024000	3024000	3024000	3024000	3024000	3024000
$\bar{u}(m/s)$	0.68	0.37	0.72	-0.5	0.65	0.51
$u_{min}(m/s)$	-10.78	-11.19	-5.25	-9.42	-7.58	-7.34
$u_{max}(m/s)$	6.16	18.85	5.60	6.15	15.9	6.16
Variance (m/s)	4.95	4.50	1.08	1.5	2.83	3.17

Table 2.1: Datasets characteristics (before rotation, after quality control)

presented with a 30-minutes averaging time for the mean stream line coordinate transformation.

In figure 2.10, PDFs of u-velocity increment are presented for the the 3 sonics sites, and for different values of τ. Independent of the sonic location, the PDFs present all the so-called heavy-tails that indicates high intermittency. The distributions are scale dependent: for smaller scales, the distributions are even more intermittent. This differs from the theoretical Gaussian distribution that is expected for isotropic turbulence or as can be found for laboratory experiments. Also for a large range of scales, the distributions shape remains similar but significantly different of the PDFs shape from isotropic turbulence. Experiments with isotropic turbulence show taht the PDFs shape changes with the scales, and for large scales the distributions are Gaussian. By contrast, our observations show that the wind on Gaudergrat are constantly intermittent over all the scales presented here. As mentioned in Böttcher et al. (2003), the shape of these PDFs is found to be robust over the different scales which seems to contradict the mathematical concept of stability where the Gaussian distribution is the limiting one. Normal distribution arises to be the limiting distribution in the statistics or probability theory and has the property of being a stable distribution. Stable here means that a number of random variates that are in the same group, any linear combination of these variates will also be in the same group. Consequently if the distributions of wind speeds can be limited by a Gaussian, it is easier to predict the occurence of wind gust for any location.

In addition, at site 31 (west slope), it can be noticed that for a given time lag τ, the PDF slope tends to be more flat than at the two others locations, indicating more intermittency. Indeed on this side of the ridge, flow seperations are more frequent

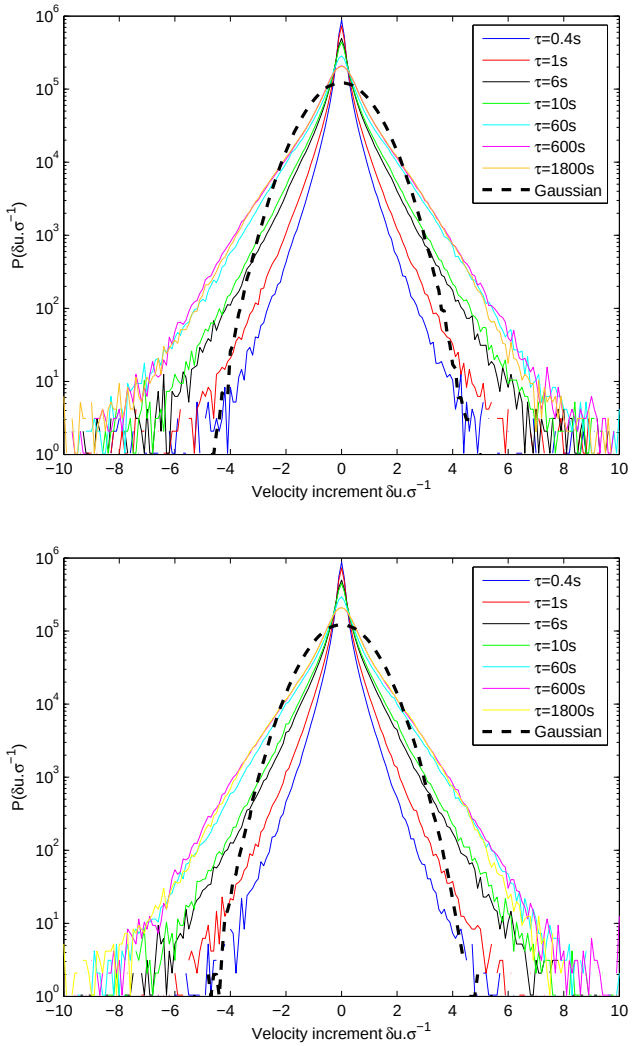

Figure 2.9: Probability distribution of the u-velocity increment at site 31 (east) using rotated data with 10 minutes (above) and 30 minutes (below). The Gaussian distribution (dashed black line) is given for $\tau = 1800s$

due to prevailing westerly to northwesterly winds. At the crest and on the upwind slope, the flow is channeled and accelerated (Venturi effect, as shown in Figure 4.10, Chapter 4) which also leads to a more laminar flow. The heavy tails observed for the larger time lag (τ of the order of 600s) can be observed at the crest (site 32) and on the east slope (site 31), which correspond to non-local strong winds.

The triple rotation method has been applied to the sonic data, as described in section 2.2, consequently the v- and w-velocity components consist only of the fluctuations and classifying the data based on the mean velocity is hardly applicable to the PDF of v- and w-velocity components. Thus the following study is focused on the u-velocity component, An example of v- and w-velocity increments distributions is shown respectively for site 33 (west slope) and 31 (east slope) in Figure 2.11. The bounds in vertical velocity PDF at $\pm 1.5 m/s$ are due to the rotation in the meanstream line coordinate system where only the fluctuations of the vertical velocity are kept. This PDF show a high intermitency, which is the consequence of the generation of vortices with an horizontal axes.

Böttcher (Böttcher et al., 2006) found that the atmospheric turbulence is similar to laboratory turbulence (homogeneous) when the velocity increments are classified in categories based on the mean wind speed, and they interpreted intermittent distributions as a composition of subsets of isotropic turbulence. In the case of the Gaudex, it is interesting to see if this assumption works over a more complex terrain such as a steep ridge.

Figure 2.12 shows PDFs of the u-velocity increments classified depending on the mean wind component : the PDFs tend to a Gaussian distribution, independent of the site location, i.e. windward or leeward slope. It is also noticeable that the distributions are even more similar to Gaussian when the time lag is larger, for example τ=600s or 1800s. Wind gusts are identified as a large velocity rise during a short time, and time lags larger than a few minutes can be considered as a large scale fluctuations. According to this definition, larger scale fluctuations converge better to a Gaussian distribution. However even if the PDF becomes bounded by a Gaussian distribution for small increment values, gusts with large increments values (about $\pm 8 m/s$) are still possible. this indicates that they are still some discrepancies with homogeneous turbulence. In addition, the narrower the mean velocity interval is, the better the conditioned PDFs of velocity increments fit the Gaussian distribution, as shown in comparison of figure 2.13 where the mean velocity range is $\bar{u} \pm 1 m/s$, with figure 2.12 where the mean velocity range span over $\bar{u} \pm 0.5 m/s$. A narrower range tends to represent one scale of motion, and this result indicates that the different scales individually respect homogeneous turbulence theory.

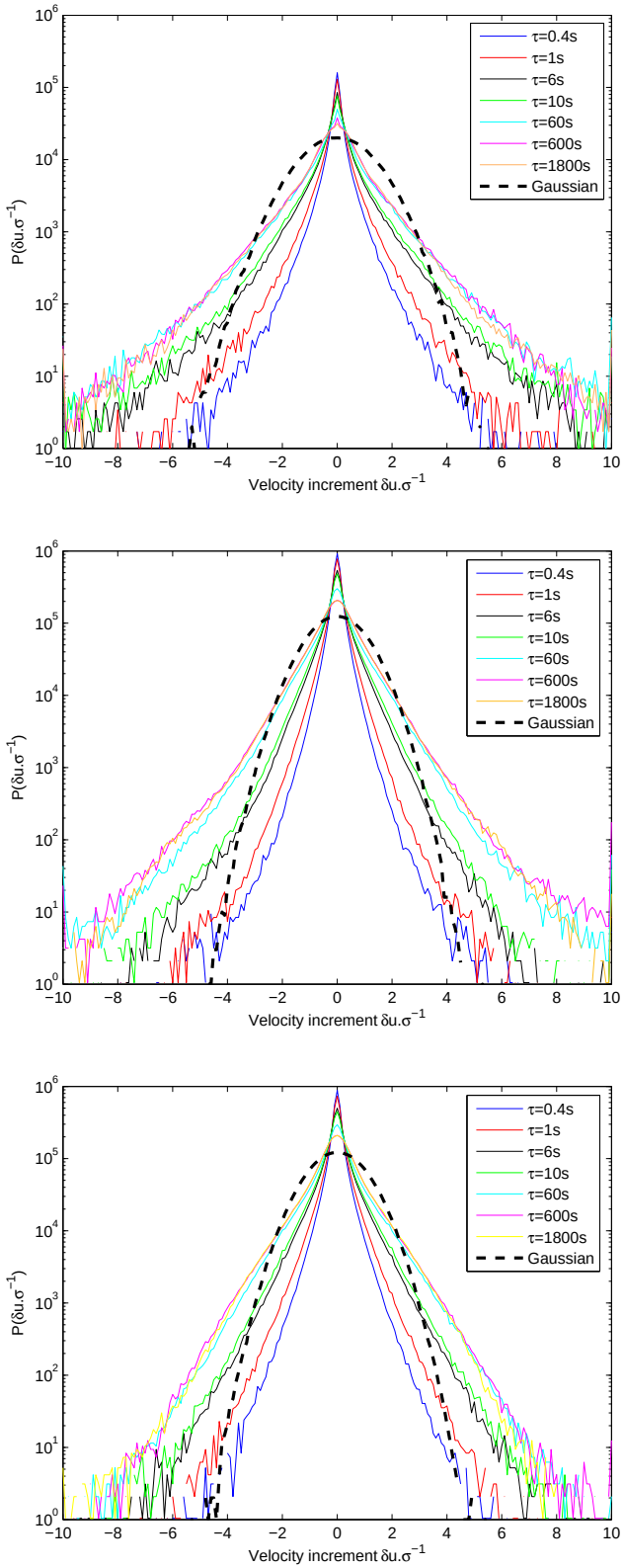

Figure 2.10: Probability distribution of the u-velocity increment at site 31 on the east slope (above), site 32 at the top (middle) and site 33 on the west slope (below). The Gaussian distribution (dashed black line) is given for $\tau = 1800s$

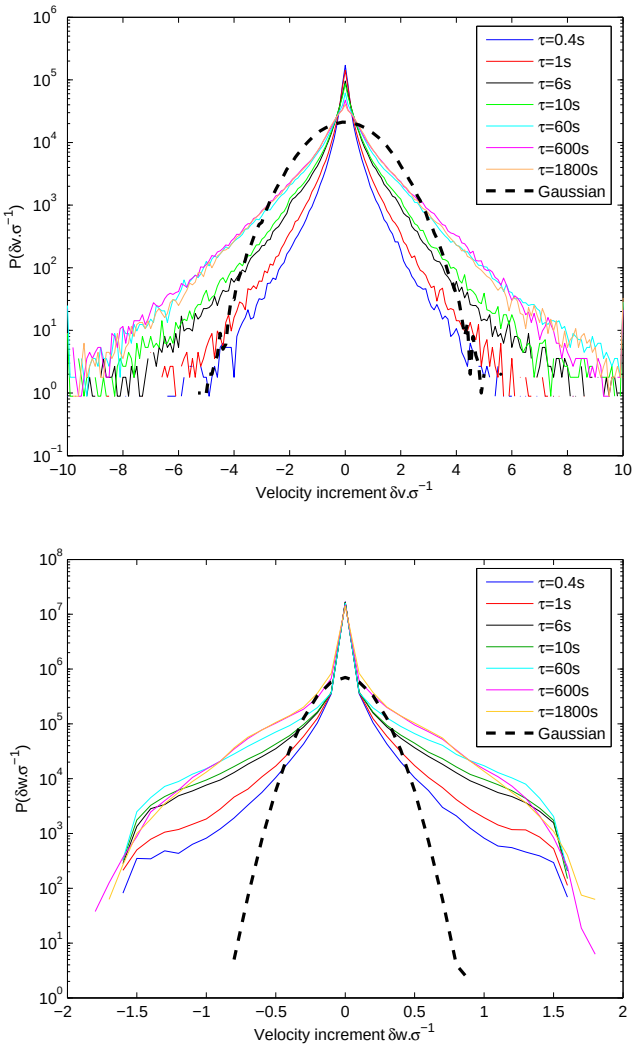

Figure 2.11: Probability distribution of the northward velocity increment at site 33 (above) and the vertical velocity increment at site 31 (below). The Gaussian distribution (dashed black line) is given for $\tau = 1800s$

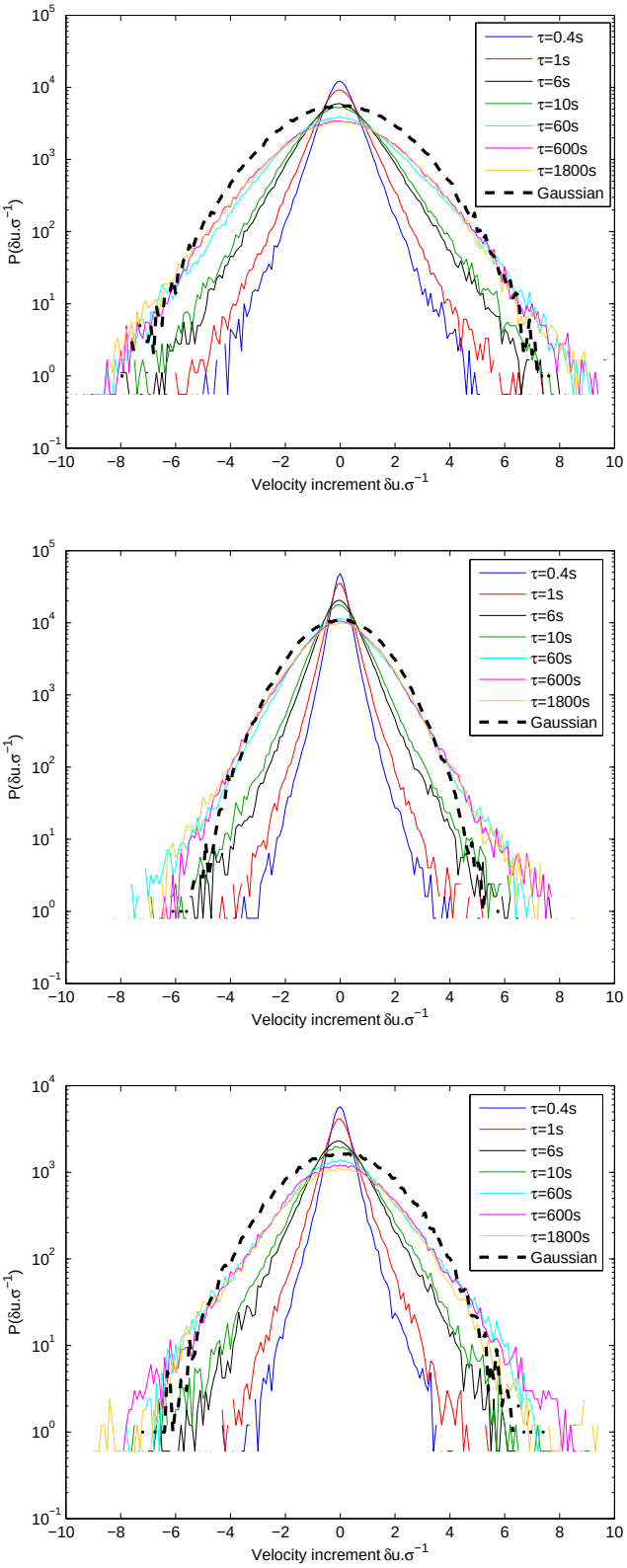

Figure 2.12: Probability distribution of the u-velocity conditioned depending on their mean wind speed : $\bar{u} = 3m/s \pm 0.5m/s$, at site 31 (above), site 32(middle), site 33(below). The Gaussian distribution (dashed black line) is given for $\tau = 1800s$

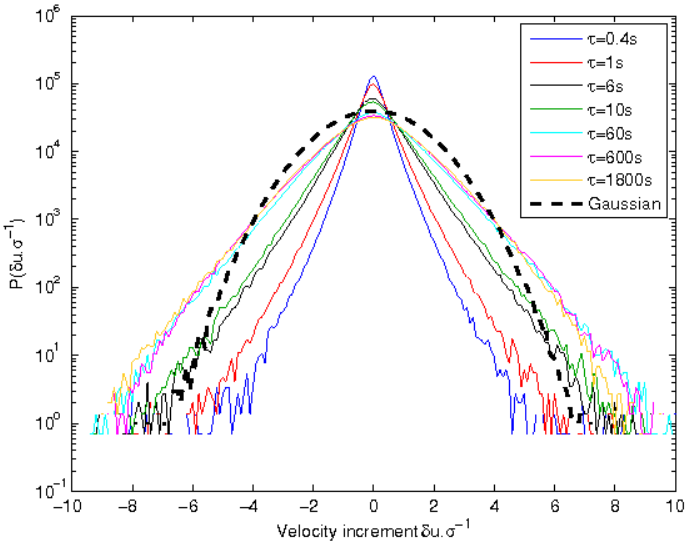

Figure 2.13: Probability distribution of the u-velocity increments at site 31. The mean wind interval on wich the u-velocity increments are conditioned is $\bar{u} \in [3,4]m/s$. The Gaussian distribution (dashed black line) is given for $\tau = 1800s$

2.4.3 Spectral analyis of the turbulence at the Gaudergrat

The statistical analysis informed us on the repartition in time of the gusts and lead to the deduction that over complex heterogenous terrain, the turbulence can be seen as a composition of subsets of isotropic turbulence. In this section, a spectral analysis of the turbulence structure at the Gaudergrat ridge is performed to check this assumption. The ultrasonic data rotation in the mean streamline coordinate has been investigated using two averaging periods. However the choice of one or the other time does not influence the distribution of energy through all the scales. The only difference is more scatter in the fluctuations calculated from the 10 minutes averaging time. For example the spectra of u-velocity obtained with 10 or 30 minutes averaging times are similar as can be seen in Figure 2.14. Thus an averaging period of 10 minutes is chosen in the following analysis.

On both sides of the ridge, and at the top, the spectra of the u- and v-velocity components (figure 2.15) show a similar distribution of energy with a transition from the production range to the inertial subrange occuring at about $f \approx 4.10^{-2}Hz$.

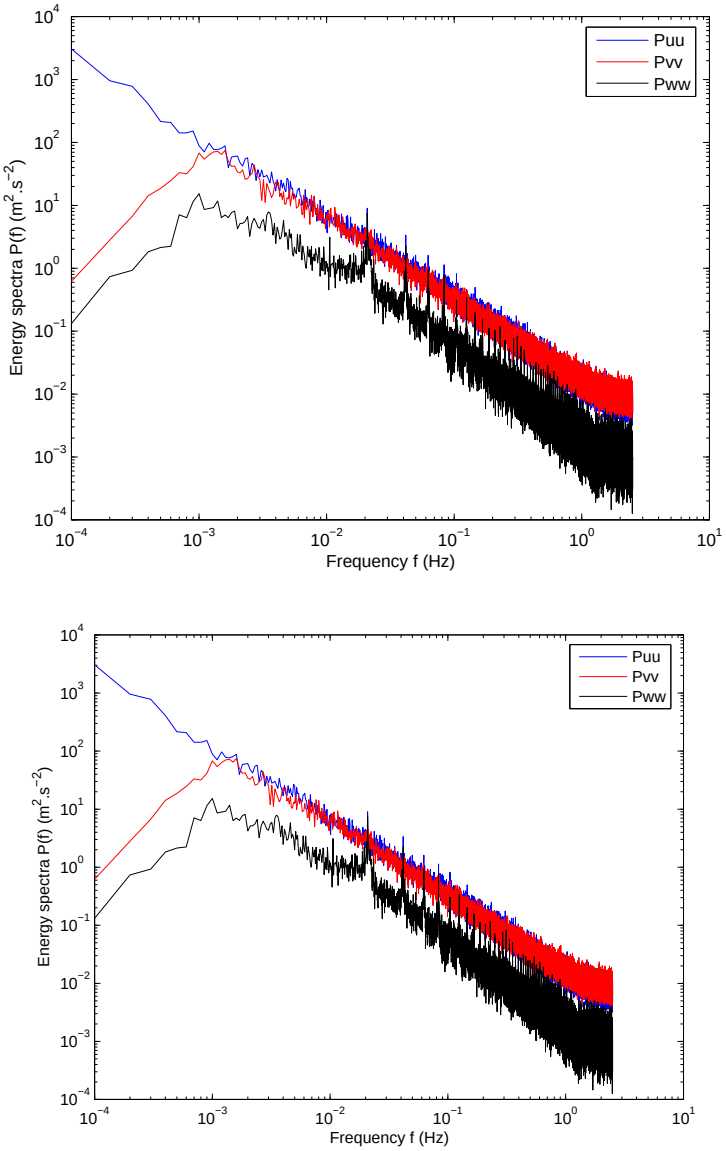

Figure 2.14: Spectra of the velocity components at site 31 (east), obtained from data rotated with an averaging time of 10 minutes (above) and 30 minutes (below)

This corresponds to a size of eddies of $50m$, for a mean total velocity of about $2m/s$. Also, in the production range, there is slightly more energy at the crest. The w-velocity components spectra (figure 2.15) are similar for all sites, whereas they

contains less energy than those of the u and v components, in the production range. This effect is also observed over flat homogeneous terrain, for example during the Kansas experiment (Kaimal et al., 1972). For the vertical velocity, the transition from production range to the inertial subrange appears for eddies larger than those for the horizontal velocity components at $f \approx 10^{-2}Hz$, i.e. for eddies of size about $32m$. The transition to the inertial subrange appears for smaller scales in the w-velocity spectra than in the longitudinal velocities spectra. This indicate that the production range contains smaller scales.

The spectra shown in Figure 2.15 follow the Kolmogorov $f^{-5/3}$ energy decrease for isotropic homogeneous turbulence only over a very limited range of scales. However, when the spectra are plotted for data conditioned in mean wind speed intervals, the spectra respects the inertial subrange $f^{-5/3}$ law, over a larger range of scale, as can be seen in Figure 2.16, where the u-velocity spectra are presented for a mean wind speed interal $\bar{u} \in [2, 3]m/s$. This observation confirms that the turbulence observed in the atmospheric boundary layer is a superposition of different scales that individually respect the theory for isotropic turbulence .The production range where the energy decrease follows the f^{-1} law extends over a larger range of scales and the transition to the inertial subrange occurs at $f \approx 4.10^{-2}Hz$, i.e. for eddies of size about 50m. The eddy size in the production range are smaller when the wind speed are classified depending on their mean component.

Turbulent kinetic Energy (TKE) is an interesting parameter when studying flow over slopy terrain. Indeed it can be treated as the trace of the Reynolds stresses matrix, and by definition is invariant in any coordinate system. For this reason the raw data can be used without transformation in the mean streamline coordinate. The spectra for the TKE per unit mass on both sides of the ridge and at the top are presented in Figure 2.17. Independently of the site, the energy decrease follows the $f^{-5/3}$ law in the inertial range as observed for isotropic turbulence over flat homogeneous terrain. Moreover, in the inertial range, the amount and the distribution of energy is roughly the same for the west side and at the crest, but there is more energy at these scales on the east side. The turbulence on the east slope is hence more influenced by small scale, local turbulence. In contrast, in the production range, there is more energy at the ridge crest (site 32), indicating that this location is more influenced by larger scale turbulence, coming from the surrounding mountains wake or the synoptic wind. The transition from production range to the inertial subrange is difficult to interpret as an eddy size, as it is a sum of velocities.

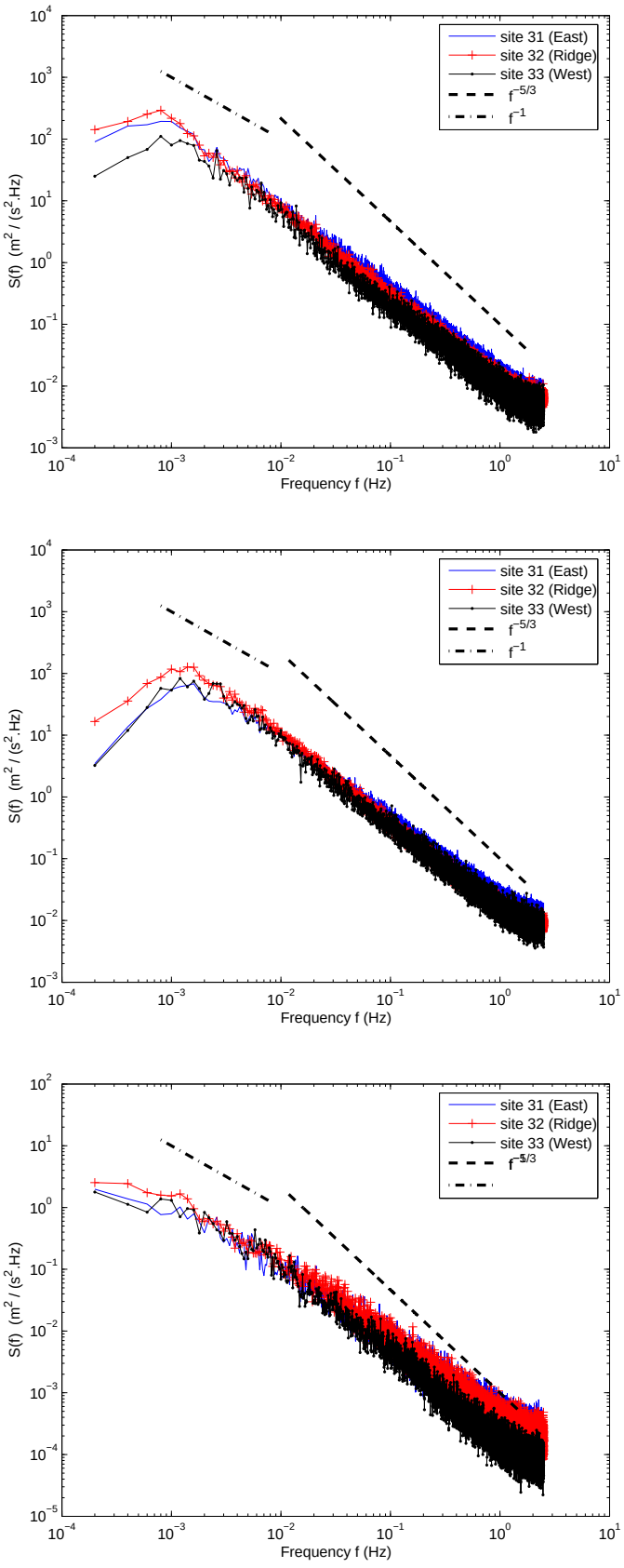

Figure 2.15: Spectra of the u-, v-, and w-velocity component, respectively from top, at all sonics sites. The data used have been recorded from 11 to 25 August 2003

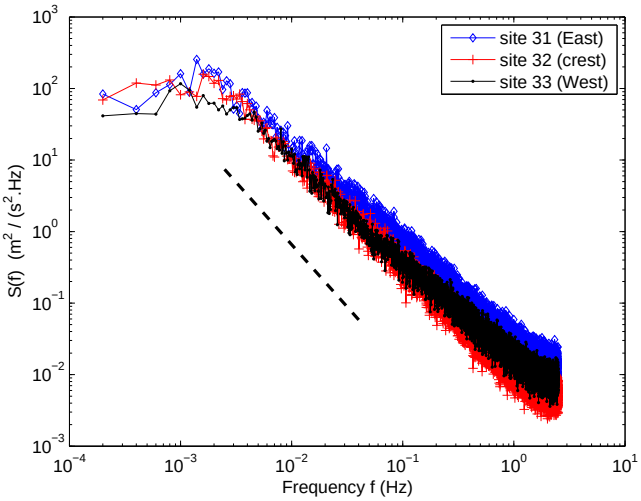

Figure 2.16: Spectra of the u- velocity component at all sonics sites, period 11 to 25 August 2003. A condition on the maen wind speed is applied ($\bar{u} \in [2,3]m/s$)

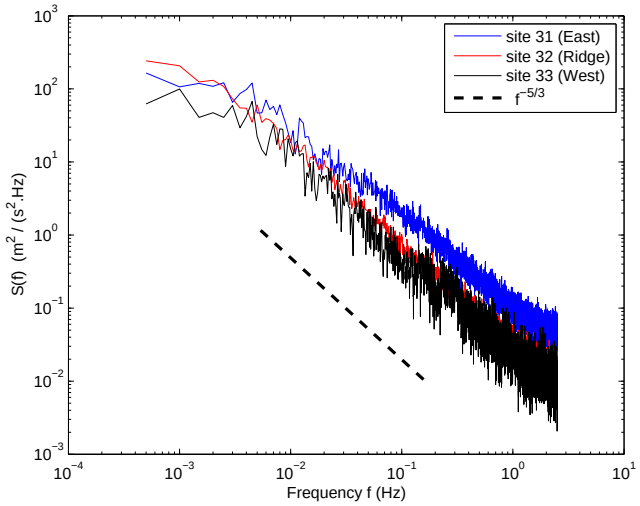

Figure 2.17: Spectra of the TKE per unit mass at all sonics sites, period 11 to 25 August 2003

2.5 Conclusion

Intermittency can be investigated in several ways. The analysis presented here is based on the approach discribed by Böttcher et al. (2003)and shows that the wind gusts are highly intermittent at the Gaudergrat ridge, independently of the location, and there is a high probability of strong gusts. These intermittent distributions remain robust over several scales. By conditioning the velocity increments into mean wind speed intervals, it is possible to find an analogy between local isotropic turbulence and atmopheric turbulence, on each side of the ridge as well as at the top. The hypothesis of Böttcher et al. (2003) is observed at the Gaudergrat on the lee slope as well as on the windward slope. This is an interesting result for the modelling of atmospheric turbulence as isotropic turbulence statistics are better known. Indeed if the composition of the isotropic subset is known, it should be possible to model atmospheric wind speed satististics, with relative ease.

The stratification conditions during this period were either stable or near neutral when the wind was stronger. However the change in stratification did not influence the results. Only the condition on the mean wind velocity has an influence. Even if the PDFs obtained from conditioned velocity increment are more consistent with Gaussian distribution the production of turbulence is not continuous as it assumed in many theoretical formulations.

In order to check if this conclusion applies to all type of stratifications, the study could be extended to days during the Gaudex, with a purely convective situation.

The turbulence over the Gaudergrat ridge, at the crest as well as on each side presents similarities to the theoretical turbulence over flat homogeneous terrain when the velocity measurements are rotated in the mean streamline coordinates. The turbulence in the windward side and at the crest present more energy at larger scales that indicate a larger influence of the surrounding mountain wakes or the synoptic airflow, whereas the turbulence on the lee side is more locally influenced.

This study shows that the traditional scaling and averaging laws developed for homogeneous horizontal surfaces can b applied to complex terrain under certain conditions. The heterogeneous surface conditions are likely to create additional length and time scales to generalize the statistical properties.

Chapter 3

Neutral boundary layer simulations with ARPS

3.1 Introduction and background

During a snow storm, the strong winds yield a well mixed atmospheric boundary layer. The theoretical study of the boundary layer development under a neutral atmosphere is thus well representative of the processes that take place in the atmosphere during a drifting snow event. It is important to characterise the turbulence in the surface layer as it is responsible for energy distribution and influences exchanges and mass transport. Moreover, computations of the flow in a neutral atmosphere over a rough wall is well documented in the literature (Deardorff, 1972; Porté-Agel et al., 2000) and is a standard way to test the mechanical turbulence model of ARPS.

In a neutral boundary layer, the velocity profile should be logarithmic in the surface layer. However a well-known weakness of the eddy-viscosity models, such as the one used in ARPS, is their failure to reproduce a logarithmic profile in the near-wall region : velocity is too low at the wall and too high further away from the wall and the shear is then overpredicted.

The subgrid scale motions are assumed to be universal and can be parametrised using simple SGS model, provided most of the turbulent energy is present in the large resolved scales (Sagaut, 2002). However, near the wall, the turbulence becomes more anisotropic and the spatial resolution is not sufficient as the energy containing scales become smaller.

This chapter presents the ARPS results for a neutral boundary layer over flat homogeneous terrain, hence the analysis focuses on the mechanical turbulence. The aim is firstly to evaluate the capacities of ARPS in the modelling of turbulence and the repartition of the energy of the flow among the different scales by mean of a spectral analysis and compare with the literature and theory. Secondly, it is a possibility to investigate the turbulence over flat terrain in order to understand the influence of a real topography on the airflow as presented in Chapter 4. Finally, the simulations presented in this chapter will also permit to tune several model parameter values and coefficients related to turbulence for the computations over real topography.

A general overview with a description of the numerical experiment is given in section 3.2, the model set-up is explained in section 3.2, and the results and sensitivity analysis are presented in section 3.3.

3.2 Model overview

The Advanced Regional Prediction System (ARPS) is a meteorological model developed by the Center for Analysis and Prediction of Storm (CAPS) at the University of Oklahoma (Xue et al., 1995, 2000). It was first conceived for the prediction of storms, i.e. phenomena with a scales of a few kilometers, but recent studies have shown that it can also be used for microscales airflow simulations (Chow et al., 2006; Raderschall et al., 2008, submitted; Weigel et al., 2006), which is more suitable for LES computations.

ARPS computations rely on the conservation equations for momentum, heat, mass, water substance (vapour, liquid, ice) and the equation of state of moist air. Among the three state variables, ARPS predicts the potential temperature θ_v and the pressure p, the density ρ is then deduced using the equation of state. This set of equations is completed by initial and boundary conditions and a sub-grid scale model, the formulation of which depends on the problem. The equations are written for a compressible gas, and some terms can be neglected due to low Mach number.

In ARPS, all the equations are written in a curvilinear coordinate system (ξ, η, ζ), which is locally Cartesian. The vertical transformation allows grid stretching, and several options are available in ARPS. In all the presented computations, a tangent hyperbolic function is chosen in order to have more refinement near the surface. It is possible to flatten the levels above a certain height, in order to eliminate

the errors associated to the computations of horizontal gradient on a non-orthogonal grid. The grid is generated numerically and can be arbitrary. The only requirement is that the second level conforms to the terrain. The first level is below the surface. All the equations are discretised on a stagerred grid, the so-called Arakaw C-grid.

The set of equations is formulated to describe perturbations around an undisturbed base state. The base state is assumed to be horizontally homogeneous (i.e. function of z only), hydraulically balanced and time invariant. The base state mass and wind fields are generally not in a geostrophic balance except when the base state wind is zero. Hence any variable Ψ can be expressed:

$$\Psi(x, y, z, t) = \bar{\Psi}(z) + \Delta\Psi(x, y, z, t)$$

where $\Delta\Psi(x, y, z, t)$ is the deviation from the base state $\bar{\Psi}(z)$.

ARPS can be set in a Large-Eddy Simulations (LES) configuration. The equations are filtered in order to separate the large scales and the smaller scales, thus the variable Ψ can also be decomposed as:

$$\Delta\Psi(x, y, z, t) = \widetilde{\Delta\Psi}(x, y, z, t) + \Delta\Psi'(x, y, z, t)$$

where $\widetilde{\Delta\Psi}$ represents the large or resolved scales of the variable $\Delta\Psi$ after filtering using the grid size Δ as the characteristic length of the filter. $\Delta\Psi'(x, y, z, t)$ represents the small scales which are parametrised. The filter size determines the limit between the larger scales, resolved explicitly, and smaller scales, called subfilter scales which are parametrised. The subfilter scales (SFS) can be divided into resolved subfilter scales (RSFS), and unresolved subfilter scales : the sub-grid scale (SGS). The RSFS can be reconstructed, whereas the SGS must be modeled. The reconstruction of the resolved subfilter scales are difficult when the equations are explicitly filtered (Chow, 2004, chapter 6). In addition the stress produced near the bottom boundary by the filtering process is not well-defined and the shear stress is often over-predicted in the near wall region.

In ARPS, the filtered equations are solved in the physical space using finite differences and by consequence the the equations are explicitly filtered. ARPS is built to handle irregular terrain, consequently spectral methods are not possible. The discretisation on the grid leads to an implicit filtering, the filter is by consequence unknown and different for each term in the equations, depending on the numerical scheme. The contribution of the RSFS is ignored although it is reported that the

RSFS are important for neutrally or stably-stratified atmospheres (Chow, 2004, chapter 6).

In any LES model, the SGS have to be modeled to estimate the subgrid fluxes $\widetilde{u_i' u_j'}$ and $\widetilde{u_j' \theta_v}$. ARPS gives the possibility to choose between two types of sub-grid scale (SGS) models (Xue et al., 1995, chapter 6.3). The first-order Smagorinsky-Lilly model which takes into account the stratification (Lilly, 1962; Smagorinsky, 1963), and the 1.5 order Turbulent Kinetic Energy (1.5 TKE)(Deardorff, 1980; Moeng, 1984).

3.2.1 Smagorinsky-Lilly turbulence closure

In the Smagorinsky model it is assumed that the SGS fluxes are proportional to the resolved velocity strain tensor $\widetilde{S_{ij}}$ and the temperature gradient, through the SGS mixing coefficients for momentum K_m and heat K_h, also called respectively eddy-viscosity and eddy-diffusivity. The strain tensor is computed from the large velocity scales (equation 3.1):

$$\widetilde{Sij} = \frac{1}{2}\left(\frac{\partial \widetilde{u_i}}{\partial x_j} + \frac{\partial \widetilde{u_j}}{\partial x_i}\right) \tag{3.1}$$

Since the strain tensor is expected to be maximum near the surface, the mixing coefficient for momentum (eddy-viscosity) is expected to be also maximum there, leading to an overestimation of the energy dissipation.

$$\widetilde{u_i' u_j'} = \frac{2}{3}\widetilde{u_k' u_k'}\delta_{ij} - K_m \widetilde{Sij} \tag{3.2}$$

$$\widetilde{\theta' u_j'} = -K_h \frac{\partial \widetilde{\theta_v}}{\partial x_j} \tag{3.3}$$

The modified Smagorinsky SGS closure, called Smagorinsky-Lilly (Lilly, 1962), takes into account the stratification in the formulation of the momentum mixing coefficients K_m (equation 3.4) by use of the Brunt-Väisälä frequency N (equation 3.5) that may reduce significantly the mixing coefficient :

$$K_m = (C_k \Delta)^2 [\, max\,(\, \sqrt{2(\widetilde{S_{ij}})^2 - N^2/Pr_t}\,,\, 0\,)\,]^{1/2} \tag{3.4}$$

Where Pr_t is the turbulent Prandtl number, defined as in equation 3.10.

$$N^2 = \frac{g}{\theta_v}\frac{\partial \widetilde{\theta_v}}{\partial z} \tag{3.5}$$

C_k is the Smagorinsky coefficient set to 0.21 over the whole domain, as defined by Deardorff (Deardorff, 1972) and Δ is a measure of the grid size. For a grid with similar spacing in all directions,

$$\Delta = (\Delta x \Delta y \Delta z)^{1/3} \tag{3.6}$$

the turbulence is nearly isotropic, the mixing coefficients for momentum in horizontal and vertical are equal : $K_{mh} = K_{mv} = K_m$.

In the case of large aspect ratio $\Delta x/\Delta z$ (i.e. order of 10 or larger), the turbulence is considered as anisotropic, and to avoid an excessive vertical mixing, different length scales are used and the horizontal and vertical mixing coefficients are defined:

$$K_{mh} = (C_k \Delta_h)^2 [\, max\,(\, \sqrt{2(\widetilde{S_{ij}})^2 - N^2/Pr_t}\,,\, 0\,)\,]^{1/2} \tag{3.7}$$

$$K_{mv} = (C_k \Delta_v)^2 [\, max\,(\, \sqrt{2(\widetilde{S_{ij}})^2 - N^2/Pr_t}\,,\, 0\,)\,]^{1/2} \tag{3.8}$$

Where Δ_h and Δ_v are the horizontal and vertical grid spacing:

$$\Delta_h = (\Delta x \Delta y)^{1/2} \qquad \text{and} \qquad \Delta_v = \Delta z \tag{3.9}$$

This mixing coefficient for heat is linked to the one for momentum through the turbulent Prandtl number Pr_t:

$$K_h = K_m / Pr_t \tag{3.10}$$

3.2.2 The 1.5 order TKE turbulence closure

The second possible closure is the 1.5 order TKE (Deardorff, 1980; Moeng, 1984). It is also based on the Smagorinsky model where the SGS fluxes are proportional to the velocity strain tensor (see equation 3.2) but an extra prognostic equation for the subgrid TKE is solved. This equation represents the transport of the TKE by the large scale velocities. Indeed a significant amount of energy is produced near the ground but is not necessarily dissipated there. The equation of transport based on the work of Moeng (1984), and is defined in equation 3.11. The TKE is noted e.

This equation is given in Cartesian coordinates for clarity, however in ARPS computations it is transformed in the terrain following coordinates.

$$\frac{\partial e}{\partial t} + \widetilde{u_j}\frac{\partial e}{\partial x_j} = \underbrace{K_h\widetilde{\rho}\frac{g}{\theta_{v0}}\frac{\partial\widetilde{\theta_{v0}}}{\partial z}}_{a} - \underbrace{\widetilde{\rho}K_m\widetilde{S_{ij}}^2}_{b} + \underbrace{\frac{\partial}{\partial x_j}(2K_m\frac{\partial e}{\partial x_j})}_{c} - \underbrace{\varepsilon}_{d} \tag{3.11}$$

The terms in this equation describe the physical processes that create or dissipate turbulence : SGS buoyancy production (a), SGS shear production (b), diffusion of e (c), and viscous dissipation rate of e (d) which is parametrised using the Kolmogorov hypothesis :

$$\varepsilon = C_\varepsilon\frac{e^{3/2}}{\ell} \tag{3.12}$$

The constant C_ε is expressed after Deardorff (1980) and Moeng (1984):

$$C_\varepsilon = \begin{cases} 3.9 & \forall z > 2, \\ 0.19 + 0.51\dfrac{\ell_j}{\Delta} & \text{for } z = 1 \text{ or } 2. \end{cases} \tag{3.13}$$

Where j stands for horizontal or vertical directions, and z is the vertical level.

The SGS fluxes using this closure, are defined as:

$$\widetilde{u_i'u_j'} = \frac{2}{3}e\delta_{ij} - K_m\widetilde{Sij} \tag{3.14}$$

$$\widetilde{\theta'u_j'} = -K_h\frac{\partial\widetilde{\theta_v}}{\partial x_j} \tag{3.15}$$

In the 1.5 order TKE SGS model, the mixing coefficient is related to a mixing length ℓ and a velocity scale deduced from the SGS TKE instead of velocity strain tensor as in the Smagorinsky SGS model. The formulation of the mixing length depends on the stratification. The mixing coefficients for momentum (equation 3.16) and heat (equation 3.17) are expressed:

$$K_{mh} = C\ell_h e^{1/2} \qquad \text{and} \qquad K_{mv} = C\ell_v e^{1/2} \tag{3.16}$$

where $C = 0.1$.

$$K_h = \frac{K_m}{Pr_t} = K_m(1 + \frac{2\ell}{\Delta}) \tag{3.17}$$

In the 1,5 order TKE closure the isotropic and anisotropic (large aspect ratio) also differ in for the formulation of ℓ. For isotropic turbulence, and for an unstable or neutral atmosphere, the mixing length is :

$$\ell = \ell_h = \ell_v = \Delta = (\Delta x \Delta y \Delta z)^{1/3} \tag{3.18}$$

whereas for a stable stratification, the mixing length is : $\ell = min(\ell_s, \Delta)$, with ℓ_s defined after Moeng (1984):

$$\ell_s = 0.76 e^{1/2} (\frac{g}{\theta_0} \frac{\partial \widetilde{\theta}}{\partial z}) \tag{3.19}$$

In the case of anisotropic turbulence, the vertical and horizontal mixing length differ. In the case of a neutral or unstable stratification the mixing lengths are defined as:

$$\ell_h = \Delta_h \qquad \text{and} \qquad \ell_v = \Delta_v$$

Whereas for a stable atmosphere, we have ℓ_s:

$$\ell_h = min(\ell_s, \Delta_h) \qquad \text{and} \qquad \ell_v = min(\ell_s, \Delta_v)$$

Where Δ_h and Δ_v) are defined as in equation 3.9

In ARPS, an option for non-local mixing is available (called PBL parametrisation, Sun and Chang (1986)), but can only be applied to computations with resolution larger than 100m in the horizontal and in the vertical. In this case, the model does not behave as a LES model anymore and is consequently not discussed here.

In the following the two SGS models are tested. Sensitivity analysis is also performed on the SGS models empirical coefficients.

3.3 ARPS setup for the neutral atmosphere simulations

In the following numerical experiments, the model is set up as close as possible to the numerical experiment over real mountainous terrain, presented in Chapter 4, so that comparisons allow to investigate the influence of a complex terrain on the air flow. The main goal here is to test the mechanical turbulence in ARPS, this is the reason why a neutral atmosphere is applied in all the numerical experiments of this chapter.

The grid size was first set to $(nx, ny, nz) = (67,67,43)$, in order to have a grid similar to the one used in chapter 4. The horizontal resolution in x and y-directions is dx =25m, this leads to a length of the domain is $L_x = (nx - 3)dx = 1500m$. However to ensure that the eddies have enough time to develop and do not interact with themselves due to periodic boundary conditions, the numerical domain has been extended in the streamwise direction, so that L_x is of the order $O(6L_y)$. In the presented computations. The horizontal length of the numerical domain is set to $L_x = 6000m$. In the vertical direction, the grid levels are stretched using a tangent hyperbolic function : as a result, the mean vertical resolution is about 100 meters and the minimum resolution, near the ground, is about 3 meters. The vertical extend of the numerical domain is $L_z = 2600m$. A smaller vertical extent of the grid leads to reflection of numerical waves.

The set of equations is solved here with a fourth-order advection scheme in all directions for momentum and for scalar fields a fourth-order centred-in-space scheme is used. The time discretisation is treated using the time-splitting technique (Klemp and Wilhelmson, 1978): equation terms are split into sound waves and gravity waves. An explicit formulation is given for the terms responsible for the sound waves and are integrated with small time step, whereas other terms are evaluated using a larger time step. The pressure is explicitly formulated, and the Poisson equation, which diagnostically determines the pressure in anelastic systems has non-constant coefficients due to the grid stretching in the vertical direction. A second-order Leapfrog scheme is used to solved the time discretisation and an Asselin time filter (Asselin, 1972) is applied at every large time step. The tuning of the time filter coefficient is discussed in section 3.4. The Coriolis terms are turned off as the domain extent is small.

ARPS is used here in its LES configuration and the two turbulence closures described previously are tested. A fourth-order computational mixing, equivalent to a numerical hyper-viscosity, is applied in order to avoid high frequency motions that appear due to non-linear terms. This coefficient has been set to a minimum so that the computations are stable.

The top boundary is a free-slip rigid lid and the bottom boundary condition is a rough rigid wall with a roughness length of 2 centimetres. A logarithmic law is used by ARPS to compute the surface fluxes. The drag coefficient is computed through the friction velocity which is formulated using the Monin-Obukhov similarity theory

and the Richardson number as stability parameter (Businger et al., 1971; Buyn, 1990; Deardorff, 1972).

The lateral boundary conditions are periodic in order to consider the flow as infinite, and let enough time for turbulence to develop. It also allows direct comparisons to other numerical models results. In the case of periodic boundary conditions, the pressure field was detrended using ARPS pressure detrending option, in order to avoid oscillations due to boundary effects which propagate through the domain. This pressure detrending option (Xue et al., 1995, chap 6.3) removes the domain-wide pressure drift or trend by setting the domain-averaged Exner function to zero at every time step. The detrending of the pressure field does not change the solution for the current neutral atmosphere as the pressure perturbation interfere only with buoyancy terms (Chow, 2004; Xue et al., 1995).

Fixed boundary conditions for the inflow (west boundary) have been tested, with rigid-wall on the north and south boundary, and zero-gradient on the outflow boundary (east boundary). This type of boundary condition was chosen for comparison with the nesting technique as presented in chapter 4. Numerical experiments have been run with addition of a random sine function-based perturbation on the fixed boundary conditions. However this configuration did not permit to compute smaller motions, so the results are not shown here.

For all the experiments presented in this chapter, the model is initialised with a neutral stratification and an initial logarithmic wind profile unidirectional for the streamwise velocity component. Also at each grid point a small initial random perturbation of small amplitude ($[-1, +1]$) is introduced in addition to the initial profile (Figure 3.1), on the three velocity components, to create a velocity gradient. ARPS does not produce any perturbation by itself if the terrain is flat. This small perturbation is constructed so that the xy-plane average equals zero. To record realistic turbulence field, the flow is allowed to developed until these perturbations are forgotten. This initialisation to trigger the mechanical turbulence fields has been implemented in ARPS specially for the numerical experiments presented here.

The model is run for 30 hours in order to get a stationary flow and have enough data points to construct the spectra. Moreover this period covers the duration of the computations over the real topography which last one day.

It is observed that the flow develops during the first 7200s seconds before being completely turbulent. Time series are collected at several z-levels : z=3,5,10 and

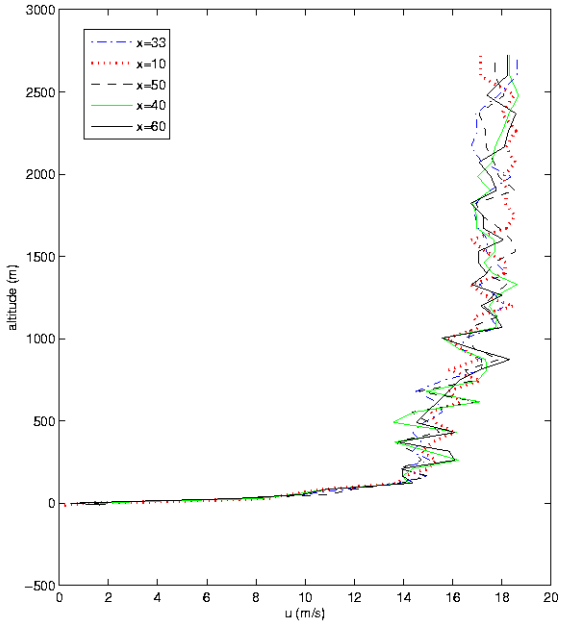

Figure 3.1: Initial streamwise velocity component profiles at several x-positions along y=33. Small amplitude perturbations are added to the logarithmic profile

15 (about 3m, 50m, 345m, 1300m respectively above the ground), and over a fixed central plan, along y=33. The flow is assumed to be homogeneous in horizontal, and turbulence data can be averaged over this plan. Data have been recorded when the flow was stationary, and each time series contains 10 to 20 hours of data for the spectral analysis of the turbulence.

The code is parallelised using the MPI interface. The following simulations were run on a 64 processors cluster at the WSL (Swiss Federal Institute for Forest, Snow and Landscape Research). The nodes are AMD opteron 270 processors at 2GHz. Details on computing performances can be found in Appendix A.

3.4 Results and sensitivity analysis

The averaging period for statistics is chosen when the statistics/flow variables remains roughly stationary. This is observed also in figures showing times series of velocity fluctuations or friction velocity.

3.4.1 Coefficient for the Asselin time filter

In ARPS uses a centred in time (Leapfrog) numerical scheme for advection. A time filter is consequently required to prevent the three time steps from diverging. Consequently the Asselin time filter is applied at each large time step. The Asselin time filter is defined for any variable ψ as (Asselin, 1972):

$$\psi^t = \psi^t + C_a(\psi^{t+\Delta t} - 2\psi^t + \psi^{t-\Delta t}) \tag{3.20}$$

The default value in ARPS is $C_a = 0.05$. If C_a is set to zero, the filter is turned off. These two extreme values constitute the range for the following sensitivity analysis. The resulting time series for the streamwise velocity component u are, at level $z = 10$ (about 300m above ground), are presented in Figure 3.2.

These time series are interesting as they show that for a too high Asselin coefficient ($C_a = 0.05$), all smaller scales are filtered. Moreover the motions tend to be periodic, with a time period of about 72s, but does not correspond to the advection time for a structure to cross the domain (at $z = 10$, $\bar{u} \approx 16m/s$) Without the Asselin filter, the small scales fluctuations are present, however there is a numerical noise that appear and create this blurry curve for the non-filtered signal (see Figure 3.2) This forms a clearly identifiable peak at a frequency of 4Hz when looking at the spectra.

The correct value for the Asselin filter should be able to remove this noise without filtering the physical small scale motion that are present. The sensitivity analysis suggested to fix this coefficient to 0.01. The following experiments are consequently performed with an Asselin coefficient of 0.01. Now that the filter coefficient is tuned, it is possible to concentrate on the SGS models. Indeed the filter is independent and common to both SGS model.

3.4.2 Smagorinsky closure

In ARPS, the default value for the Smagorinsky coefficient, as presented in equation 3.4, is $C_k = 0.21$. This coefficient measures the numerical resolution provided for a cut-off length scale for eddies that are parametrised. Mason and Callen (1986) explain that a value of 0.2 is optimum and greater values provide unnecessary resolution but smaller values carry finite differences errors. Lilly (1967) indicates that $C_k = 0.23$ is the value implied by the energy on the mesh scale corresponding to an inertial subrange. The form of the inertial sub-range cascade is in agreement with

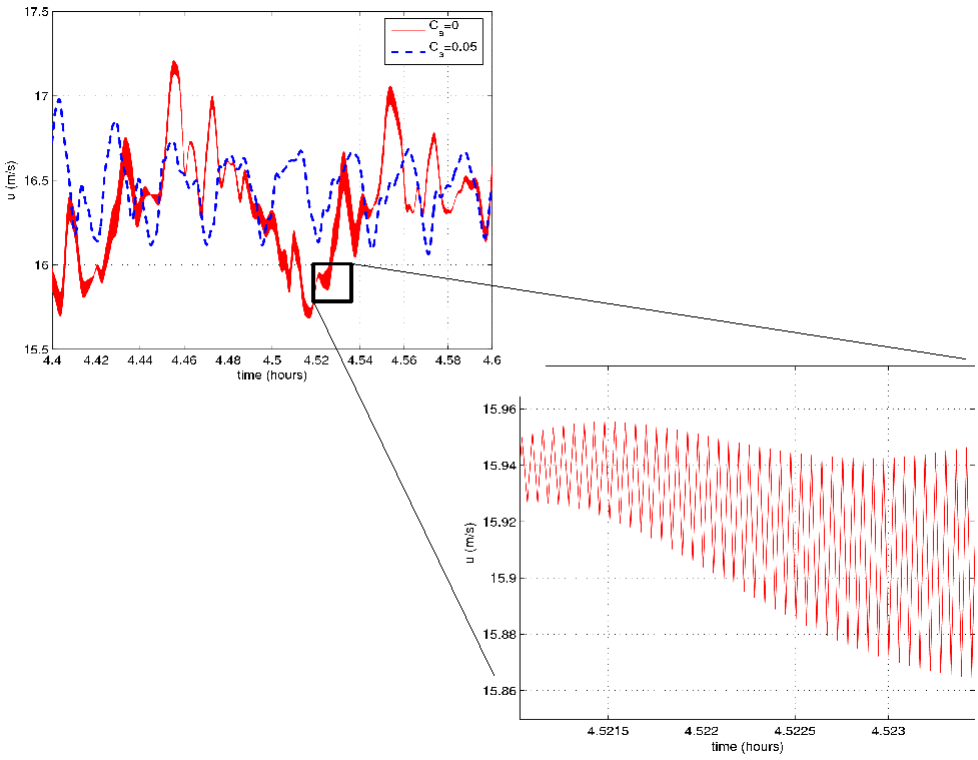

Figure 3.2: Time series of the streamwise velocity at z=10 (about 300m above the surface). Comparison of results with a Asselin filter coefficient of 0.05 (dashed line), and without time filter (solid line). The zoom (right) on the time series without Asselin time filter show high frequency numerical noise.

the requirement that finite differences should have only a small amount of energy on the scale of the grid.

ARPS default value is in agreement with the values suggested by the PBL flow experiment of Lilly (1967); Mason and Callen (1986). However, with a grid spacing of 25m, this value of C_k filters the small scales as can be seen in the time series of the resolved velocity presented in Figure 3.3. Consequently, the Smagorinsky coefficient has to be set properly for the current model configuration.

Several values of the Smagorinsky coefficient have been tested, starting with the extremely low value of $C_k = 0.05$. With this value, the resolved streamwise velocity tends to oscillate at the first level above the ground (i.e. 3 meters above the ground).

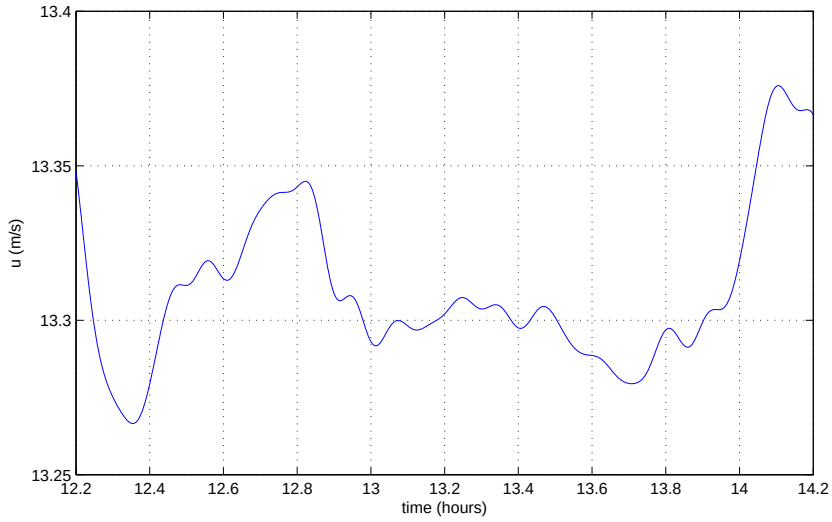

Figure 3.3: Zoom on the time series of the streamwise velocity u at level z=5 (about 68m above the surface), obtained from the numerical experiment with ARPS default value $C_k = 0.21$.

This behaviour disappears at the fifth level above the surface (corresponding to about 68 meters above the ground). Moreover the time series present periodic patterns, at all levels, with a period of $f \approx 1min$, as can be seen in Figure 3.4, presented for level 5 at about 68m above the ground. This correspond to a distance of about 6.1km and indicates that some eddy are recirculating through the domain producing coherent structures (see Figure 3.5).

With a value of $C_k = 0.12$, the oscillations near the surface disappear and the periodic features seldom appears, as shown in the time series of the streamwise velocity at level 5 (see Figure 3.6) Indeed the coherent structures are not observed frequently, in the cross section in the xy-plan (See Figure 3.7)

Higher values of C_k do not improve these results, and were more diffusive near the surface. Consequently the Smagorinsky coefficient is set to $C_k = 0.12$. ARPS was originally designed for storm scale (i.e. about 3km) simulations, hence the original value of the subgrid scale parametrisation included also larger unresolved flow features than in the current study. This could explain the quite large difference between ARPS default value and the one found here. In the following, the turbulence statistics are analysed from computations results using this value. For comparisons

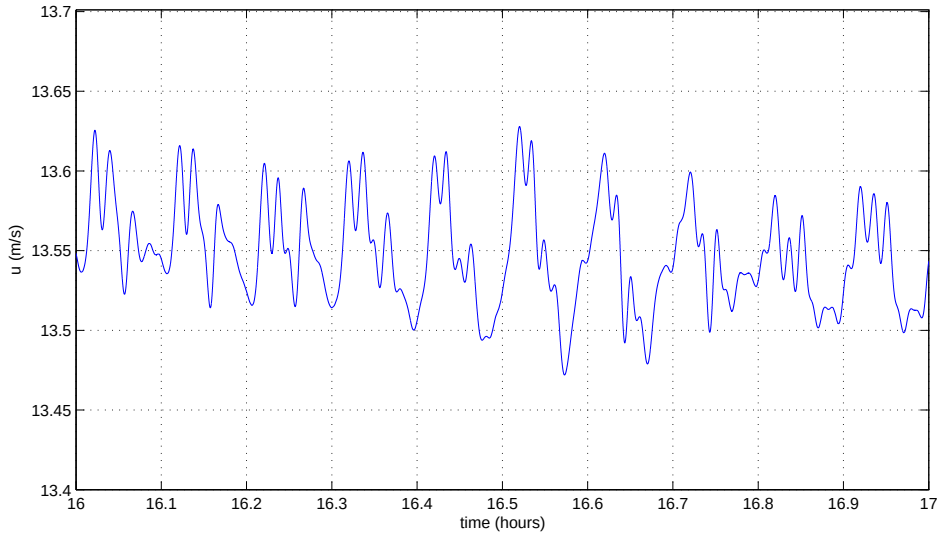

Figure 3.4: Zoom on the time series of the streamwise velocity at level z=5 (about 68m above the surface), obtained from the numerical experiment with ARPS default value $C_k = 0.05$. Periodic features can be observed

with the results over real topography (see Chapter 4), where space average are not possible, the spectra are computed in the frequency domain. according to the Taylor hypothesis, the spectra in the wave or frequency domains should be identical.

The velocity spectra of the resolved streamwise velocity (figure 3.8) indicate that above a height of about 300m (level z=10), the eddies are resolved up to a size of about 54 m ($f_c \approx 5.10^{-2} Hz$), which correspond to roughly the filter size in equation 3.6. At lower levels, like at level 5 (68m), the transition occurs at $f_c \approx 9.10^{-2} Hz$. Eddies smaller than about 50 m are not explicitly resolved. Near the surface the flow is not well resolved although the vertical grid spacing in this region is refined using the stretching method.

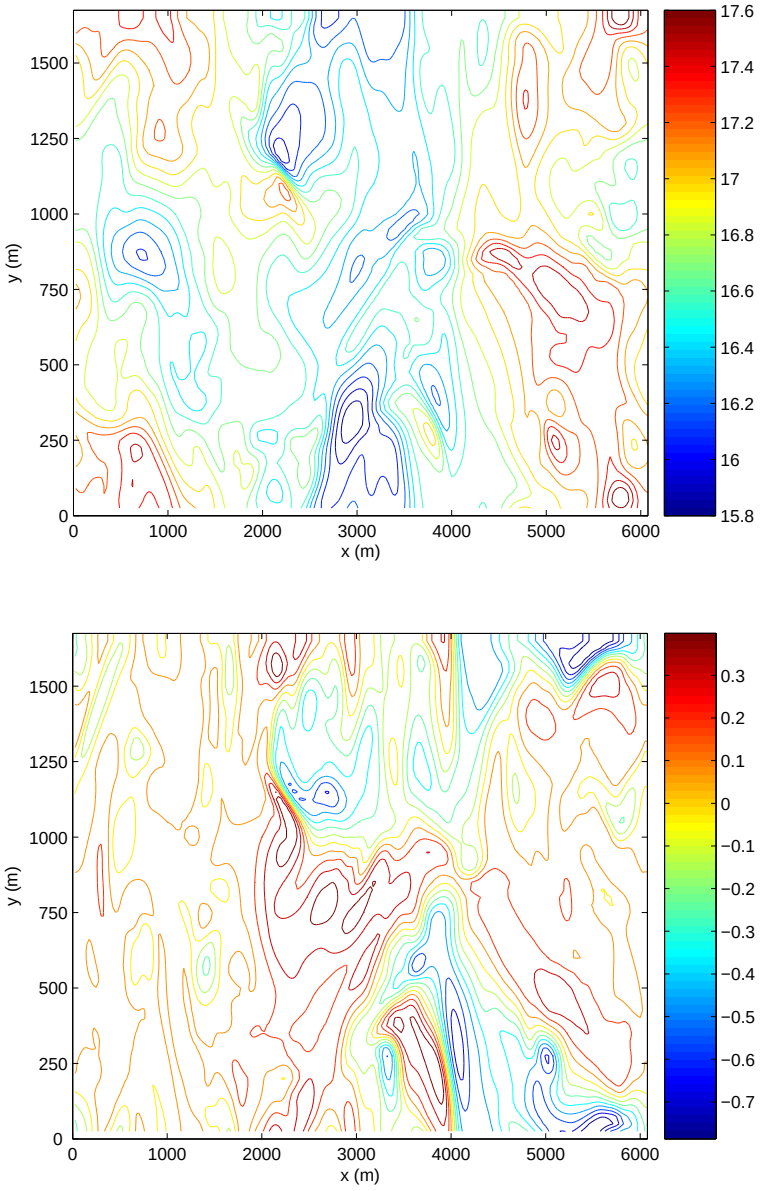

Figure 3.5: Contours of the streamwise velocity u (left) and vertical velocity w (Right), on a horizontal cross-section at level z=5 (about 68m above the surface). This results are obtained from the numerical experiment with $C_k = 0.05$, at time t=16h.

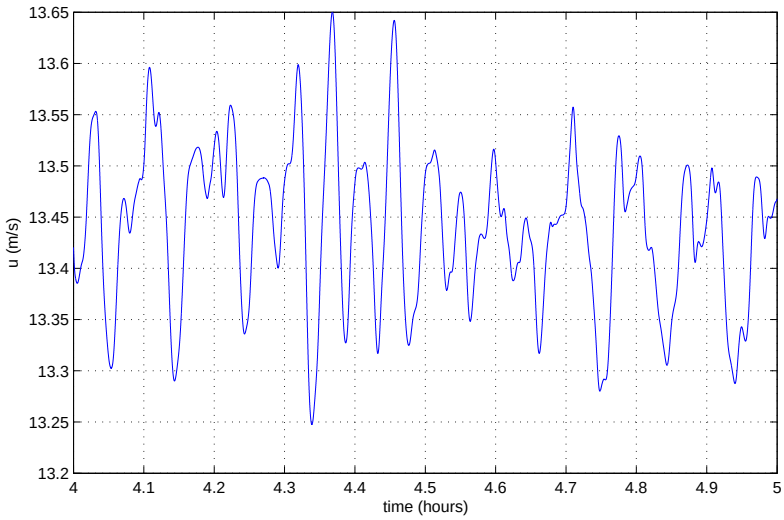

Figure 3.6: Zoom on the time series of the streamwise velocity at level z=5 (about 68m above the surface), obtained from the numerical experiment with ARPS default value $C_k = 0.12$.

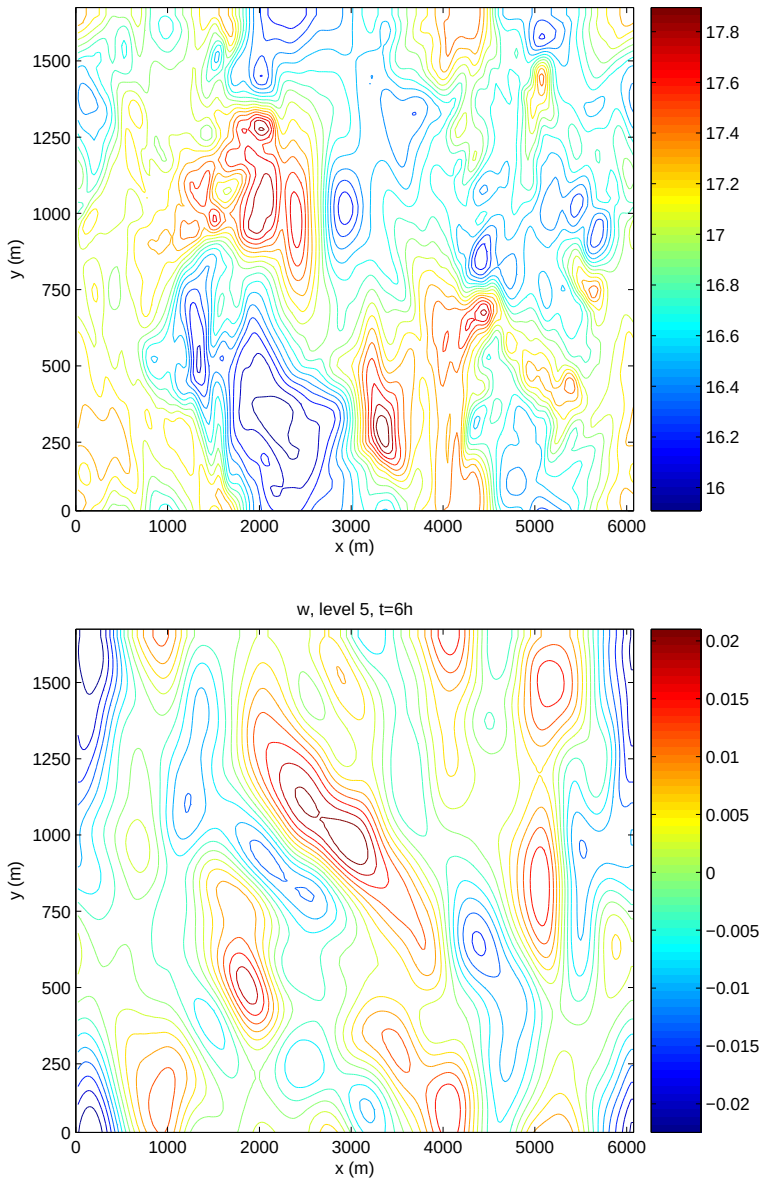

Figure 3.7: Contours of the streamwise velocity u (left) and vertical velocity w (Right), on a horizontal cross-section at level z=5 (about 68m above the surface). This results are obtained from the numerical experiment with $C_k = 0.12$, at time t=6h.

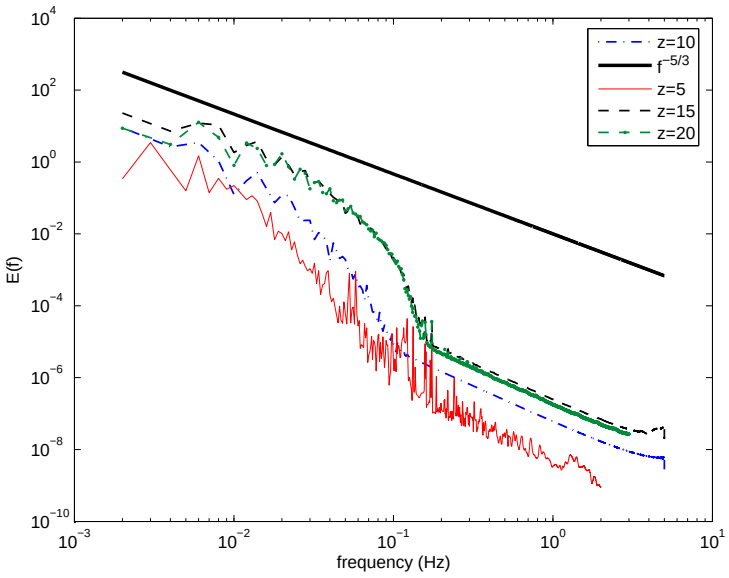

Figure 3.8: Streamwise velocity spectra at several heights : z= 10 (300m), z=5 (68m), z=15 (900m), z=20 (2100m) . The spectra are computed from the numerical experiment outputs with the Smagorinsky closure using $C_k = 0.12$.

3.4.3 Comparisons with the 1.5 order TKE closure

The Deardorff formulation for the 1.5 order TKE closure allows the diffusion coefficient to be changed for the first levels. Indeed the diffusion term in the prognostic TKE equation takes into account the grid scale via a mixing length (see section 3.2.2), thus the vertical refinement of the grid is taken into account in the dissipation terms in the TKE prognostic equation. The diffusion coefficient for TKE, C_ε, is expressed as in equation 3.13.

A similar procedure to the one applied previously to find the Smagorinsky coefficient has been applied in order to find the diffusion coefficient for the TKE closure. This coefficient has been set to the following values :

$$C_\varepsilon = \begin{cases} 3.9 & \text{up to the first level above the ground,} \\ 0.9 & \text{otherwise.} \end{cases} \tag{3.21}$$

The results obtained with these values are compared with the Smagorinsky closure results. The streamwise velocity spectra indicate the same behaviour as with the Smagorinsky closure, i.e the flow is underresolved for levels that are below about 400m. Although slight discrepancies appear : in the case of the 1.5 order TKE closure, there is already more energy starting at level 10, but the spectra obtained for lower levels show that smaller scales are filtered near the surface.

The TKE spectrum at level 10 (Figure 3.10), where the flow starts to be better resolved, gives a cut frequency $f_c = 10^{-1} Hz$ for the Smagorinsky closure. This is however more difficult to interpret in terms of length scale when considering the TKE spectrum, although it permits a more direct comparison with the 1.5 order TKE closure experiments (figure 3.11). The results obtained with the 1.5 order TKE closure give a similar frequency. In addition, it is interesting to observe that all the energy comes from the resolved scales, indicating that the choice of the grid resolution is consequently more important than the closure type over homogeneous flat terrain.

In neutral conditions, the velocity variances decrease with the height (Mason and Thomson, 1987), from large values at the surface, over a depth of about 2 km. In Figure 3.12, the variance profiles for both SGS model, Smagorinsky and 1.5 order TKE are presented. In both cases, the variance starts from zero at the surface and reaches its maximum at about 300m above the surface and decrease up

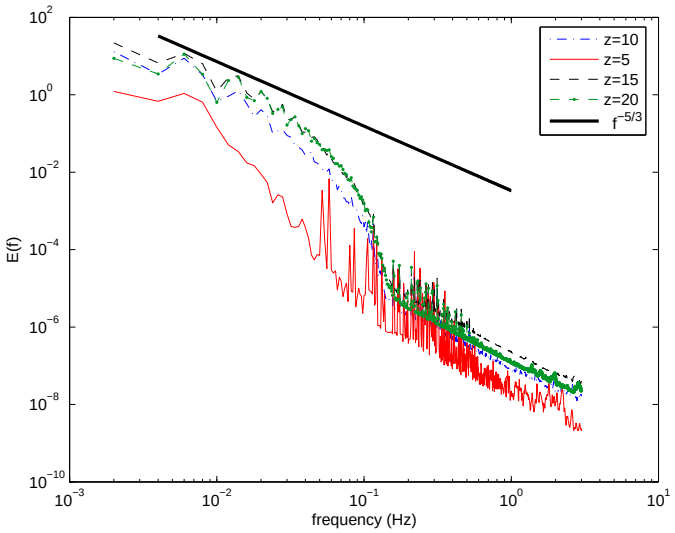

Figure 3.9: Streamwise velocity spectra at several heights : z= 10 (300m), z=5 (68m), z=15 (900m), z=20 (2100m) . The spectra are computed from the numerical experiment outputs with the 1.5 order TKE closure.

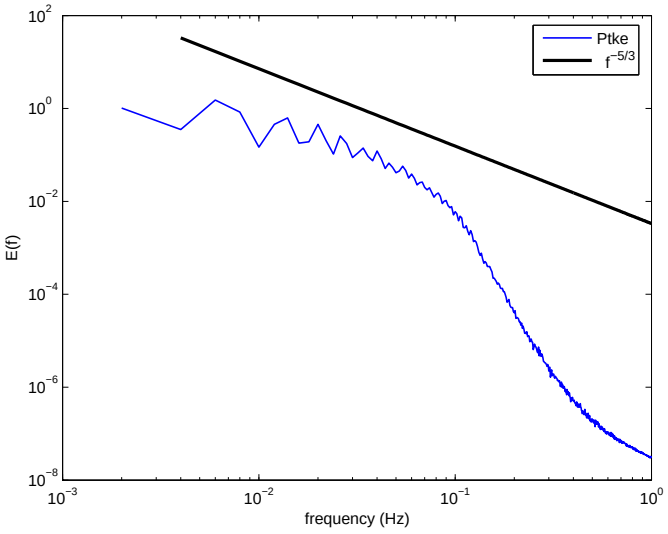

Figure 3.10: TKE spectra at level z=10 (300m above the surface). Results obtained from the numerical experiment with the Smagorinsky closure $C_k = 0.12$.

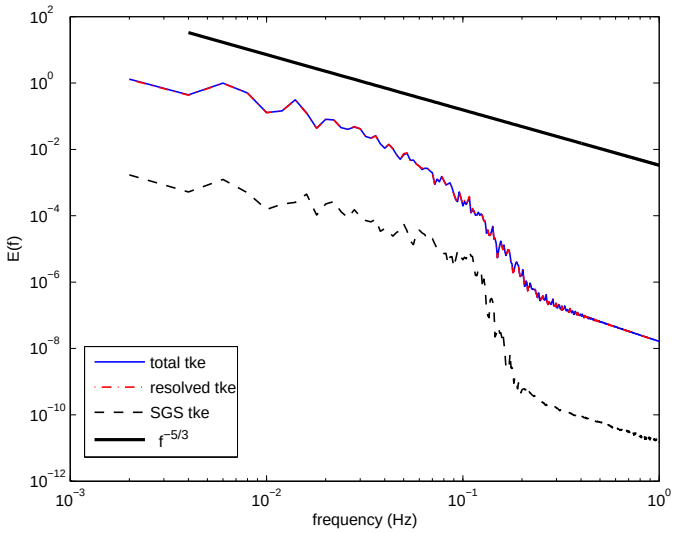

Figure 3.11: TKE spectra at level z=10 (300m above the surface). Results obtained from the numerical experiment with 1.5 order TKE closure. The total and resolved TKE spectra are represented in solid and dash-dot lines and are identical.

to the middle of the domain. The depth over which the flow is turbulent concentrate between about 300 m to 1400m. Consequently the depth scale is here much smaller as the one suggested by Mason and Thomson (1987), and the flow tends to be more laminar near the ground. It confirms the fact that near the ground, the small eddies of the flow are not well resolved.

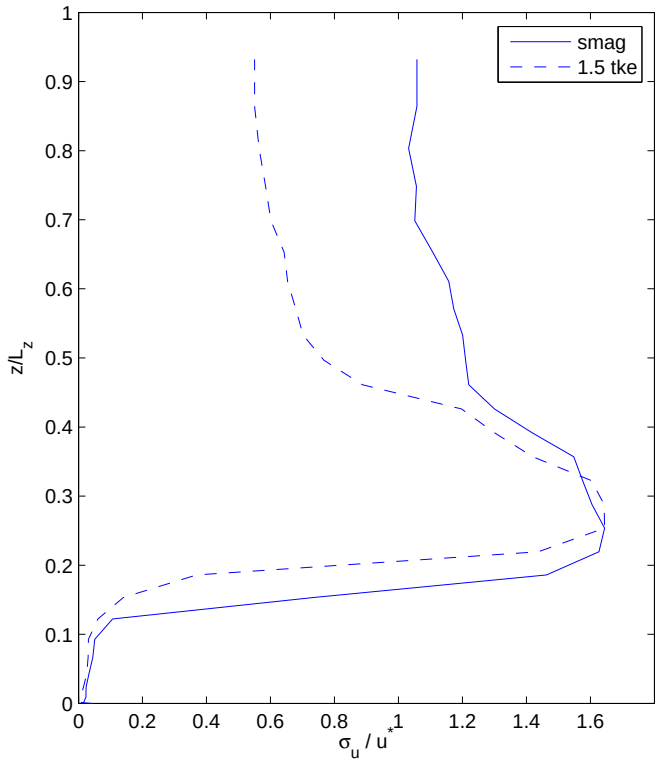

Figure 3.12: Variance profiles of the u-velocity, obtained from the numerical experiment with the Smagorinsky closure using $C_k = 0.12$ (solid line) and with the 1.5 order TKE C_ε (dashed line).

3.5 Conclusions

Airflow computations over flat terrain and in a neutral atmosphere have been conducted with ARPS to test the ARPS turbulence models and fix some parameters values, namely the Smagorinsky coefficient for the Smagorinsky closure, the diffusion coefficient for the 1.5 order TKE turbulence model, and the Asselin time filter parameter. The Asselin time filter coefficient was set to 0.01 a smaller value than the default ARPS value. This was necessary to avoid filtering small time scale fluctuations. This value remains however high enough to prevent the numerical solution from diverging.

The numerical experiments presented here also indicate that over flat terrain ARPS does not produce any turbulent features when the perturbations are not triggered during the initialisation or by the boundary conditions. This has been achieved here by the introduction of small perturbations on the initial mean wind profile.

The comparison between the Smagorinsky and the 1.5 order TKE closures show that both SGS models gives similar results over homogeneous, flat terrain. The flow is poorly resolved near the surface in both cases and the turbulence concentrates in a layer extending between about 300m and 1400m above the ground. Further work could include testing varying Smagorinsky coefficients over the numerical domain height, if one is interested in using this turbulence model. The addition of an enhanced near-wall model has also proved to compensate the poor resolution in this region (Senocak et al., 2007).

The settings obtained from these numerical experiments will be used for evaluation of computations over a real mountainous topography, presented later in Chapter 4. In the computations over complex terrain, the 1.5 order TKE closure is preferred to the Smagorinsky closure as it includes a transport equation for the TKE and hence allows the TKE produced at one location to be dissipated further. It is consequently more suitable to simulate flow over non-homogeneous terrain.

The results of the experiment with the 1.5 order TKE SGS model, presented in the last section, will be used to produce boundary conditions files for computations of the airflow over an Alpine ridge as explained in Chapter 4. The results obtained here form a basis for comparison with the results obtained over real topography (Chapter 4) and hence to understand the influence of the topography on the distribution of energy between the different scales.

Chapter 4

Simulations of the airflow over Gaudergrat during the Gaudergrat Experiment

4.1 Introduction

Snow transported by wind is an important factor for avalanche formation as well as in the ecology and hydrology of mountainous environments. The topographic modifications of airflow by mountain landscapes may result in snow erosion and accumulation zones (Lehning et al., 2008, submitted). Proper modeling of the windfield is fundamental for prediction of snow redistribution.

The understanding of flow features in steep and complex mountainous environments still remains limited despite an increasing number of recent studies. The main physical processes of flows over gentle hills can be described using linear analysis (Hunt et al., 1988a,b), whereas this is not possible for steep topography.

In the 70s and 80s, experimental studies have concentrated on gentle hills surrounded by almost flat terrain. Brent Knoll (Mason and Sykes, 1979), Black Mountain (Bradley 1980), Blashaval (Mason and King 1985), Askervein Hill (Taylor and Teunissen, 1987) are examples. These studies highlight some differences in the airflow over hill compared to the airflow over flat terrain. However these experimental studies did not always agree in finding an universal behaviour for turbulence characteristics over complex topography.

Antoniou et al. (1992) studied the modification of turbulence structure caused

by topographic effects and compared to the results obtained for turbulence over homogeneous flat terrain in Kansas (Kaimal et al., 1972). The horizontal velocity components spectra contain more energy at low frequencies and are sensitive to wind direction. Based on experimental data, Founda et al. (1997) found that the asymmetry of the upwind terrain clearly appears in velocity variances profiles and in spectra. Later, Van Gorsel et al. (2003) studied turbulence over steep forested slopes, focusing on the influence of the canopy on flow characteristics. Their observations indicate that in the canopy, a sharp attenuation of the turbulence is observed.

In parallel to experimental studies, numerical models have been used to simulate air flows over complex terrains. Flow separation and recirculation in the boundary layer over 2D and 3D topographies and real terrain have been successfully simulated by Kim and Patel (2000), using Reynolds Averaged Navier-Stokes (RANS) equations combined with the single equation model ($\epsilon - \ell$) or two equations model ($k - \epsilon$) for turbulence parametrisation.

When the spatial and temporal resolution are alike and sufficiently fine, RANS and Large Eddy Simulations (LES) gave similar results (Hug et al., submitted) for mean flow features. The advantage of LES in simulating turbulent flow however is that up to the filter size (linked to the grid size in ARPS), the turbulence can be explicitly resolved.

The grid resolution has an obvious influence on the results but other parameters are also important. Simulations using MM5 model of the Föhn wind in the Rhein Valley (Zängl et al., 2004) and of in the Wipp Valley (Gohm et al., 2004) showed discrepancies in timing of events although most of the features were correctly reproduced. Zängl et al. (2004), found that results are also sensitive to parameter such as the numerical mixing, which was even more important than a fine grid resolution.

The data collected during Riviera-MAP project in 1999 described mean and turbulent structures of airflow in the steep Riviera valley (Rotach et al., 2004). de Wekker et al. (2005) studied the performance of the mesoscale model RAMS to reproduce the convective boundary layer in the Riviera valley and concluded that topographic shading was important. Topographic shading has been implemented in ARPS (Colette et al., 2003) along with detailed soil properties. As a result, convective air flow in the Riviera valley could be better reproduced (Chow et al., 2006; Weigel et al., 2006). The investigations of Turbulent Kinetic Energy (TKE) budget in the Riviera Valley (Weigel et al., 2007) indicated that ARPS could reproduce the correct diurnal trends for all terms of the TKE budget. However the largest part of

TKE was provided by the Subgrid Scale model, although using an LES configuration.

SGS dynamic models for LES can reproduce more accurate turbulence statistics especially in the surface layer (Bou-Zeid et al., 2005; Porté-Agel et al., 2000). However their application requires periodic boundary conditions that often limits application to idealised ABL computations. The nesting technique on the other hand allows LES with non-periodic lateral boundary conditions (Moeng et al., 2007; Sullivan et al., 1996). These nested LES simulations require modifications on the Subgrid Scale (SGS) model (Moeng et al., 2007).

Wind field simulations over the Gaudergrat ridge using the ARPS model, Submeso version (Anquetin et al., 1998; Xue et al., 2000, 2001) have been conducted by N. Raderschall (Raderschall et al., 2008, submitted), with a fine resolution of 25 meters. Well mixed boundary layer and strong wind conditions were applied, and the mean flow features could be well reproduced. However the model was initialised with a single artificial sounding and periodic boundary conditions were applied. With this homogeneous atmosphere initialisation method, the runs are highly sensitive to initial and boundary conditions and become quickly unstable. Another method for the initialisation of ARPS simulations over the Gaudergrat Ridge was proposed by G. Spreitzhofer (Spreitzhofer and Raderschall, 2004). A sounding is constructed based on the downscaling of four grid points of the MeteoSwiss Alpine Model, aLMo, located around the ARPS numerical domain. Although this initialisation leads to a more realistic atmosphere, it does not solve the boundary conditions issue. As a consequence of the interpolation, it is only applicable to a small domain especially in the mountainous terrain where the atmospheric parameters variability is high.

In the present study, ARPS is used in a one-way nesting configuration: aLMo outputs are interpolated on the ARPS coarsest domain, to provide initial and boundary conditions forcing. Then ARPS is run using four nested domains to bridge spatial resolutions from 7km (aLMo-grid size) to 25 m, the finest resolution. With such a fine resolution it is expected that the largest part of the flow energy is explicitly resolved. The present windfield computations are prepared for snow transport applications, however they could also drive pollution or fire smoke transport or other particles transport models.

The field data were recorded during the Gaudergrat Experiment (Gaudex) which took place during the summer 2003 at the Gaudergrat ridge, located near Davos, Switzerland. This large dataset is ideal for understanding the flow features

of the Gaudergrat (Lewis et al., 2007) as well as to check the modeling results.

In this chapter, airflow computations over the Gaudergrat ridge are presented for periods with rather synoptic (strong winds) driven southwesterly to northwesterly flows. These situations are the most comparable with observations during snowdrift events at the Gaudergrat location. The objective is to simulate accurate windfields and Turbulent Kinetic Energy (TKE) patterns over complex mountainous terrain during days dominated by advection using ARPS. The effect of the nesting technique on the qualitative mean flow features will be compared to the windfiled computations run using a homogeneous initialisation and periodic boundary conditions as computed by Hug et al. (submitted) and Raderschall et al. (2008, submitted). In addition, a quantitative comparison with the field data is presented. The performance of the model in representing TKE features are compared to the observations. These results reveals that an extra implementation of perturbations generation is required in addition to the nesting time dependent boundary condition. Consequently a method for artificial turbulence generation is proposed.

4.2 The Gaudex field campaign

4.2.1 Experimental site description

The experimental data have been collected during the Gaudergrat Experiment (Gaudex) which is described in Chapter 2.

The north-south orientation of the ridge is roughly perpendicular to the prevailing winds blowing from west to north west (Gauer, 2001). The steep slopes reach angles up to 55 degrees but the Swisstopo 25 meters resolution dataset presents slopes up to 45 degrees (See Annexe B). The ridge is also surrounded by other mountains, which makes the topography even more complex and challenging for numerical models.

In addition to the turbulence towers described in Chapter 2, other measurements stations are used for comparisons with the model results.

In the following the measurements sites are called by their number. The location and number of the measurement sites are shown in Chapter 2 in Figure 2.3. A detailed description of the Gaudex can be found in (Lewis, 2006, chap. 3 and annexes)

4.2.2 Flow characteristics observed during the Gaudex

The extensive Gaudex surface observations permit to determine the flow characteristics. As presented in Mobbs et al. (2005), Lewis (2006) and Lewis et al. (2007) three characteristic flow features could be identified on the Gaudergrat Ridge based on wind speed and direction comparisons:

- flow separation from the ridge crest with a horizontal axis eddy in the lee and re-attachment near the foot of the slope
- flow separation at the north end of the ridge with a stable vertical axis eddy
- flow parallel to the ridge at lower altitudes, on both sides and a pronounced cross-ridge flow independent of the inflow conditions

These flow features could be qualitatively reproduced using ARPS and a commercial fluid dynamic code CFX (Hug et al., submitted), using theoretical soundings for a horizontally homogeneous initial state (i.e. the same conditions at every grid points). However, this method works only for short computing periods only, and CFX was able to reproduce the flow separation only in the case of a stable atmosphere. In addition to the prevailing west to north-west winds already observed at the Gaudergrat ridge in winter (Gauer, 2001) during snowdrift events, south-west winds were often present during Gaudex 2003. Airflow differences between winter and summer can be explained by thermal effects (Hug et al., submitted).

4.3 Meteorological situation and flow characteristics on August 11 and 18, 2003

In order to analyse situations as close as possible to winter, this study concentrates on two strong wind days during the period of observations with winds from south-west to north-west. These wind conditions are most frequently encountered during snowdrift events at the Gaudergrat. However the thermal effects, although small cannot be neglected during these two summer days.

The two selected days were fair-weather days. The surface isobaric map of the Met Office (Figure 4.1, upper graphic) shows however on the 11th of August that a week low pressure centre (1013hPa) was crossing Switzerland. On August 18, the pressure distribution at the surface showed a synoptic west wind influence.

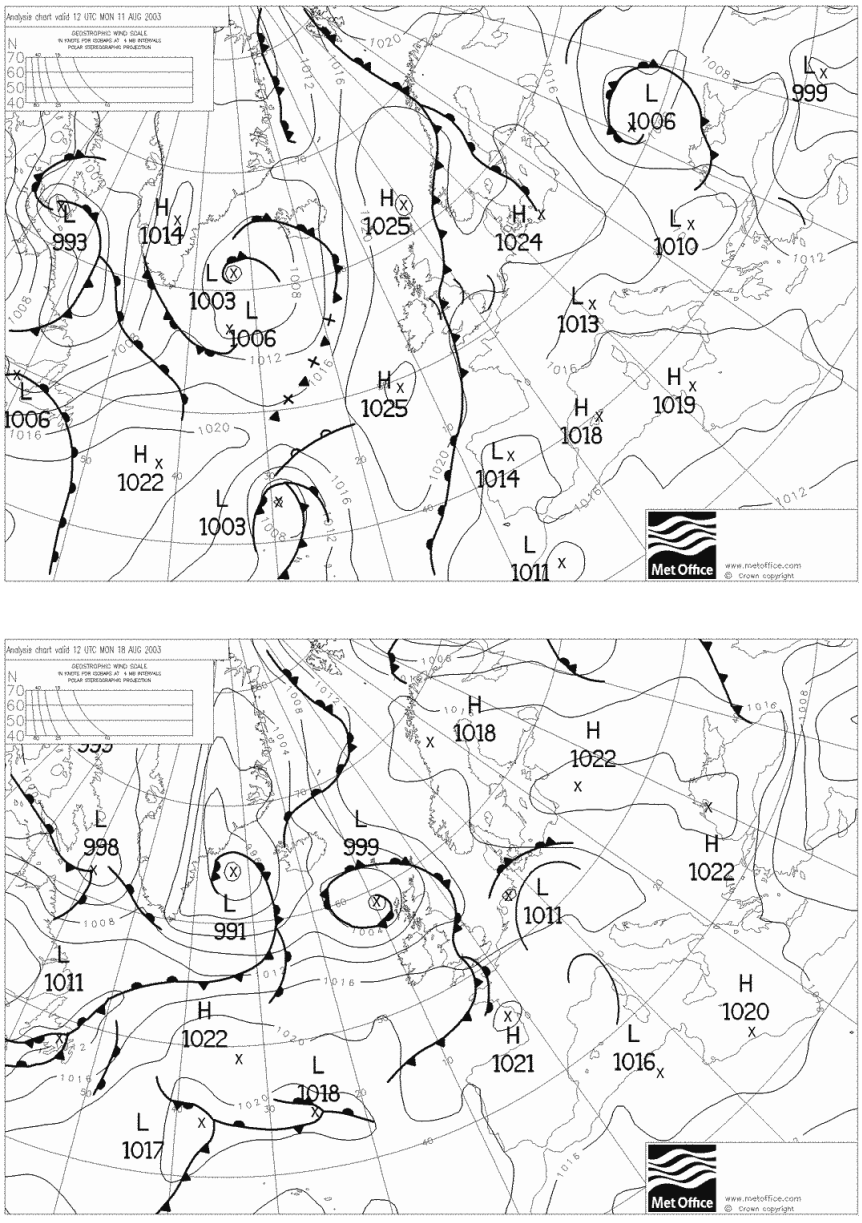

Figure 4.1: Surface isobaric maps from the Met Office at 12:00 UTC on August 11 (above) and August 18 (below), 2003

A more regional overview of the flow conditions is given by another permanent weather station: the Weissfluhjoch, located 1 kilometer on the south-east of the Gaudergrat, at the altitude of 2693m. The measurements at Weissflujoch show a

north-west flow on the 11th of August before 6:00 and in the afternoon. The wind blows from north-east between 6:00 and 12:00, and from south after 18:00. On the 18th of August, the flow is a steady southerly wind until 6:00, before turning briefly to north and fluctuating between south and west (Figure 4.2) during the rest of the day due to synoptic forcing. The wind speeds are quite constant and range between 2 and 5m/s on August 11 with a peak after 18:00 at 7m/s. On August 18, wind speed is less steady and varies between 1 and 6 m/s.

The local situation, on the upwind side of the ridge, is described by measurements at site 27 (Figure 4.3) where the horizontal windspeed and direction are measured at 5m above the ground. On August 11, wind conditions are under the influence of thermal effects but the situation is still interesting for its northwesterly afternoon flow. As typically observed during Gaudex (Lewis, 2006) at night a southerly wind is blowing. Then during sun rise, the wind direction turns rapidly to east, then north and changes to south-west until midday before blowing from north-west in the afternoon. The wind speed also shows a clear cycle along the day, with a stronger variability due to thermal effects. The wind speed is 3m/s in average between 7:00 and 17:00, whereas it is only about 1m/s during the night. On August 18, the wind direction is south to south-west before turning to the east between 15:00 UTC and 18:00 UTC. Two accelerations are noticeable at 8:30 UTC and 14:00 UTC, the first one corresponding to the start of an increased synoptic forcing at the Weissfluhjoch the second one corresponding to a change in the wind direction.

Concerning the stratification, no sounding are available on these days. An estimation of the atmosphere stability close to the surface is given by the surface heat fluxes as presented in Figures 4.4 and 4.5. The surface heat fluxes are computed using the ultrasonics temperature measurements at 7.5 meters above the surface from sites 31 (East slope), 32 (Crest) and 33 (West slope). The influence of the sun appears clearly on August 11 (Figure 4.4). As soon as the sun light the ground surface, the air close to the ground surface is warmed up and the atmosphere near the ground becomes unstable. Indeed This phenomenon starts earlier on the East slope. On August 18, as the wind is stronger, the effect of the sun is not so pronounced due to stronger wind. However during the day, the atmosphere become unstable. The surface heat fluxes for both days show that the influence of thermal flow is difficult to avoid during fair weather summer days.

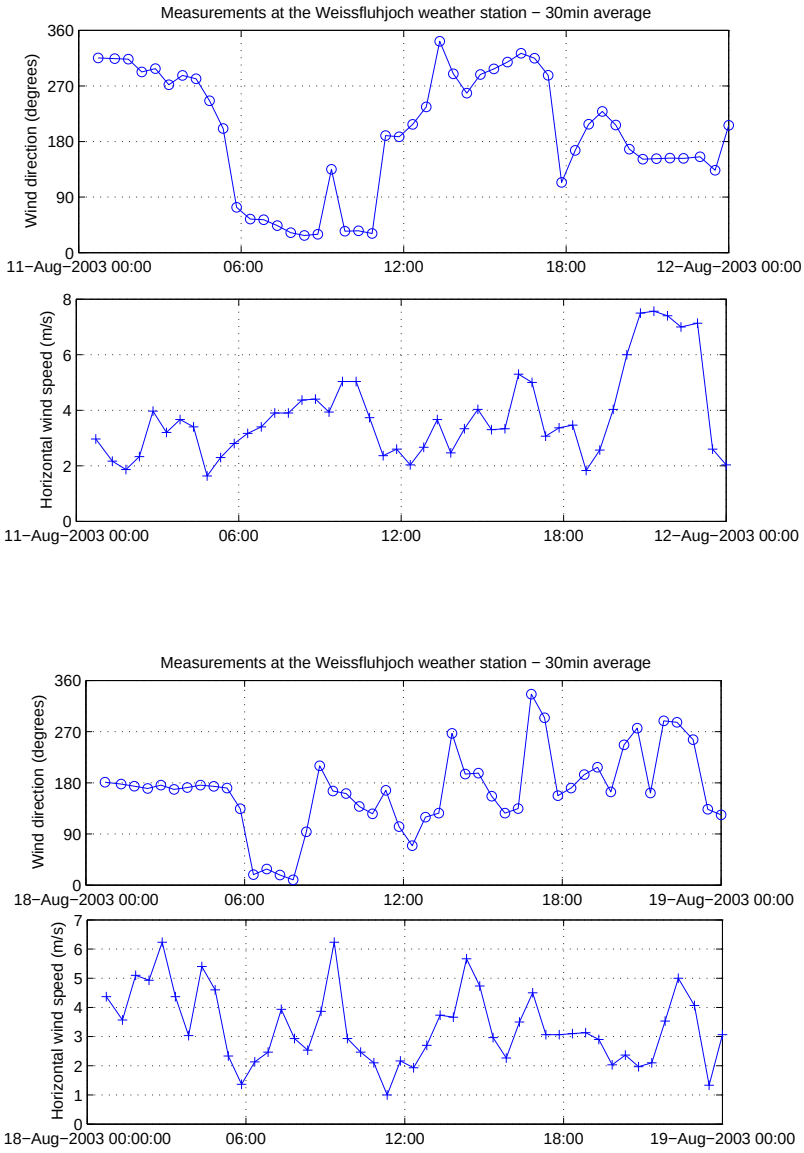

Figure 4.2: Wind direction and speed measurements at the Weissfluhjoch on August 11 (above) and August 18 (below), 2003 (data are averaged over 30 minutes, time is UTC)

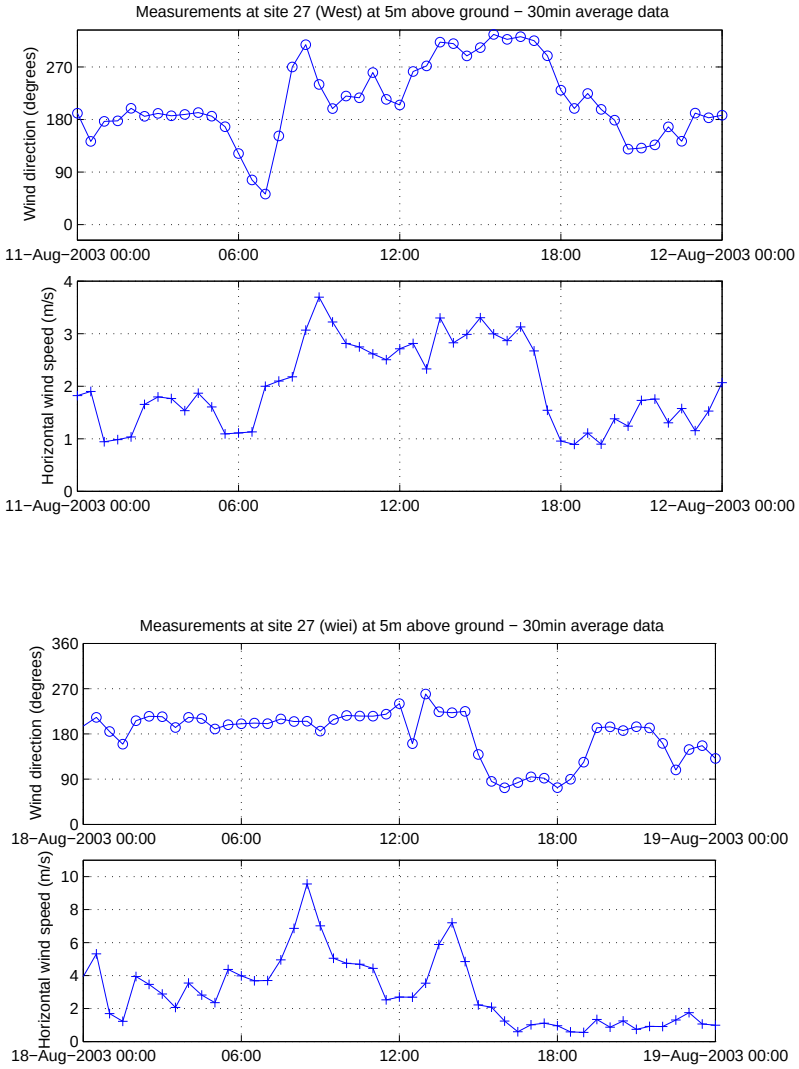

Figure 4.3: Wind direction and speed measurements at site 27, at 5m above the ground, on August 11 (above) and August 18 (below), 2003 (data are averaged over 30 minutes, time is UTC)

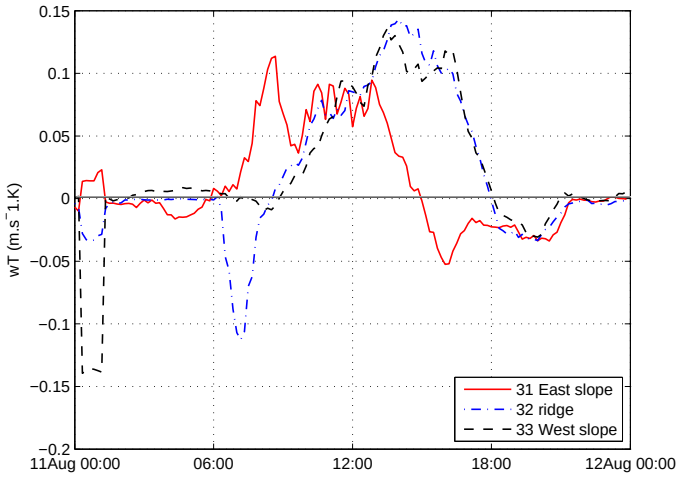

Figure 4.4: Surface heat fluxes at sites 31, 32, 33, on August 11 (Time is UTC)

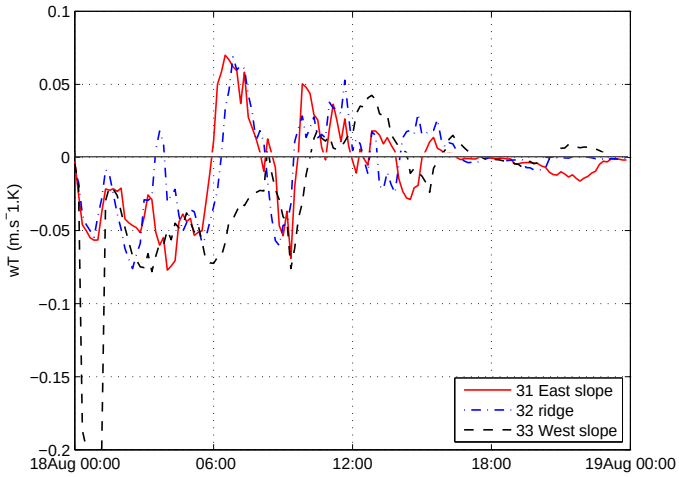

Figure 4.5: Surface heat fluxes at sites 31, 32, 33, on August 18 (Time is UTC)

4.4 Numerical setup

Windfields over the Gaudergrat ridge have been computed using the meteorological model ARPS, developed at the Centre for Analysis and Prediction of Storms at the University of Oklahoma. It solves the 3 dimensional, non-hydrostatic, compressible Navier-Stokes equations (Xue et al., 1995, 2000, 2001) and offers the possibility to run it with a Large Eddy Simulation (LES) configuration.

4.4.1 ARPS general setup

The LES configuration is used for all the numerical computations presented in this study. Several subgrid scale turbulence closures are available in ARPS, including the 1.5-order Turbulent Kinetic Energy TKE (Deardorff, 1980; Moeng, 1984) based on the Smagorinsky-Lilly static models (Lilly, 1962; Smagorinsky, 1963). Depending on the mixing length expression, the TKE approach can be formulated so that it can adapt to fine and coarse resolutions (Sun and Chang, 1986). This last formulation is especially useful when a large fraction of the velocity scales is contained in subfilter scales, as it is the case for coarse resolution grids (Pope, 2000, chap.13) or in mesoscale models.

The equations are solved using finite differences with a fourth-order spatial differencing scheme for advection terms, and a mode-splitting technique for the temporal terms to suppress high frequency acoustic waves. At small time steps, the acoustically active terms are computed, and the other variables are computed at large time step intervals. Hence the acoustic wave speed limits the small time step size. The choice of the time step is limited by the Courant-Friedrich-Levy (CFL) stability criteria. A Leapfrog scheme is used for the large time steps, and a first-order forward-backward explicit scheme is used to solve the small time steps, except for terms responsible for vertical acoustic propagation which are computed with a semi-implicit scheme. An Asselin time filter is applied every small time step to remove numerical high-frequency perturbations. The Asselin coefficient is set to 0.01 to remove oscillations without filtering all the small scales motions (See details in Chapter 3). A fourth order computational mixing (with a coefficient of 10^{-3}) and a divergence damping term are also applied.

The lateral boundary conditions are time dependent and provided by the one-way nesting technique. This point is described in the following section. The top boundary is set to zero gradient and the bottom boundary is a rough rigid wall. All

the equations are solved on a staggered grid (Arakawa-C grid) which is a validated approach for many applications, as it generally enhances stability and accuracy.

Computations are run with ARPS5.2.4. Version 5 is based on ARPS Submeso formulation for steep terrain, but differs by the addition of enhanced soil model, the implementation of the shading module, and the parallel computing interface.

The simulations are performed using the parallel version of the code on AMD opteron processors from the cluster (Sun Grid Engine) at the Swiss Federal Institute for Forest, Landscape and Snow (WSL) and at the Swiss Supercomputing Centre (CSCS) on AMD Opteron processors the Cray XT3 platform. Computing performances information can be found in Appendix A.

4.4.2 Nesting from aLMo outputs to the ARPS finest grid

Previous studies have shown that simulations over complex mountainous terrain are highly sensible to initial and boundary conditions (Raderschall et al., 2008, submitted). The nesting technique provides time dependent boundary conditions imposed by a larger, coarser grid and and was proven suitable for airflow computations over complex terrain (Chow et al., 2006; Weigel et al., 2006).

In the present study, the nesting technique is applied, starting with the Meteoswiss Alpine model (aLMo) outputs with a spatial resolution of 7km down to ARPS finest resolution of 25m. The Meteoswiss Alpine model aLMo is adapted from the Lokal Model from the German Weather service (DWD) to the Alpine region. This meteorological model has been chosen for its higher resolution compared to ECMWF (7km instead of 9km) and its adaptation for Alpine terrain computations. To the knowledge of the author, it is the first time that these two meteorological models are coupled. Only a part of the aLMo numerical domain was used for the interpolation on the ARPS coarsest grid and it is centred on the region of intersest. A schematic representation of the nested domains is given in Figure 4.6. Four one-way nested domains are used with horizontal resolutions of 1.6km, 400m, 100m and 25m. The grids overlap and are centred over the Gaudergrat Ridge region. The interpolation of the lateral boundary fields from coarser grids on finer grids matches the three velocity components, the pressure, the potential temperature and the humidity. A linear interpolation method is used for all grids.

The aLMo data are used for the initialisation and hourly boundary forcing of the coarsest domain. As suggested in Warner and Peterson (1997), all these grids

are centred on the Gaudergrat ridge, with a relaxing zone at boundaries of 5 to 7 grid cells. The number of grid cells in the relaxing zone depends on the size of the domain : 7 grid cells for the larger numerical domains (with 99×99 points) and 5 grid cells for the smallest grid (67×67 points).

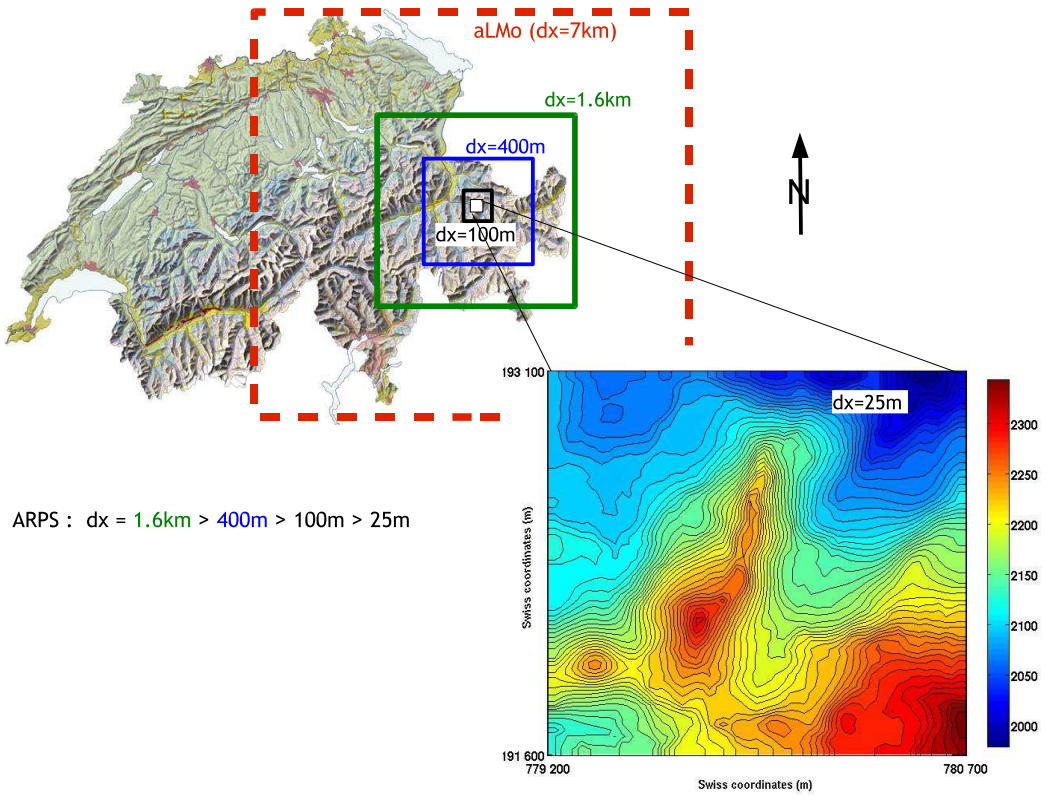

Figure 4.6: Schematic representation of the nested domains.

The topographies have been constructed using the Swiss Digital Elevation Model (DHM) datasets DHM25 and DHM100, which have respectively a resolution of 25m and 100m. These dataset are then rewritten in the ARPS terrain file format. The interpolation of the 100m resolution dataset for the 1600 and 400m grids are processed in ArcGIS with a nine-point filter in order to avoid sharp edges at grid points. The Gaudergrat ridge is surrounded by higher and larger mountains and it is recognisable in the numerical domain when the horizontal resolution is 100m or finer. The differences between two nested grids remain large, as presented for example between the 25m and 100m resolution grids in Figure 4.7.

For the finest resolution domain, a damping layer is used : it extends from the top boundary down to about one third of the domain vertical length. This compensates a rather small vertical extension for this domain (about 3km).

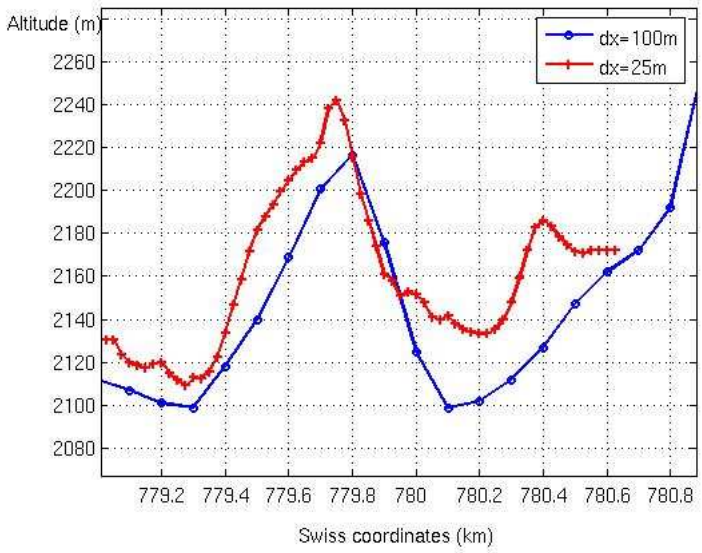

Figure 4.7: Comparison of a cross section from the nested domains with horizontal resolution 100m and 25m.

(nx,ny,nz)	dx (m)	dz (m)	dzmin (m)	Lz (km)	dtbig (s)	dtsml (s)
(99,99,63)	1600	400	50	24	1	1
(99,99,63)	400	300	40	18	0.1	0.05
(99,99,83)	100	200	15	15	0.1	0.01
(67,67,33)	25	100	3	3.5	0.01	0.001

Table 4.1: Nested grids properties

The nested numerical domains boundaries are merged to have similar boundary elevation than the surrounding coarser domain. During the computation of the two finer domains, the Coriolis option was turned off. Indeed as the numerical domains extension is small, this option would lead to strong velocities gradient near the ground. The initial and boundary conditions for the coarsest resolution domain are forced with the MeteoSwiss model aLMo datasets. The current aLMo version has a 0.0625 (about 7km) horizontal resolution with 45 vertical levels and the output

frequency is one hour. Consequently the boundary condition forcing is updated hourly. Two configurations have been tested: in the first one, there is only one initialisation at the beginning, whereas in the second one, the run is re-initialised. The optimum time for the reinitialisation depends on the size of the domain. A reinitialisation every hour on the smallest domain has been tested, but did not avoid the spurious effects, such as non-realistic accelerations, that can develop at the boundary.

For a steep topography, the vertical resolution has to be chosen carefully to avoid distortion and instabilities. The aspect ratio $\Delta z/\Delta x$ has to be small. For the smallest horizontal resolution domain, the aspect ratio $\Delta z_{min}/\Delta x$ at the surface is about 8 (Table 4.1). It is also necessary to find a compromise between a finer grid to resolve the first meters of the atmosphere which interests us for snow transport modeling and computation duration. For better results, the run has to be started about 6 hours before the beginning of the selected day so that the flow is well established though the domain. Indeed once the flow is developed it stays stable in the interior of the domain and the boundary forcing is adapted progressively.

4.4.3 Surface data and bottom boundary condition

ARPS provides a land-surface soil-vegetation model for surface energy and moisture budget equations (Xue et al., 1995, 2001). As found in the Riviera Valley simulations (Chow et al., 2006; Weigel et al., 2006), the surface cover description improves the results. For the nested domains of resolution 100m and 25m the surface data Arealstatistics 85 from the Swiss Federal Office for Statistics have been used to construct surface description files. For the domain of resolution 100m and 25m the data have been corrected with orthophotos covering the same area. Consequently the ARPS land-surface soil-vegetation model has been modified to read and integrate the vegetation categories relative to the Alpine landcover. It contains 24 categories, among which some specific to the mountainous regions : firn, ice, rock, alpine and sub-alpine meadows.

The surface data are part of the bottom boundary conditions, which forces the flow through heat exchanges and roughness lengths. A two-layer soil model is applied which uses the force-restore method (Noilhan and Planton, 1989; Pleim and Xiu, 1995). The soil model is connected to the airflow via a wall model that models the contribution of the mean drag on the flow and the contributions of small scales

fluxes due to the surface roughness or heat fluxes fluctuations. The bulk aerodynamic formulations of the heat and momentum surface fluxes introduce drag coefficients that depend on the stratification just above the ground and on the roughness length (Buyn, 1990; Louis et al., 1981; Noihlan and Platon, 1989). This parametrisation plays an important role in the case of thermal air flows.

4.5 Results

4.5.1 Surface mean flow comparisons

The general flow features observed during the Gaudex (Hug et al., submitted; Lewis, 2006), as described in section 2.1 are also observed in the model results. The cross-ridge flow appears independently of the inflow wind direction as presented in Figures 4.8 and 4.9, at 6:00 and at 12:00, where the inflow wind direction is respectively south-west and south. At lower altitudes, it is possible to recognise flow parallel to the ridge on both sides. The flow separation from the ridge crest on the lee slope is well represented in Figure 4.8(a) and 4.9(a), at 6:00 and 17:00. A situation with a southerly wind, like in Figures 4.8 and 4.9, is influenced by thermal effects whereas westerly wind situations with a cross-ridge flow (Figures 4.8(a) and 4.9(a)) tends to be driven by pressure gradients (Lewis, 2006).

Figure 4.10 shows a vertical slice of the flow at the cross-section symbolised by the SLF AWS (sites 22 to 26), following the coordinate line Y=192.2 km (see Chapter 2 Figure 2.3). The separation of the flow from the crest appears clearly as well as the reattachment further near the foot of the lee slope (Lewis, 2006; Raderschall et al., 2008, submitted). The flow acceleration at the ridge due to the Venturi effect can also be identified.

The eddy at the north end of the ridge (as explained in section 4.3) is also present in the numerical results, although shifted a little to south-east (Figure 4.9(b)). As a difference to previous windfield simulations over Gaudergrat (Hug et al., submitted; Raderschall et al., 2008, submitted), the flow stays stable and can be computed over a longer time and for any wind direction and not only for stable atmospheres. The nesting technique permits to simulates larger types of conditions than with a horizontally homogeneous initialisation.

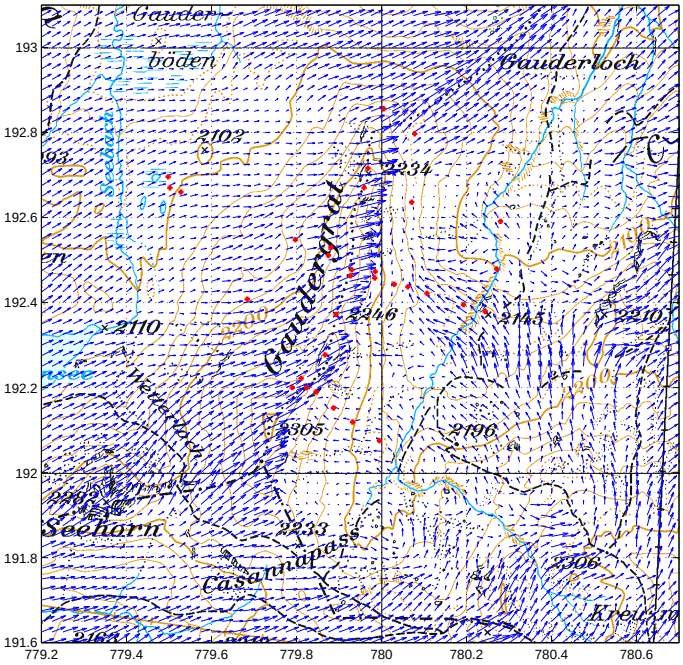

(a)

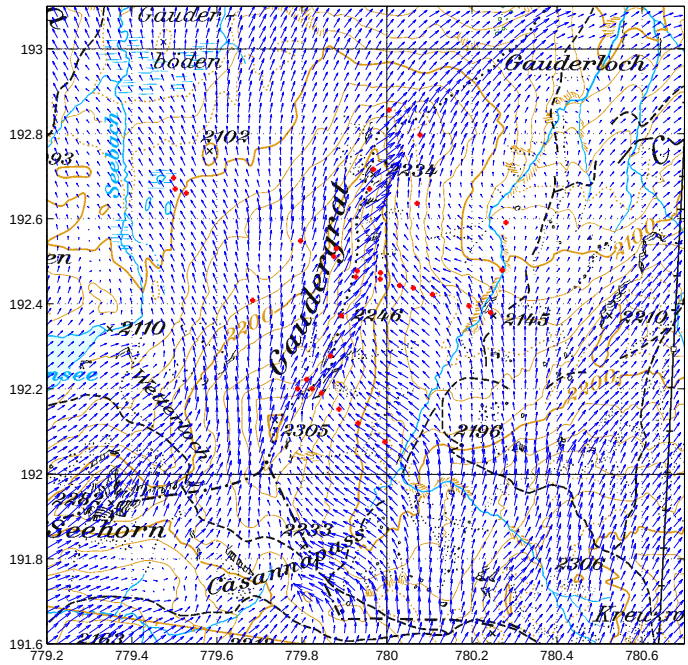

(b)

Figure 4.8: ARPS Windfields on August 18, 2003. Horizontal cross-section at the first level above the surface (about 3 to 5m above ground), at (a) 6:00 UTC and (b) 12:00 UTC. The red crosses represent the measurements sites locations.

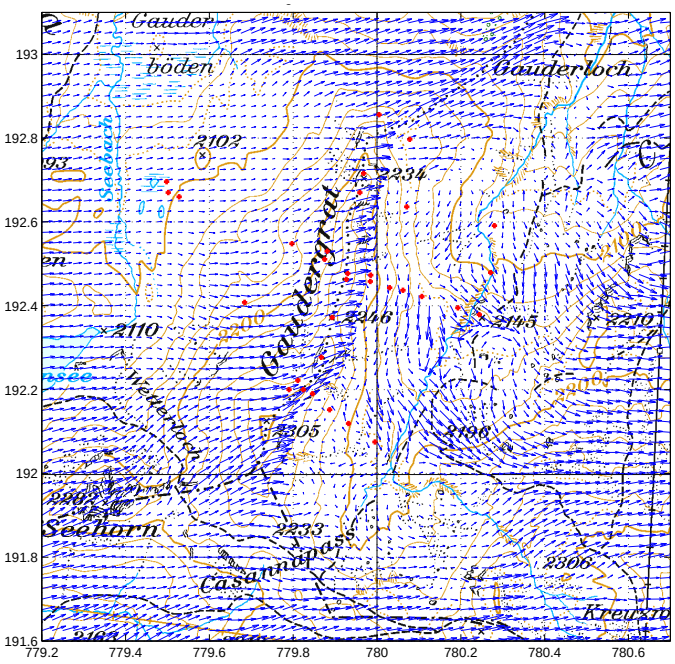

(a)

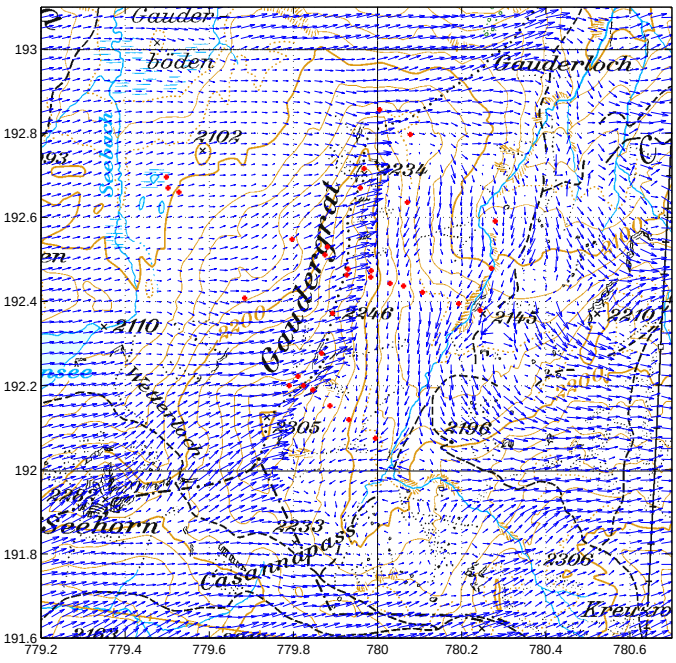

(b)

Figure 4.9: ARPS Windfields on August 18, 2003. Horizontal cross-section at the first level above the surface (about 3 to 5m above ground), at (a) 17:00 UTC and (b) 20:00 UTC. The red crosses represent the measurements sites locations.

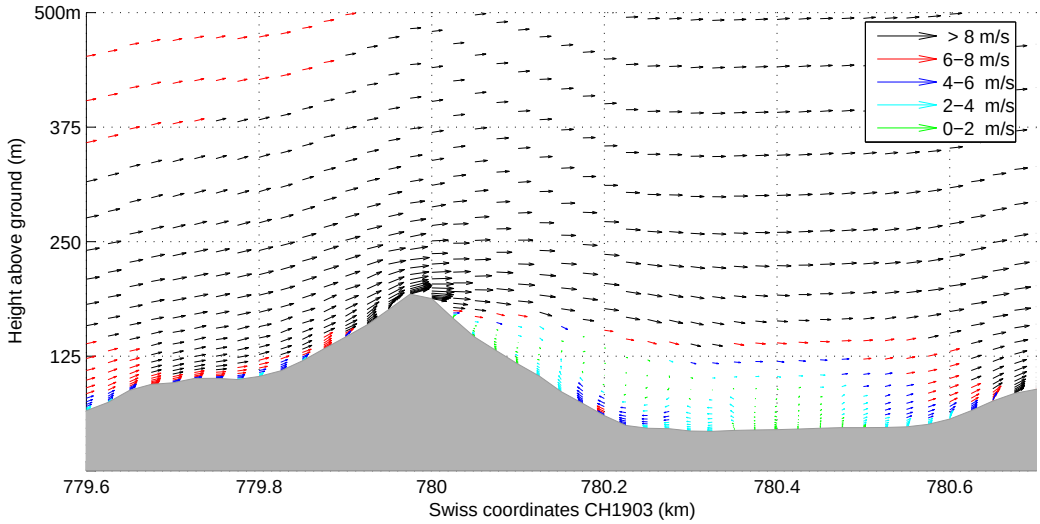

Figure 4.10: Vertical slice of the ARPS windfields along the northwards coordinate line Y=192.2 km, on Aug. 18, 2003, at 6:00 UTC

The effect of nesting on the mean windfields structure can also be quantitatively compared with the Gaudex AWS measurements. The mean wind time series (Figures 4.11, 4.12 and 4.13), for both days, show a good agreement with measurements when the flow is synoptically influenced. However wind direction changes due to thermal effects are weakly represented in ARPS results as shown for example in Figure 4.11, in the wind direction time series at sites 27 and 22, located on each sides of the ridge, in the afternoon. In the Riviera valley study, Chow et al. (2006) and Weigel et al. (2006) have shown that the soil moisture is an important parameter for thermal winds. In the present computations, the soil moisture is included as a constant value for the whole domain, and the soil temperature is derived from the air temperature near the surface (so-called force-restore parametrisation). This setting could account for the differences. Nevertheless, for winter flow computations, the soil is frozen, and therefor the soil moisture and soil temperature initialisation is not an issue.

With a resolution of 25 meters, topographic details are smoothed, especially near the crest and it influences the whole air flow. These topography differences are important especially when comparing with the AWS measurements recorded at 2 meters above the ground. Indeed at sites 9 and 2 (see Figure 4.13), a constant wind direction shift of about 80 degrees can be observed. ARPS results show a south-

easterly wind instead of a south-southwesterly wind in the morning. As mentioned previously, the observed eddy at the ridge north end is shifted in ARPS towards the south-east and contributes to the wind direction shift in the zone.

As shown in Figure 4.8, ARPS windfields show a re-attachment at the north end of the ridge, whereas in the observations there is an eddy with a vertical axis located at this place. The eddy obtained from ARPS is shifted a little to south east, this explains the differences in the wind direction times series at site 18 (see Figure 4.12) where the modeled wind direction is north-east instead of north-west. At this site, the wind speed is also overestimated in the evening (see Figure 4.12). This is due to a too strong forcing from the outer grid. Indeed the external windspeed interpolated from the coarser grid (dx = 100m) is about 15 m/s at this location (see Figure 4.14). The influence of the lateral boundary forcing is large at points located near the boundary relaxation zone, as it is the case for site 18, whereas in the interior of the numerical domain, the flow is quite stable.

The wind speeds used for the comparisons have been measured with Young propellers. Hence the wind direction measurements are less accurate for wind speeds which are less than 1 m/s. Consequently the differences in the wind directions observed on August 18 in the evening (for example at site 16, Figure 4.12), may not be so large.

In addition to what has been observed for August 18, results for August 11 show a computed velocity larger than the measured one until about 8:00 UTC, as can be seen in Figure 4.16, at sites 27 and 16. This overestimation of the velocity correlates well with the discrepancies observed in ARPS wind direction. The synoptic forcing provided by aLMo outputs for wind speed and direction on this day presented discrepencies with measurments at the Weissfluhjoch station (see Figure 4.15). This differences have propagated through the four nested domains and consequently the local circulation in the finer grid is still influenced by this errors.

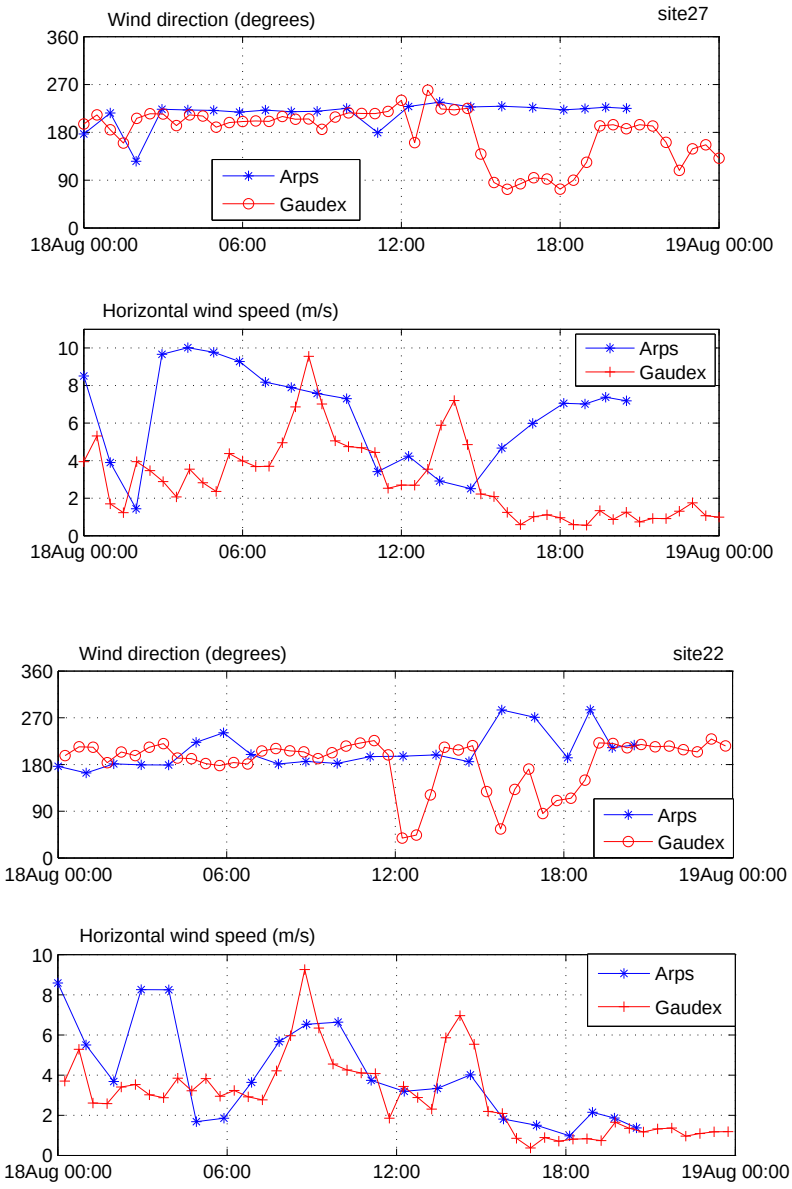

Figure 4.11: Time series for wind direction and speed from ARPS results and Gaudex Measurements on August 18, 2003, respectively at site 27 (above) and site 22 (below). The Gaudex data are averaged on 30 minutes.

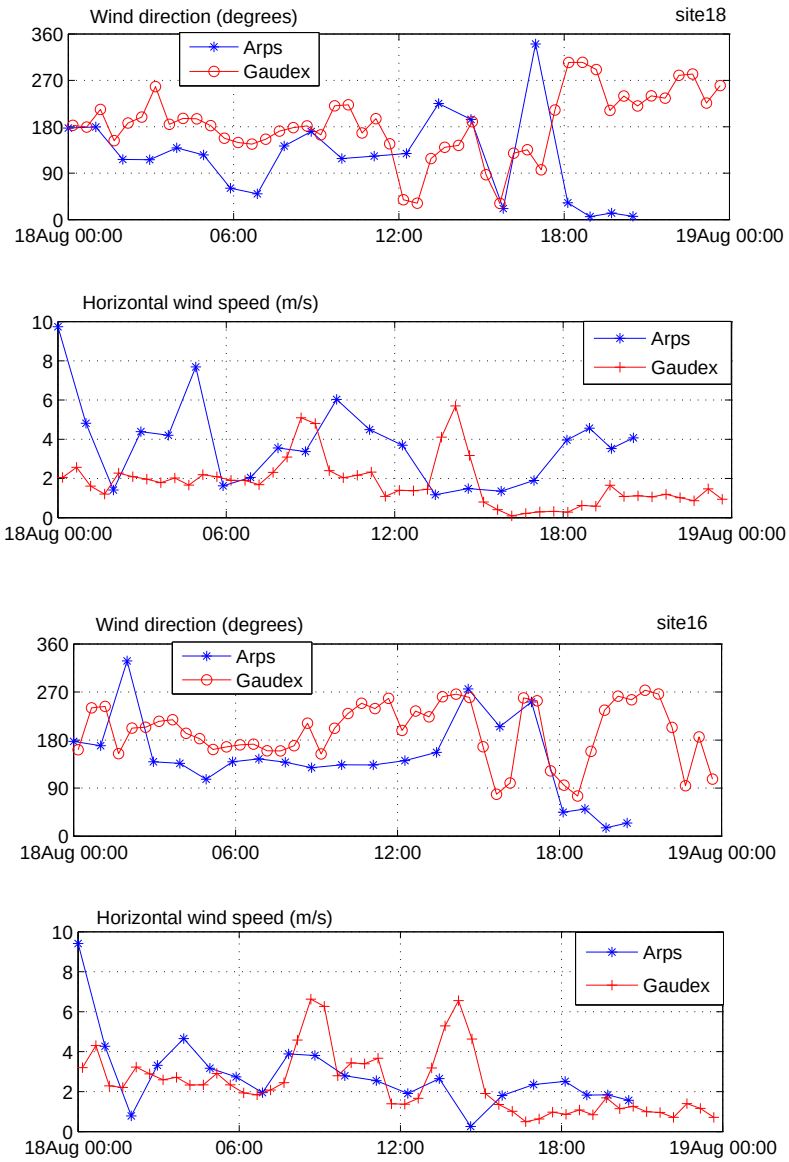

Figure 4.12: Time series for wind direction and speed from ARPS results and Gaudex Measurements on August 18, 2003, respectively at site 18 (above), site 16 (below). The Gaudex data are averaged on 30 minutes.

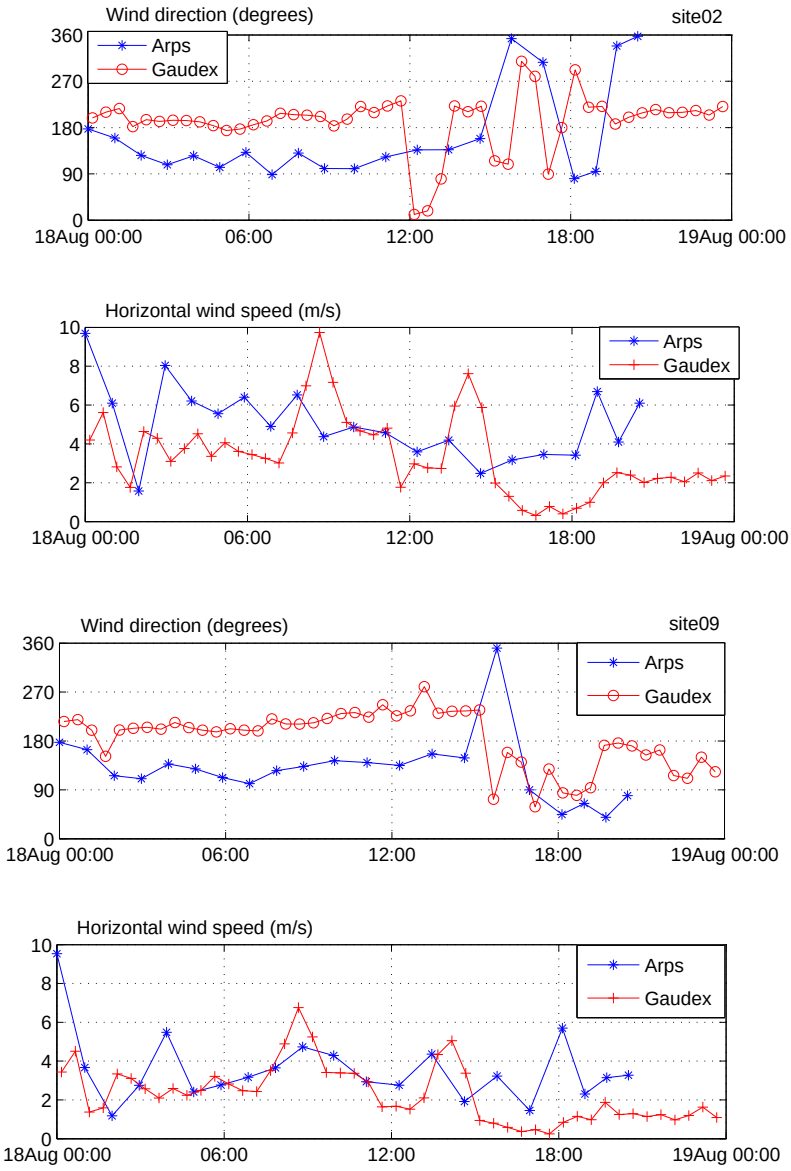

Figure 4.13: Time series for wind direction and speed from ARPS results and Gaudex Measurements on August 18, 2003, respectively at site 02 and site 09. The Gaudex data are averaged on 30 minutes.

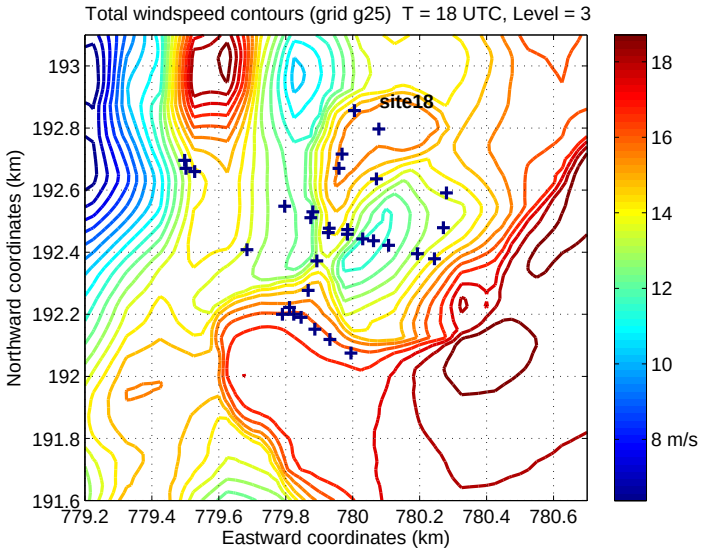

Figure 4.14: Interpolated total windspeed from the outer grid with dx=100m on the finest grid with dx=25m. The windspeed contours are shown at the first level above the surface, on August 18, 2003 at 18 UTC. The crosses represent the measurement stations.

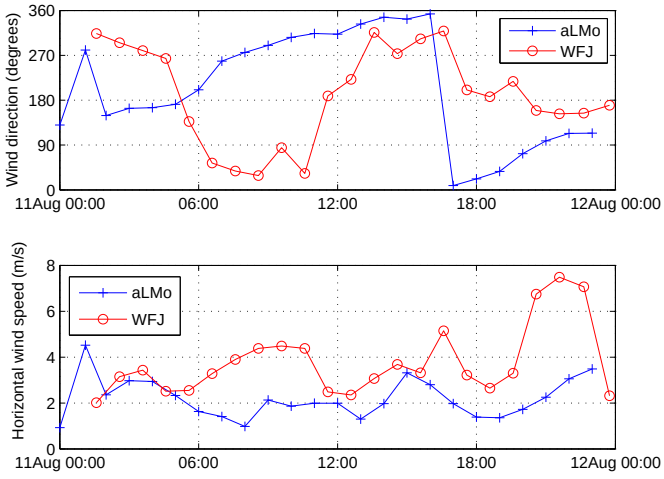

Figure 4.15: Comparison of time series for wind direction and speed from interpolated aLMo results on the grid with a resolution of 1600m and measurements at the Weissflujoch station (2663m) on August 11, 2003.

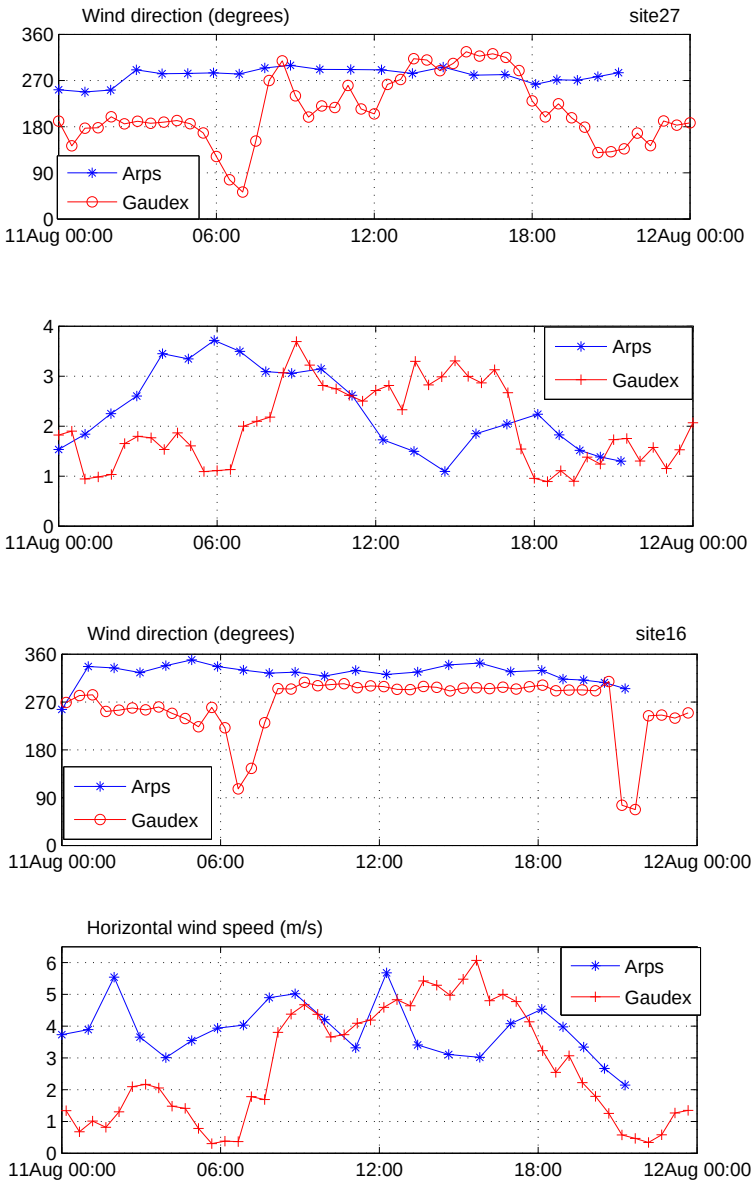

Figure 4.16: Time series for wind direction and speed from ARPS results and Gaudex measurements on August 11, 2003, respectively at site 27 and site 16. The Gaudex data are averaged on 30 minutes.

4.5.2 Turbulent kinetic energy (TKE)

TKE time series

The turbulent kinetic energy (TKE) per unit mass (equation 4.1) is a measure of turbulence intensity and an important parameter for the snowdrift computations. It is also an interesting parameter for turbulence studies in sloping terrain, as it is independent of the coordinate system. TKE is defined as half of the trace of the Reynolds stresses tensor. Consequently this allows us to ignore the influence of the alignment of measurements with the streamlines, a typical problem when interpreting ultrasonic measurement over steep terrain. The turbulent kinetic energy per unit mass is noted: e

$$e = 0.5(u'^2 + v'^2 + w'^2) \tag{4.1}$$

To analyse TKE, the measurements from uvw-anemometers (sites 23, 24 and 25), fixed at 5m above the ground (See Chapter 2 Figure 2.3) and from sonics located 7.5m (sites 31, 32, 33) were used. The sampling frequency was 1Hz for the first category of anemometers and 5Hz for the second category. Instead of the instantaneous TKE, we consider the averaged TKE, computed as in expression 4.2, which is more representative of the overall flow.

$$\overline{e} = 0.5(\overline{u'^2} + \overline{v'^2} + \overline{w'^2}) \tag{4.2}$$

The mean component of the velocity for the Reynolds decomposition was computed over 30 minutes for all measurement sites. The influence of the average period for the mean velocity component has not shown significant influence on the results. An average over a smaller period gives more scatter between two adjacent time intervals (Lewis, 2006). This point is detailed in chapter 2.

For the time series comparisons, ARPS hourly outputs have been used. Model outputs contains only the subgrid TKE from the prognostic equation, defined in chapter 3. In the 1.5 order TKE SGS model, the mixing coefficients are related to a mixing length and a velocity scale deduced from the SGS TKE instead of velocity strain tensor as in the Smagorinsky SGS model. The formulation of the mixing length depends on the stratification. The complete description is given in (Xue et al., 1995, chapter 6).

As the contribution of the resolved TKE is missing, the following comparisons between the model results and the measurements are qualitative. It can be seen that SGS TKE contains as much energy as the total TKE from measurements,

which already point out that the largest part of the energy lies in the parametrised motions.

On August 18, the two flow accelerations occurring at about 8:30 and 14:00 UTC at site 27 (see Figure 4.3), are clearly recognisable in the TKE time series at uvw-anemometers sites as well as at site 31 (see Figure 4.17). The numerical results show a minimum at around 12:00, similar to what is observed in measurements. According to the Gaudex measurements, the amount of TKE decreases after 16:00 UTC, contrary to the model results. The model maxima span over roughly four hours instead of about two hours for measurements. As explained previously, the mean wind quick and sharp changes are difficult to reproduce with the model, and this influences also the TKE results. In both measurements and model results, the time series maximum TKE is found at the ridge (see Figure 4.17). On August 18, with southwesterly winds, the leeward and windward sides are clearly distinguished and the speed-up is maximum at the ridge crest. As the TKE is roughly proportional to the mean wind speed, it is maximum as well at the crest and minimum in the leeward side as observed at site 23 and 31, in both model results and measurements.

On August 11 (Figure 4.18), it is interesting to see that for all locations the same cycle can be observed. TKE increases as the wind speed increases and simultaneously when the local wind direction turns from south (i.e. parallel to the ridge) to north west (perpendicular to the ridge), as shown in Figure 4.3. This feature is well reproduced by the model as well. Indeed it is in agreement with the production term in the TKE prognostic equation, which is proportional to the mean wind component strain.

The TKE computed from ultrasonics measurements is larger on the east slope between roughly 8:00 UTC and 16:00 UTC. On this day, the synoptic wind turns from north east to north west over south during this period, as can be seen in Figure 4.2. Consequently on the east side is the windward side in the morning and cannot clearly be defined as the leeward side in the afternoon. However the modeled TKE values are larger on the west slope and at the crest, due to the synoptic forcing that was too strong and leads to wind directions changes especially in the morning. Another important aspect is the shift of the period with high TKE production. In ARPS this shift starts at 1:00 UTC instead of 7:00 UTC in the sonics measurements. Indeed in the ARPS computations for August 11, the wind speeds were also too high in the morning and the mean wind speed influences directly the TKE.

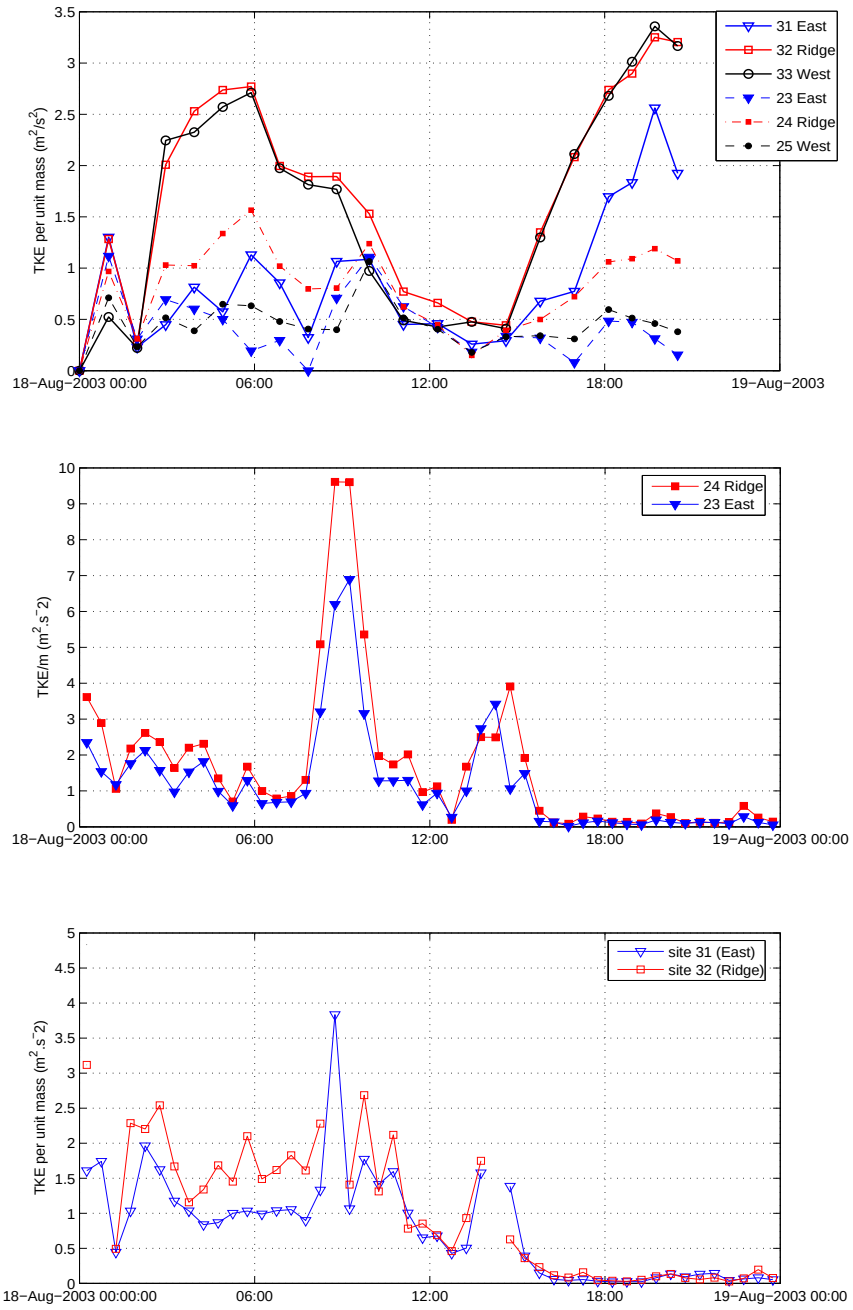

Figure 4.17: Time series of the TKE per unit mass on August 18, 2003, from (respectively from top): a/ ARPS sub-grid scale model at locations corresponding to UVW anemometers (full symbols) and ultrasonics sites, b/ UVW anemometers data (sites 23 and 24) at 5m height, c/ ultrasonics data (sites 31 and 32) at 7.5m height.

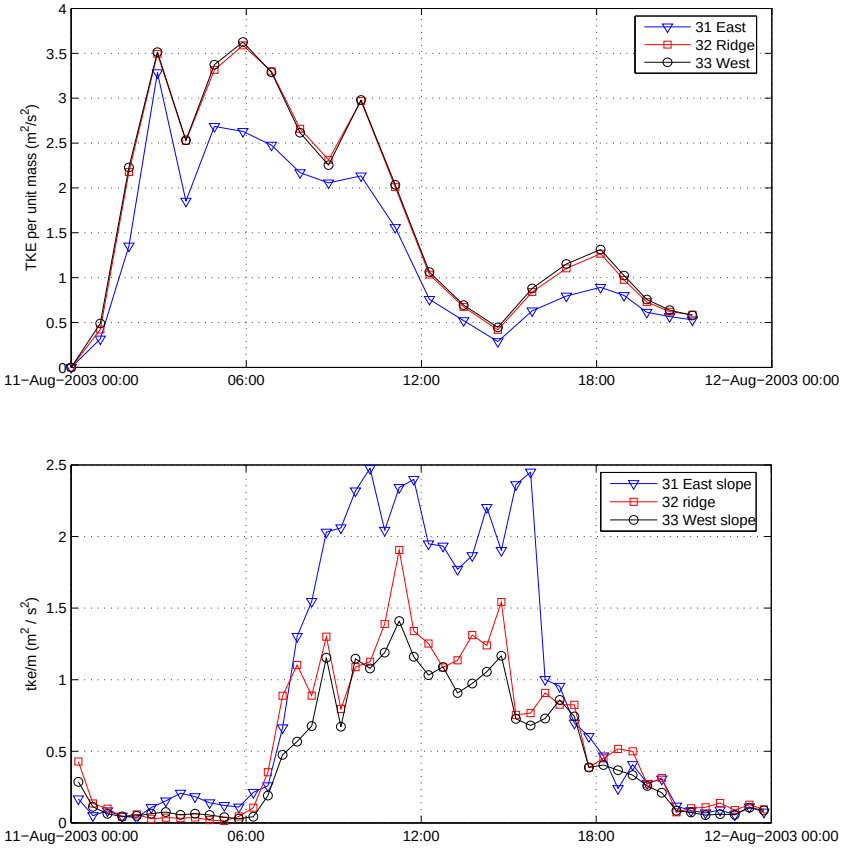

Figure 4.18: Turbulent kinetic energy per unit mass on August 11, 2003, from : ARPS sub-grid scale model (above), sonics data (sites 31, 32 and 33) (below). For the TKE from measurements, the velocity mean component is averaged over 10 minutes

TKE spectra

The spectral analysis of ARPS results informs us on the repartition of the energy through the resolved scales and one can deduce which scales are resolved explicitly. The spectra of TKE per unit mass obtained from the Gaudex measurements, show an energy decrease following the $f^{-5/3}$ law (Figure **??**) as described by the Kolmogorov theory for the inertial subrange, for all sites independently of their location. The fitted slopes give results between $f^{\text{-}1.62}$ and $f^{\text{-}1.75}$ ($-5/3 \approx -1.67$). The energy is also similarly distributed through the scales on the east slope and at the crest. However the production range appears to contain more energy at the ridge. The east slope is often the subject to recirculation, hence the turbulence is more influenced by local smaller scales than at the ridge which is influenced by the larger eddies coming from the surrounding mountains, as explained in Chapter 2.

For comparison, ARPS TKE spectra have been constructed at the grid points corresponding to sonics locations, at the first level above the surface, i.e. at about 3 meters above the ground. The spectra are presented for August 18, which is also representative of August 11. The resolved TKE is computed using equation 4.2 with a time series of the velocity components, whereas the total TKE is obtained by adding the SGS TKE from the prognostic equation. The time series contains the results from the grid point representing the sonics location, as well as from the two surrounding grid points along the north-south line (y coordinate). This grid points are considered close enough to ensure homogeneity. The output frequency is based on the ARPS large time step ($dt = 10^{-2}s$), thus the number of points used for the spectra construction is about $O(10^6)$. The spectra computed from ARPS results are presented in Figure 4.19 for site 32 (ridge crest), at the first level above the surface for comparison with the surface observations. The spectra for the two other sites are similar and hence not shown. A deficit of energy clearly appears in the resolved TKE : the smooth line indicates that the whole energy comes from the parametrisation

The spectra computed with the Gaudex measurements (see Figures 4.20 and 4.21) show an inertial subrange starting at a frequency of $3.10^{-2}Hz$. With a mean wind speed of 3m/s, it can be deduced that eddies with size smaller than about 100m originate from to the inertial subrange. The spectra have been computed from sonics measurements with a longer time series to produce a clearer transition from production range to inertial subrange.

The filter size in the current ARPS computations is :

$$\Delta = (\Delta x \Delta y \Delta z)^{1/3}$$

where $\Delta x, \Delta y, \Delta z$ are the grid size in the x, y, z-directions.

According to this expression the filter size is about 40 meters. Consequently ARPS should be able to resolve eddies up to the inertial sub-range, as recommended by Moeng (1984) for three dimensional LES of the atmospheric boundary layer. However in the current simulations, these scales do not show significant resolved energy. The small scale fluctuations are not transferred from the outer grid to this finer grid, but are expected to develop during the simulations on the finer grid. One reason can be the small size of the numerical domain. However the finer numerical domain cannot really be extended due to computational cost. The boundary conditions are modified to facilitate the development of turbulence.

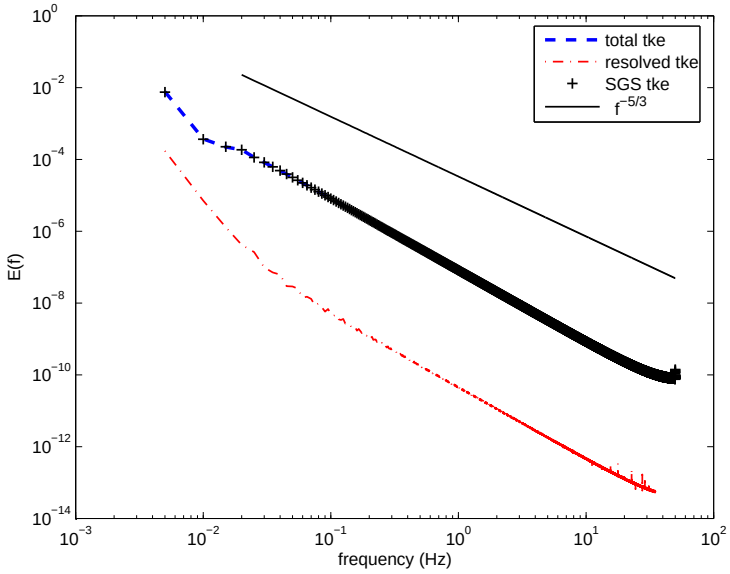

Figure 4.19: Energy spectra of TKE per unit mass, from ARPS results at sonic site 32, on Aug. 18, 2003, 15:00 UTC

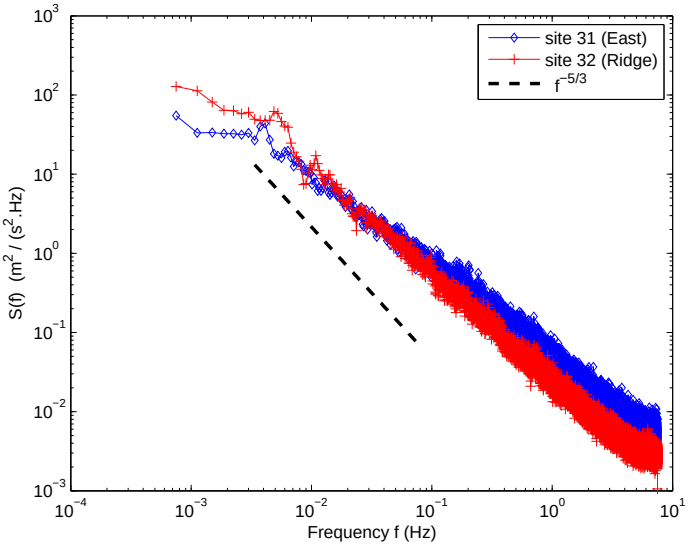

Figure 4.20: Energy spectra of TKE per unit mass at sonics sites, Aug. 18 to 25, 2003.

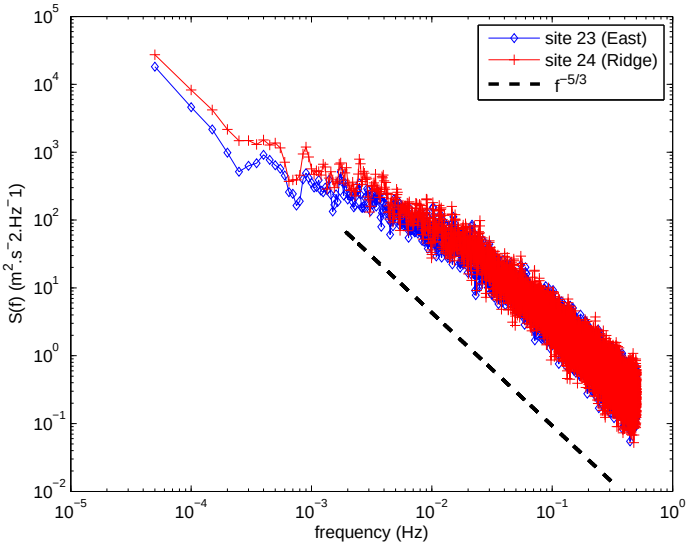

Figure 4.21: Energy spectra of TKE per unit mass at uvw-anemometers sites, Aug. 18 to 25, 2003.

4.5.3 Modification of lateral boundaries conditions to facilitate resolved turbulence

ARPS parameters setting has been studied in chapter 3 to resolve the energy containing scales. In the results shown in the previous section, the external forcing at the lateral boundaries stabilises the mean flow but damps the resolved turbulence. The outer nested grid has a filter size of about 150m and cannot pass small scale turbulence to the finer grid. This is a known issue of the one-way nesting technique: as reported by Paegle et al. (1997). The one-way nesting technique constrains the development of initial perturbations in limited area models and the interpolation of the external boundary conditions lack of fine scale turbulence. Moreover the lateral boundary conditions updates are relatively infrequent and acts as a filter. Nutter et al. (2004) proposed a method for ensemble prediction systems to restore small scale variances and ensemble dispersion. A two dimensional perturbation field is generated using inverse Fourier transforms and is added to the lateral boundary conditions. The amplitude of the perturbation is determined by the error variance spectra differences between global ensembles and local area model ensembles, whereas a random phase angle is applied to each wave number. The perturbation field has a zero mean, is periodic in x and y directions and remains coherent in space and time.

A method to keep the turbulence of the flow was proposed by Spalart (1988) in the context of engineering flow computations and applied by Mayor et al. (2002) in order to compute the development of an internal boundary layer associated with a cold air outbreak. The method is based on the recycling of turbulence from a vertical plane located downstream of the flow. The simulated turbulent perturbations and reintroduced at the inflow boundary on the mean profile. The mean profile obtained from a precursor run is maintained constant over the whole simulation. This method works well, provided that the wind keeps blowing from the same direction. This is more difficult to apply when computing on full day over an Alpine ridge.

In the current study a simple method that does not require to work in the Fourier space is tested to help generating turbulence at the lateral boundaries. In the ARPS nested grids configuration as presented previously, the variables at lateral boundaries remain constant over a hour until a new boundary condition file is read. The proposed method uses the outputs from a separate run over a flat terrain with periodic boundary conditions presented in chapter 3, section 3 are now used to

construct a three-dimensional boundary condition perturbation field containing the fluctuating part of each velocity component. The amplitude of the perturbation field remains small in order to avoid a discontinuity at the border. After the perturbation field is constructed, it is added at each time step to the spatially and temporally interpolated lateral boundary condition from the outer grid. In this new configuration, the boundary condition update applies at each time step. The boundary conditions relaxation zone covers 5 grid points. The model was run in this new configuration for 30 minutes only because of the large amount of data required by the boundary condition files. The flow remained stable over the whole simulation.

The resulting spectra for TKE are computed with the same method as previously at the first level above the surface (see Figure 4.23). At 15 UTC, on August 18, the wind is westerly, consequently, the sonic site 31 on the east slope is on the leeward side. At site 31, the SGS TKE contribution is really small, indeed the spectra for total and resolved TKE are identical. For clarity, the SGS TKE spectrum is consequently not plotted. In comparison to the previous section spectra, there is more energy in the resolved smaller scales up to a frequency of about $3.10^{-2}Hz$ with the new boundary conditions. This is also clearer at higher level, e.g. at level 10 as shown in Figure 4.22.

In order to estimate the size of the resolved eddies, the u-velocity component spectra at the same grid points are constructed from time series of the resolved motions (see Figure 4.24). The subgrid and subfilters scales are not included, as they are difficult to estimate with the current model configuration. The forecast spectra, computed at the first level above the surface, are found to follow the -5/3 energy decrease up to a frequency of about $10^{-2}Hz$. This indicates that eddies of size smaller than 50m are parametrised. This is in agreement with the effective filter size obtained in the case of airflow simulations over flat terrain, as shown in Chapter 3. This is slightly larger than the filter size (See Equation 3.6), however it is at the first level above the surface (about 3m above the ground), and it is a region where it is difficult to capture all the turbulent motions as they become smaller near the ground. In the results presented here, the thermal turbulence is also present, contrary to Chapter 3, where only the mechanical turbulence was investigated. This method permits to resolve explicitly smaller scales of the turbulence. To avoid the storage of a large amount of boundary condition files (1 boundary condition file per time step), the perturbations could be recycled and added at each time step to the

mean flow provided by the nested boundary condition files.

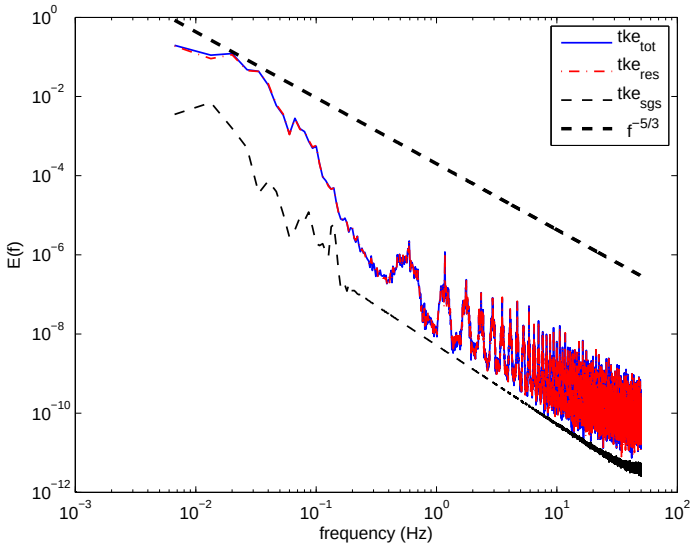

Figure 4.22: Turbulent kinetic energy spectra from ARPS results of the Aug. 18 simulations using the new boundary conditions, site 33 (west). These spectra are computed at the level z=10, which is about 100m above the surface.

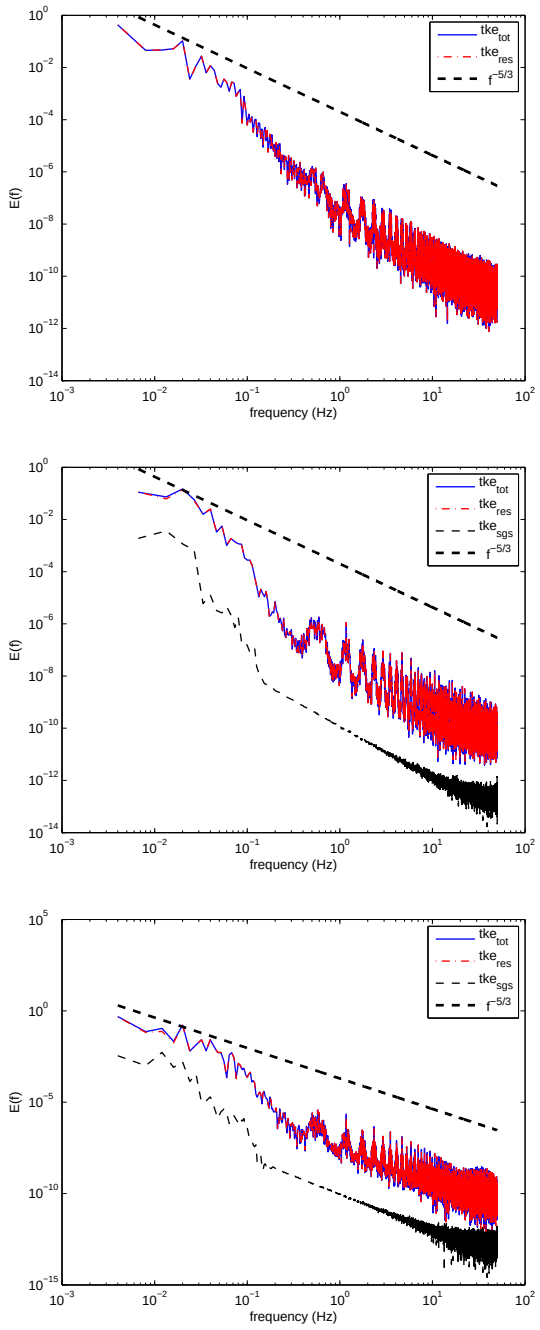

Figure 4.23: Turbulent kinetic energy spectra from ARPS results using the new boundary conditions, for Aug. 18, at, respectively from top : site 31 (east or lee side) , site 32 (crest), site 33 (west or windward side). These spectra are computed at the first level above the surface (z=3, i.e. about 3m above the surface).

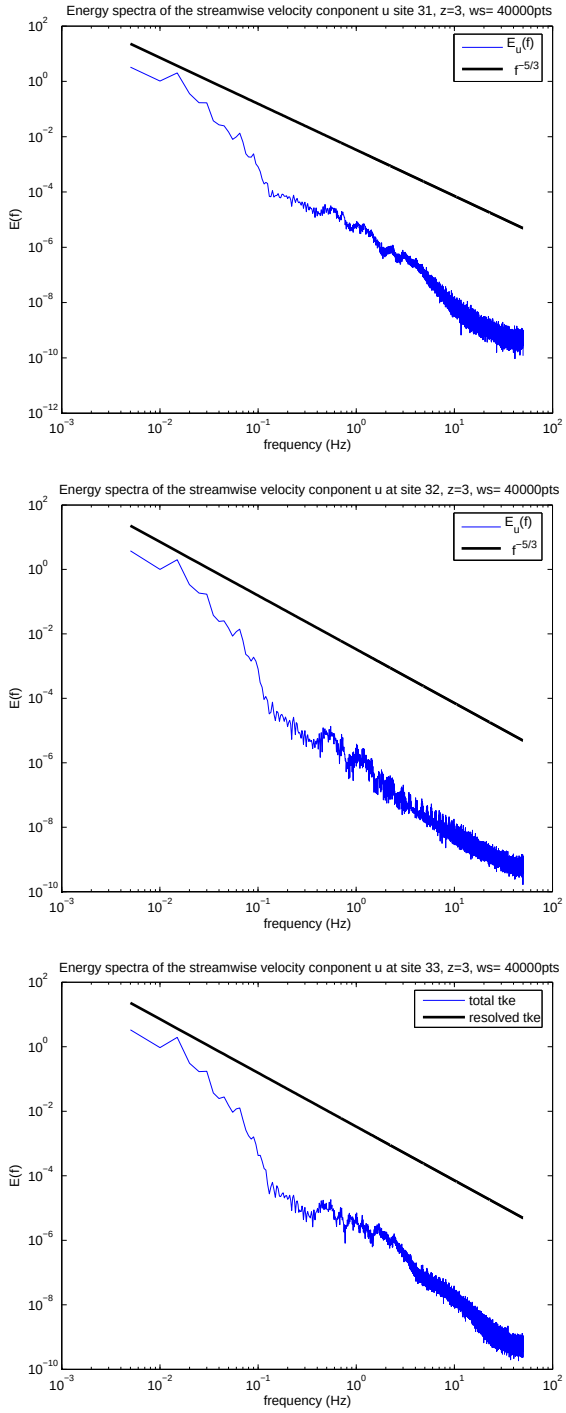

Figure 4.24: U-velocity component spectra from ARPS results using the new boundary conditions, for Aug. 18. These spectra are computed at the first level above the surface (z=3), respectively from top: site 31 (east), site 32 (crest), site 33 (west)

The normalised TKE vertical profiles from ARPS (see Figure 4.25) show that the leeward and windward slopes can now be distinguished. There is more TKE in the windward side and at the crest than in the leeslope where the recirculation occurs. In the traditional one-way nested simulations the TKE is similarly distributed on both sides of the ridge.

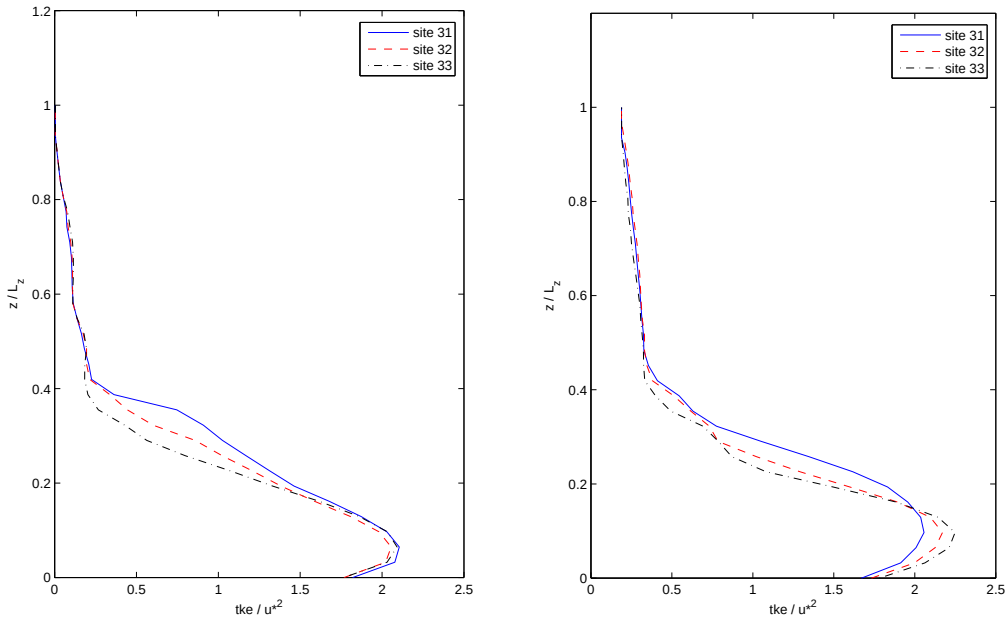

Figure 4.25: Normalised TKE profiles from ARPS : with simple one-way nesting boundary condition (left), and with addition of perturbations (right)

The feedback on the mean flow is difficult to evaluate as the duration of the computation was limited in time. However the results obtained after 30 minutes, give similar values for the mean wind as with the previous boundary conditions (see Figure 4.26). Discrepancies can be observed at the north end of the ridge. The eddy is shifted towards the north with the new boundary conditions and there is no re-attachment of the mean flow in this region. This can be explained by the shorter time allowed for to the flow to develop. The differences between the two windfields appear near the boundaries but do not affect the mean flow at the ridge. In time series of the velocity components, no periodic patterns could be detected. Consequently the small fluctuations introduced at the border permits the turbulence to develop inside

the domain without recirculating the same structures. In addition, if we consider TKE as a representation of the turbulence, the major part of turbulence is located in the first 300 to 400m above the ground in the case of airflow simulations over the Gaudergrat ridge, whereas for simulations over flat terrain (see Chapter 3), the variance profiles show that the turbulence was concentrated between 300 and 1400m.

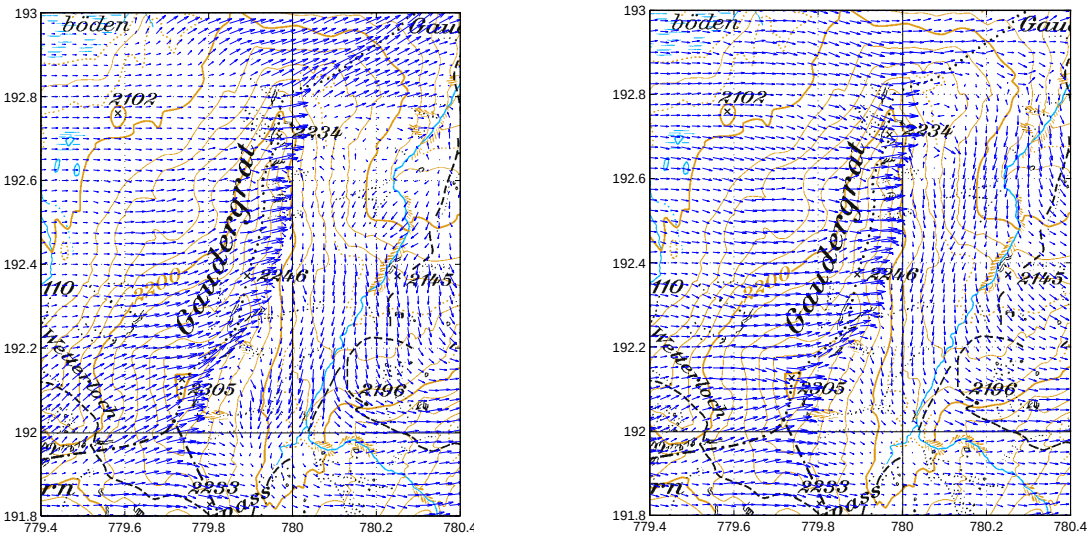

Figure 4.26: Two-dimensional windfields at the first level above the surface (z=3): with simple one-way nesting boundary conditions (left), and with addition of perturbations (right). The abscissa show the eastwards Swiss coordinates (km) and the ordinates represents the Swiss northwards coordinates (km)

4.6 Conclusion

Two meteorological models, aLMo and ARPS, have been coupled to compute windfields over an Alpine ridge, down to a resolution of 25 meters. This is the first time that this combination has been used with a one-way nesting technique to produce initial and boundary conditions. The computed airflow over the steep Gaudergrat ridge remained stable during the two selected days, even under stronger wind conditions.

The results for mean flow characteristics show a good agreement with observations, although the thermal flows are difficult to reproduce. The influence of aLMo forcing is also recognisable in the finer grid results, especially near the border.

By choosing a fine resolution and a LES configuration, it is expected to resolve explicitly as much as possible small scale turbulence especially near the ground surface, region of interest for snowdrift simulations. However most of the energy was in the SGS, hence parametrised. The nesting technique, although stabilising the mean flow provides too much forcing and filtering due to the coarse temporal update to let the turbulence develop. Turbulent structures are missing from the initial state in the forecasts because the coarser grid cannot pass small scale turbulence. However these structures can be simulated when perturbations are introduced at the boundaries on the finer resolution domain.

The implementation of boundary condition perturbations allows the resolved scales to contain more energy than the subgrid scale motions. Moreover the mean flow is not modified by this turbulent features and the TKE distribution correspond to the observations. The TKE in the recirculation zone is lower than at the crest or in the upwind side, where the windspeed is higher. This new configuration permits to explicitly resolve the flow up to smaller scales of motion. In the case of meteorological simulations, a very fine resolution alone does not permit better resolution of the flow and the turbulence has to be triggered artificially. Nevertheless, from a practical point of view, the method could be improved by the implementation of boundary condition perturbations directly in the code.

Chapter 5

Summary, conclusions and outlook

Windfield simulations over complex topography are a challenging task and many parameters can influence the results. The choice of SGS model coefficients has a strong influence on the turbulence results. These SGS parameters also depend on the type of ABL that is simulated. In this work, the Smagorinsky and 1.5 order TKE closure have been tested over flat terrain and the SGS coefficients have been tuned to better resolve the smaller scales (Chapter 3). Once properly tuned, both SGS turbulence models show similar results. The advantage of the 1.5 order TKE closure is that it takes into account the transport of the TKE. Over complex terrain the TKE is not necessarily dissipated where it is produced. This point determined the choice of the 1.5 order TKE model for the simulations over the Gaudergrat presented in Chapter 4. The turbulence statistics of the numerical experiments over flat terrain indicate that the flow is underesolved in the surface layer. Increasing the vertical resolution near the surface does not solve the problem, as the horizontal resolution remains constant leading to underesolved eddies in the horizontal direction. The variation of the Smagorinsky coefficients with height is let to further developments.

The introduction of a complex topography creates even more difficulties, especially in the initialisation and the boundary conditions: horizontally homogeneous initialisation and periodic lateral boundary conditions, as used before, are not appropriate anymore. To compute windfields over the steep Gaudergrat ridge, the one-way nesting technique has been applied (Chapter 4) using for the first time MeteoSwiss Alpine model aLMo outputs. With this method the computed flow remains stable over the whole simulations (one full day). The Gaudex measurements show satisfying quantitative agreements with the ARPS mean flow features. However the

small scale motions are filtered due to the coarse boundray conditions update. The development of the turbulence has to be facilitated by using a separate run over flat terrain to create turbulent perturbations that are then added to the nested boundary conditions. With these new boundary conditions, the flow is explicitly resolved up to finer scales although the region near the surface remains with underesolved flow. In addition the modeled TKE patterns show better agreement to the observations. A limitation to these nested simulations is the current computing time required. This turbulence generation method is not straight forward yet, and further work should be made on turbulent perturbations generation or considering a two-way nesting approach with turbulence triggering during the initialisation.

Field observations indicate that the airflow is highly intermittent, especially in the lee of the ridge (Chapter 2). This is a difficult characteristic to capture with a meteorological model. Moreover the intermittency of the flow arises the question of the validity of ARPS surface fluxes parametrisation as it is based on the similarity theory which assumes flow stationarity. The lee side of the ridge is more influenced by local small scale turbulence whereas the windward side is more influenced by larger scale turbulence produced by the wake of surrounding mountains. Statistical and spectral analysis show that when the velocity are conditioned according to their mean wind speed turbulence at the Gaudergrat ridge can be described as a composition of subsets of isotropic turbulence, making the prediction of strong wind gusts an dother turbulence features easier. These measurments analysis also show that in complex terrain it is difficult to apply the traditional scaling and averaging laws developed for homogeneous horizontal surfaces.

The windfields simulations of this work have been computed keeping in mind that they should be used in the end for snow transport applications. Indeed some hypothesis have been applied along the simulations, and the simulated Gaudex days focused on strong wind conditions. As a first test, windfields have been computed for the snow storm that occurred from 4 to 6 October 2003 to drive the SLF Snowdrift model. However the patterns obtained for snow deposition or erosion zone show poor agreements with observations. Indeed some ARPS windfields show small numerical instabilities in the North-East edge, at the border and in the first levels above the surface. A hypothesis is that the strong advection through the numerical domain creates a reflection on the topography near the border. Further work is needed to solve this oscillations and instabilities.

The modeling of windfields in the Atmospheric Boundary Layer is of theoretical and practical interests and very high resolution windfields simulations as presented in this work can be applied in weather forecast or particle transport such as snow but also fire smoke, pollutants, pollen... Currently a Numerical Weather Prediction model cannot explicitly represent mountains with less than a few (2 to 4) grid lengths (Wood, 2000). Such a model therefore needs to know what the net effect of mountains of scale less than the effective resolution is on larger scales resolved variables. Consequently the very fine resolution computations presented in this work can contribute to a better understanding of the mountains influence on atmospheric flows for NWP models, and hence permit a parametrisation for mesoscale meteorological models.

Appendix A

Computational performances

Computer performances have increased considerably in the last years thanks to parallel computing. However computational performance often remains a limiting factor when running simulations over a large domain with a fine grid resolution. In the case of ARPS, finite differences methods are used to solve the Compressible Navier-Stokes equations and the Courant-Friedrich-Levy (CFL) stability criteria requires very small time steps. Indeed for the grid with a horizontal resolution of 25m, the small time step is 0.001 s. The simulations presented in this work have been performed on two clusters: The WSL cluster (Zeus) and on a Cray XT3 platform at the Swiss Super-Computing Center (CSCS)

WSL cluster:

ARPS code is parallelised using the Message Passing Interface. The following simulations were run on the WSL cluster (Zeus) which is built of 64 processors. The nodes are AMD Opteron 270 processors at 2GHz. The computing nodes are connected with Myrinet. The code has been compiled with a Pathscale Ekopath compiler for Fortran90.

Cray XT3 platform at CSCS:

The CSCS XT3 system (Palu) consists of 1664 dual core nodes giving 3328 compute processing elements (PEs). The PEs are based on an AMD Opteron CPU running at a frequency of 2.6 GHz (5.2 GigaFlops of peak performance). XT3 system runs the UNICOS/lc operating system, implementing the Linux kernel and the Catamount

lightweight kernel. Compute PEs run the single-task Catamount kernel The whole XT3 (PALU) compute system has therefore a peak performance of 17.30 TeraFlops, and totals of 3.3 TeraBytes of RAM. The code is compiled using the "ftn" wrapper command that actually calls the PGI compiler. This command performs compilations so that the created executables are able to run on the worker nodes of the XT3 system (these nodes use a special stripped-down version of the linux kernel called CATAMOUNT).

Computational performances comparisons:

The computing performance on Zeus cluster and CSCS Cray XT3 platform are presented for the computations of one full day (24 hours), over each nested domains, using the real topography.

dx (m)	(nx,ny,nz)	dtsml (s)	Nb of processors	CPU
1600	(99,99,63)	1	48	144 CPU ($\approx 3h30$)
400	(99,99,63)	0.05	48	2.2 kCPU ($\approx 1day + 21h$)
100	(99,99,83)	0.01	48	8.3 kCPU ($\approx 7days + 6h$)
25	(67,67,33)	0.001	32	11.5 kCPU ($\approx 10days + 6h$)

Table A.1: Computational performance of ARPS on the WSL cluster

dx (m)	(nx,ny,nz)	dtsml (s)	Nb of processors	CPU
1600	(99,99,63)	1	64	42 CPU ($\approx 40min$)
400	(99,99,63)	0.05	64	192 CPU ($\approx 3h$)
100	(99,99,83)	0.01	16	1 kCPU ($\approx 1day + 38h$)
25	(67,67,33)	0.001	16	3.5 kCPU ($\approx 9days$)

Table A.2: Computational performance of ARPS on the CSCS Cray XT3 platform

According to these tables, to compute one full day using the nesting technique, it took about 23 kCPU (about 20 days) on the WSL cluster and 4.7 kCPU (about 11 days and 17h) on the CSCS Cray XT3 platform. The advantage on Palu is that due to the large amount of processors, the day (24 hours) can be divided in sub-simulations of one hour each that can be run simultaneously. Which is hence quicker, although requiring some more preparation for the 24 inputs.

The code required some adaptation to be run at CSCS and be more efficient with the fine resolution domains (100m and 25m). It was found that the code is more efficient with 16 to 32 computing nodes, in order to reduce communication time between the processors.

Appendix B

Slope angles of the 25m resolution grid

The 25m resolution digital elevation model from SwissTopo give slope angles from the Gaudergrat ridge up to 45 degrees. In the reality the slope angles reach 55 degrees.

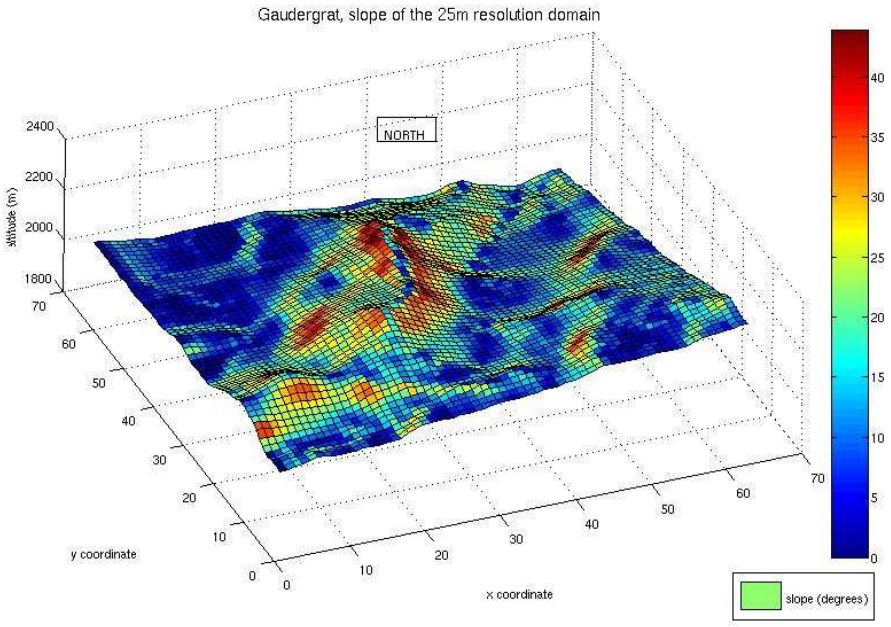

Figure B.1: Slope angle of the 25m resolution grid

Bibliography

S. Anquetin, C. Guilbaud, and J. P. Chollet. The formation and destruction of inversion layers within a deep valley. *Journal of Applied Meteorology*, 37:1547–1560, 1998.

I. Antoniou, D. N. Asimakopoulos, A. Fragoulis, A. Krotonaros, D. P. Lalas, and I. Panourgias. Turbulence measurements on top of a steep hill. *Journal of Wind Engineering and Industrial Aerodynamics*, 39:343–355, 1992.

R. A. Asselin. Frequency filter for time integration. *Monthly Weather Review*, 100: 487–492, 1972.

J. Bardina, J.H. Ferziger, and W.C. Reynolds. Improved turbulence models based on large-eddy simulations of homogeneous, incompressible, turbulent flows. Technical report tf19, Departement of Mechanical Engineering, Stanford University, Stanford, California, USA, 1983.

F. Böttcher, Ch. Renner, H. P. Waldl, and J. Peinke. On the statistics of wind gusts. *Boundary Layer Meteorology*, 108:163–173, 2003.

F. Böttcher, St. Barth, and J. Peinke. Small and large scale fluctuations in atmospheric wind speeds. *Stochastic Environmental Research and Risk Assessment*, 21:299–308(10), 2006.

E. Bou-Zeid, C. Meneveau, and M. Parlange. A scale-dependent lagrangian dynamic model for large-eddy simulation of complex turbulent flow. *Physics of Fluids*, 17, (2):025105, 2005.

E.F. Bradley. An experimental study of the profiles of wind speed, shearing stress and turbulence at the crest of a large hill. *Quarterly Journal of the Royal Meteorological Society*, 106 (447):101–123, 1980.

A. R. Brown, J. M. Hobson, and N. Wood. Large-eddy simulation of a neutral turbulent flow over rough sinusoidal ridges. *Boundary Layer Meteorology*, 98: 411–441, 2001.

J. A. Businger, J. C. Wyngaard, Y. Izumi, and E. F. Bradley. Flux-profile relationships in the atmospheric surface layer. *Journal of Atmospheric Sciences*, 28: 181–189, 1971.

D.W. Buyn. On the analytical solutions of flux-profile relationships for the atmospheric surface layer. *Journal of Applied Meteorology*, 25:1205–1212, 1990.

F. K. Chow. *Subfilter-Scale Turbulence modeling for Large-Eddy Simulation of the Atmospheric Boundary Layer over Complex Terrain.* dissertation, Stanford University, 2004.

F. K. Chow, A. P. Weigel, R. L. Street, M. W. Rotach, and M. Xue. High-resolution large eddy simulatuions of flow in a steep alpine valley. PartI: methodology, verification and sensitivity experiments. *Journal of Applied Meteorology*, 45(1):63–86, 2006.

T. L. Clark and W. D. Hall. Multi-domains simulations of the time dependend navier-stokes equations : benchmark error analysi of some nesting procedures. *Journal of Computational Physics*, 92:456–481, 1991.

A. Colette, F. K. Chow, and R. L. Street. A numerical study of inversion layer breakup and the effect of topographic shading in idealized valleys. *Journal of Applied Meteorology*, 42(9):1255–1272, 2003.

S. F. J. de Wekker, J. D. Steyn, M. W. Rotach, and S. Zhong. The performance of RAMS in representing the convective boundary layer structure in a very steep valley. *Env. Fluid. Mech.*, 5(156):1255–1272, 2005.

J. W. Deardorff. Parameterization of the Planetary Boundary layer for Use in General Circulation Models. *Monthly Weather Review*, 100(2):93–106, 1972.

J. W. Deardorff. Stratocumulus-capped mixed layers derived from a 3-dimensional model. *Boundary Layer Meteorology*, 18(4):495–527, 1980.

E.D. Eggleston and R.N. Clark. Cut-in note 1 : wind speed power spectrum analysis for bushland, texas, usa. *Wind Engineering*, 24:49–52, 2000.

D. Founda, M. Tombrou, D. P. Lalas, and D. N. Asimakopoulos. Some measurements of turbulence characteristics over complex terrain. *Boundary Layer Meteorology*, 83:221–245, 1997.

P. Gauer. Numerical modeling of blowing and drifting snow in alpine terrain. *Journal of Glaciology*, 47(156):97–101, 2001.

M. Germano, U. Piomelli, P. Moin, and W. Cabot. A dynamic subgrid-scale eddy-viscosity model. *Phys. Fluids*, 3:1760–1765, 1991.

A. Gohm, G. Zängl, and G. J. Mayr. South Foehn in the Wipp Valley on 24 October 1999 (MAP IOP 10): verifictaions of high resolution numerical simulations with observations. *Monthly Weather Review*, 132:78–102, 2004.

Ch. Hug, M. Lehning, H. Lewis, N. Raderschall, and S. D. Mobbs. Wind field modelling over steep topography - Application of two numerical models to a mountain ridge. *J. Geophys. Res.-Atmospheres*, submitted.

J. C. R. Hunt, S. Leibovich, and K. J. Richards. Turbulent shear flow over hills. *Quart. J. Roy. Meteor. Soc.*, 114:1435–1470, 1988a.

J. C. R. Hunt, K. J. Richards, and P. W. M. Brighton. Stably stratified flows over low hills. *Quart. J. Roy. Meteor. Soc.*, 114:859–886, 1988b.

C. Huntingford, E.M. Blyth, N. Wood, F.E. Huwer, and A.L.M. Grant. The effect of orography on evaporation. *Boundary Layer Meteorology*, 86:487–504, 1998.

A. Juneja and J.G. Brasseur. Characteristics of subgrid-resolved-scale dynamics in anisotropic turbulence, with application to rough-wall boundary layers. *Physics of Fluids*, 11, (10):3054–3058, 1999.

J. C. Kaimal and J. J. Finnigan. *Atmospheric boundary layer flow : their structure and measurement.* Oxford University Press, 1994.

J. C. Kaimal, J. C. Wyngaard, Y. Izumi, and O. R. Coté. Spectral characteristics of surface-layer turbulence. *Quart. J. Roy. Meteor. Soc.*, 98:563–589, 1972.

S. Khanna and J.G. Brasseur. Three-dimensional buoyancy- and shear-induced local structure of the atmospheric boundary layer. *Journal of the Atmospheric Sciences*, 55, (5):710–743, 1998.

H. G. Kim and V. C. Patel. Test of turbulence models for wind flow over terrain with separation and recirculation. *Boundary Layer Meteorology*, 94:5–21, 2000.

J. B. Klemp and R. B. Wilhelmson. The simulation of three-dimensional convective storm dynamics. *Journal of the Atmospheric Sciences*, 35:1070–1096, 1978.

M. Lehning, H. Löwe, M. Ryser, and N. Raderschall. Inhomogeneous precipitation distribution and snow transport in steep terrain. *Water Resources Research*, 2008, submitted.

H. W. Lewis. *The dynamics of the atmospheric boundary layer over steep terrain.* PhD thesis, The University of Leeds, School of Earth and Environment, 2006.

H. W. Lewis, S. D. Mobbs, and M. Lehning. Observations of cross-ridge flows across steep terrain. *Q. J. R. Meteorol. Soc.*, submitted, 2007.

D. K. Lilly. On the numerical simulation of buoyant convection. *Tellus*, 14:148–172, 1962.

D. K. Lilly. The representation of small scale turbulence in numerical simulations. *Proceedings of the IBM Scientific Computing symposium on Environmental Sciences.*, IBM Form No. 320-1951:195–210, 1967.

J.F. Louis, M. Tiedke, and J.F. Geleyn. A short history of the operational PBL parameterization of the ECWMF. In *Workshop on planetary boundary layer parameterization*, pages 59–79. ECWMF, Reading, England, November 1981.

St. Lueck, J. Peinke, and R. Friedrich. Uniform statistical despcrition of the transition between near and far field turbulence in a wake flow. *Physical Review Letters*, 83:5495–5498, 1999.

P. Mason and N. Callen. On the magnitude of the subgrid-scale eddy-coefficient in Large-eddy simulations of turbulent flow. *Journal of Fluid Mechanics*, 162: 439–462, 1986.

P. Mason and D. Thomson. Stochastic backscatter in Large-eddy simulations of boundary layers. *J. Fluid Mech.*, 78:242–251, 1992.

P. J. Mason. On the parameterization of orographic drag. In *ECWMF Seminar on Physical Parametrization for Numerical Models of the Atmosphere*, pages 139–165. ECWMF, Reading, U.K., 1985.

P. J. Mason and R. I. Sykes. Three-dimensional numerical integrations of the Navier-Stokes equations for flow over surface-mounted obstacles. *J. Fluid Mech.*, 91(3): 433–450, 1979.

P.J. Mason and D.J. Thomson. Large-eddy simulations of the neutral-static-stability planetary boundary. *Quarterly Journal of the Royal Meteorological Society*, 113: 413–443, 1987.

S.D. Mayor, P.R. Saplart, and G.J. Tripoli. Application of a perturbation recycling method in the large-eddy simulation of a mesoscale convective internal boundary layer. *Journal of the Atmospheric Sciences*, 59:2385–2395, 2002.

S. Mobbs, H. Lewis, and M. Lehning. Surface observations during Gaudex 2003. In *Proceedings of the ICAM-MAP 2005 Conference*, Zadar, Croatia, 2005.

C. H. Moeng. A large-eddy-simulation model for the study of planetary boundary layer turbulence. *Journal of the Atmospheric Sciences*, 41(13):2052–2062, 1984.

C.H. Moeng, J. Dudhia, J. Klemp, and P. Sullivan. A large-eddy-simulation model for the study of planetary boundary layer turbulence. *Journal of the Atmospheric Sciences*, 135(13):2295–2311, 2007.

J. Noihlan and S. Platon. A simple parameterization of land surface processes for meteorological models. *Monthly Weather Review*, 117:536–549, 1989.

J. M Noilhan and S. Planton. A simple parameterization of land surface processes for meteorological models. *Monthly Weather Review*, 117:536–549, 1989.

P. Nutter, M. Xue, and D. Stensrud. Application of lateral boundary conditions perturbations to help restore dispersion in limited-area ensemble forecasts. *Monthly Weather Review*, 132:2378–2390, 2004.

J. Paegle, Q. Yang, and M. Wang. Predictability in limited area and general models. *Meteorology and Atmospheric Physics*, 63:53–69, 1997.

H. A. Panofsky and J. A. Dutton. *Atmospheric turbulence; models and methods for engineering applications*. Wiley and Sons, 1984.

E.G. Patton, K.J. Davis, M.C. Barth, and P.P. Sullivan. Decaying scalars emitted by a forest canopy : a numerical study. *Boundary Layer Meteorology*, 100 (1): 91–129, 2001.

R.A. Pielke. *Mesoscale meteorological modeling.* Orlando, FL : Academic Press, 1984.

J. E. Pleim and A. Xiu. Development and testing of a surface flux and planetary boundary layer model for application in mesoscale models. *Journal of Applied Meteorology.*, 34:16–32, 1995.

S. B. Pope. *Turbulent Flows.* Cambridge University Press, 2000.

F. Porté-Agel, C. Meneveau, and M. B. Parlange. A scale-dependent dynamic model for large-eddy simulation : application to a neutral atmospheric boundary layer. *Journal of Fluid Mechanics*, 415:261–284, 2000.

N. Raderschall, M. Lehning, and C. Schär. Fine-scale modeling of the boundary layer wind field over steep topography. *Water Resources Research*, 2008, submitted.

M.R. Raupach and J.J. Finnigan. The influence of topography on meteorological variables and surface-atmosphere interactions. *Journal of Hydrology*, 190:182–213, 1997.

A.N. Ross, S.J. Arnold, S.B. Vosper, S.D. Mobbs, N. Dixon, and A.G. Robins. A comparison of wind-tunnel experiments and numerical simulations of neutral and stratified flow over a hill. *Journal of Fluid Mechanics*, 113:427–459, 2004.

M. W. Rotach, P. L. Calanca, R. Vogt, D. Steyn, G. Graziani, M. Andretta, A. Christen, S. Cieslik, R. Conolly, vand Van Gorsel E. Galmarini, S., J. Gurtz, E. Kadygrov, V. Kadygrov, E. Miller, B. Neininger, M. Rucker, H. Weber, A. Weiss, A. de Wecker, and M. Zappa. Turbulence structure and exchange processes in an Alpine Valley. The Riviera Project. *Bull. Amer. Meteor. Soc.*, 85:1367–1385, 2004.

P. Sagaut. *Large-eddy simulation for incompressible flows.* Springer Verlag, Berlin, 2002.

I. Senocak, A. S. Ackerman, M. P. Kirkpatrick, D. E. Stevens, and N. N. Mansour. Study of near-surface models for large-eddy simulations of a neutrally stratified atmospheric boundary layer. *Boundary Layer Meteorology*, 124:405–424, 2007.

R.H. Shaw and U. Schumann. Large-eddy simulation of turbulent flow above and within a forest. *Boundary Layer Meteorology*, 61 (1-2):47–64, 1992.

J. Smagorinsky. General circulation experiments with the primitive equations. *Monthly Weather Review*, 14:99–152, 1963.

P.R. Spalart. Direct Simulation of a turbulent boundary layer up to $R_\theta = 1410$. *Journal of Fluid Mechanics*, 249:337–371, 1988.

G. Spreitzhofer and N. Raderschall. Generating artificial vertical soundings over complex terrain from the almo model output to drive a high resolution snow-drift model. *Meteorol. Appl.*, 11(4):311–318, 2004.

R. B. Stull. *An introduction to boundary Layer Meteorology.* Kluwer Academic Publishers, Boston, 1988.

P. P. Sullivan, J. C. McWilliams, and C. H. Moeng. A subgrid-scale model for large-eddy simulation of the planetary boundary-layer flow. *Boundary Layer Meteorology*, 71(3):247–276, 1994.

P. P. Sullivan, J. C. McWilliams, and C. H. Moeng. A grid nesting method for large-eddy simulation of planetary boundary-layer flows. *Boundary Layer Meteorology*, 80:167–202, 1996.

W. Y. Sun and C. Z. Chang. Diffusion model for a convective boundary layer. Part I: Numerical simulation of convective boundary layer. *Journal of climate and applied meteorology*, 25:1445–1453, 1986.

R.I. Sykes. An asymptotic theory of incompressible turbulent boundray-layer flow over a small hump. *Journal of Fluid Mechanics*, 101:647–670, 1980.

P. A. Taylor and H. W. Teunissen. The Askervein project : overview and background data. *Boundary Layer Meteorology*, 39:15–39, 1987.

E. Van Gorsel, A. Christen, C. Feigenwinter, E. Parlow, and R. Vogt. Daytime turbulence statistics over a steep forested slope. *Boundary Layer Meteorology*, 109:311–329, 2003.

T. T. Warner and and Treadon R. E. Peterson, R. A. A tutorial on lateral boundary conditions as a basic and potentially seriouis limitation to regional numerical weather prediction. *Bull. Amer. Meteor. Soc.*, 78(11):2599–2617, 1997.

A. P. Weigel, F. K. Chow, M. W. Rotach, R. L. Street, and M. Xue. High-resolution large eddy simulations of flow in a steep alpine valley. PartII: flow structure and heat budgets. *Journal of Applied Meteorology*, 45(1):87–107, 2006.

A. P. Weigel, F. K. Chow, and M. W. Rotach. On the nature of turbulent kinetic energy in a steep and narrow alpine valley. *Boundary Layer Meteorology*, 123: 177–199, 2007.

C.D. Whiteman. *Moutain meteorology : foundamentals and applications*. 2000.

J.M. Wilczak, S.P. Oncley, and S.A. Stage. Sonics anemometers tilt correction algorithms. *Boundary Layer Meteorology*, 99:127–150, 2001.

N. Wood. The kettles hill project : Field observations, wind tunnel simulations and numerical model predictions for flow over a low hill. *Boundary Layer Meteorology*, 43:309–343, 1988.

N. Wood. Wind flow over complex terrain : a historical perspective and the prospect for large-eddy modelling. *Boundary Layer Meteorology*, 96:11–32, 2000.

M. Xue, K. K. Droegemeier, V. Wong, A. Shapiro, and K. Brewster. ARPS version4.0 User's guide. Technical report, University of Oklahoma, Norman, OK : Center for Analysis and Prediction of Storms, 1995.

M. Xue, K. K. Droegemeier, and V. Wong. The Advanced Regional Predidiction System (ARPS)- A multi-scale, nonhydrostatic atmospheric simulation and prediction model. PartI: Model dynamics and verification. *Meteorology and Atmospheric Physic*, 75:161–193, 2000.

M. Xue, K. K. Droegemeier, V. Wong, A. Shapiro, K. Brewster, F. Carr, D. Weber, Y. liu, and D. Wang. The Advanced Regional Predidiction System (ARPS)- A multi-scale, nonhydrostatic atmospheric simulation and prediction tool. PartII: Model physics and applications. *Meteorology and Atmospheric Physic*, 76:143–165, 2001.

T. Yamada and G. Mellor. A simulation of the wangara atmospheric boundary layer data. *Journal of the Atmospheric Sciences*, 32 (12):2309–2329, 1975.

G. Zängl, B. Chimani, and C. Häberli. Numerical simulations of the Foehn in the Rhine Valley on 24 October 1999 (MAP IOP 10). *Monthly Weather Review*, 132: 368–389, 2004.

O. Zeman and N.O. Jensen. Modification of turbulence charateristics in flow over hills. *Quarterly Journal of the Royal Meteorological Society*, 113:55–80, 1987.

J. Zhou, P.A Taylor, and Y. , Qi. Dynamic processes in stably stratified boundary layer flow over topography. In *Proceedings of the 11th symposium on boundary layers and turbulence*, Charlotte, NC, USA, 1995.

Curriculum Vitae

Education

2003–2007	Ph.D. student at the Swiss Institute for Snow and Avalanche Research, Davos, Switzerland, in the group Snow and Micrometeorology
2000–2002	Ecole Centrale Nantes (ECN), Nantes, France. *Master of Engineering in Hydrodamics and Ocean Engineering* and *Diplôme d'Etudes Approfondies (DEA) in Fluids Dynamics and Transfer.*
1996–2000	'Maîtrise' (4-years degree) in Mechanics of Fluids and Solids at the University Joseph Fourier, Grenoble. *Maîtrise in Mechanics.*
1996	*Baccalauréat Scientifique*, (High-school graduation), Annecy, France

Professional training

2002	Instituto Superior Tecnico de Lisboa (IST), Lisbon, Portugal
2001	Ifremer, Cellule Oceano-Meteo, Centre de Brest, France
2000	Southampton Oceanography Centre, Southampton, U.K
1999	Geophysics and Mechanics Laboratory, LIRIGM, University of Grenoble, France.

International Conferences

International Conference on Montain Meteorology (ICAM-MAP), Chambéry, France, 4-8 June 2007.